

Discotic liquid crystals:
from dynamics to conductivity

The research described in this thesis was performed in Fundamental Aspects of Material and Energy of the Department of Radiation, Radionuclides and Reactors, Faculty of Applied Science, Delft University of Technology, Mekelweg 15, 2629 JB Delft, The Netherlands

Discotic liquid crystals: from dynamics to conductivity

PROEFSCHRIFT

ter verkrijging van de graad van doctor

aan de Technische Universiteit Delft,

op gezag van de Rector Magnificus prof. dr. ir. J.T. Fokkema,

voorzitter van het College voor Promoties,

in het openbaar te verdedigen

op maandag 23 april 2007 om 10.00 uur

door

Olga Viktorovna KRUGLOVA

Magister van de Natuurkunde,

Staatsuniversiteit van Sint-Petersburg (Rusland)

geboren te Nizhnij Tagil (Rusland)

Dit proefschrift is goedgekeurd door de promotor:
Prof.dr. G. J. Kearley

Toegevoegd promotor:
Dr. F.M. Mulder

Samenstelling promotiecommissie:

Rector Magnificus	voorzitter
Prof.dr. G.J. Kearley	Technische Universiteit Delft, promotor
Dr. F.M. Mulder	Technische Universiteit Delft, toegevoegd promotor
Prof. dr. S.J. Picken	Technische Universiteit Delft
Prof. dr.G. Kneller	Centre de Biophysique Moléculaire, France
Prof. dr. L.D.A. Siebbeles	Technische Universiteit Delft
Prof. dr. M.R. Johnson	Institute of Laue-Langevin, France
Dr. hab. E. Mendes	Technische Universiteit Delft

© 2007 O. Kruglova and IOS Press

All rights reserved. No part of this book may be reproduced, stored in a retrieval system, or transmitted, in any form or by any means, without prior permission from the publisher.

ISBN

Keywords: Discotic liquid crystals, neutron scattering, dynamics, conductivity.

Published and distributed by IOS Press under the imprint of Delft University Press

Publisher
IOS Press
Nieuwe Hemweg 6b
1013 BG Amsterdam
The Netherlands
tel: +31-20-688 3355
fax: +31-20-687 0019
email: info@iospress.nl
www.iospress.nl
www.dupress.nl

LEGAL NOTICE

The publisher is not responsible for the use which might be made of the following information.

PRINTED IN THE NETHERLANDS

Contents

1	Introduction	1
1.1	Discotic liquid crystals	2
1.2	Neutron scattering	4
1.2.1	Coherent and incoherent cross-sections	5
1.2.2	Scattering function	7
1.3	The continuous time random walk model	8
1.4	Model for relaxation kinetics in correlating environment	11
1.5	Conductivity	13
1.6	Scope of this thesis	15
2	Experimental techniques and calculation methods	19
2.1	Structure	19
2.1.1	X-ray diffraction	19
2.1.2	Neutron diffraction	20
2.1.3	Density functional theory (DFT)	20
2.2	Dynamics	21
2.2.1	Quasielastic neutron scattering (QENS)	21
2.2.2	Molecular dynamics simulation	23
2.2.3	Dielectric relaxation spectroscopy (DRS)	24
2.2.4	Calculation of molecular vibrations	24
2.2.5	TOSCA	24
2.2.6	Conductivity	25
3	Dispersive kinetics in discotic liquid crystals	29
3.1	Introduction	29
3.2	Experimental techniques	30
3.3	Results and discussion	30
3.3.1	Dynamics	30
3.3.2	Influence of alignment on relaxation in HAT6	37
3.4	Conclusion	39

4	A Compact Model For Electron-Phonon Calculations	45
4.1	Introduction	45
4.2	Experimental techniques	46
4.2.1	Preparation	46
4.2.2	INS spectra	46
4.2.3	Computational methods	47
4.3	Results and Discussion	48
4.3.1	Observed INS spectra, sensitivity of core-modes to tail-length	48
4.3.2	Calculated Spectra	50
4.3.3	HAT1 core vibrations	51
4.3.4	Conformation of the methoxy tail	52
4.3.5	Other models and electronic effects	53
4.4	Conclusions	53
5	Coupling Between Local Vibrations and Charge Transport	57
5.1	Introduction	57
5.2	Method and Theory	58
5.3	Results and Discussion	60
5.4	Conclusions	63
6	Structure of charge transfer complex	69
6.1	Introduction	69
6.2	Experimental	70
6.2.1	Preparation	70
6.2.2	Alignment	70
6.2.3	Neutron scattering	71
6.2.4	X-ray diffraction	71
6.2.5	Optical polarization microscope (OPM)	71
6.2.6	Dielectric relaxation spectroscopy (DRS)	71
6.2.7	DFT calculation	72
6.3	Results and discussion	72
6.4	Conclusions	82
7	Conductivity of discotic liquid crystals	89
7.1	Introduction	89
7.2	Experimental techniques	90
7.2.1	Quasielastic neutron scattering	90
7.2.2	Pulse-Radiolysis Time-Resolved Conductivity	90
7.3	Results and discussion	90
7.3.1	Dynamics	90
7.3.2	Effect of TNF on the molecular relaxation processes	91
7.3.3	Fluctuations	92
7.3.4	Conductivity	94
7.3.5	Conductivity and dynamics of HAT6 and complex HAT6-TNF	95

<i>CONTENTS</i>	vii
7.3.6 Charge-molecule coupling strength	99
7.3.7 Determination of conductivity using relaxation time	99
7.4 Conclusion	100
8 General conclusions	105
Summary	107
Samenvatting	109
Acknowledgements	111
Curriculum Vitae	113
List of Publications	115
Acronyms	117

List of Figures

1.1	Discotic liquid crystalline phases	2
1.2	Hexakis(n-hexyloxy)triphenylene	3
1.3	Schematic representation of neutron scattering geometry	4
1.4	Illustration of the neutron scattering types.	6
1.5	Schematic representation of the continuous time random walk.	9
1.6	Schematic representation of relaxation process with fluctuating potential barrier.	14
2.1	Illustration of the Bragg law.	20
2.2	IN6 time of flight spectrometer	22
2.3	Schematic representation of Pulse Radiolysis Time Resolved Microwave Conductivity.	26
3.1	Fitting with two Lorentzians.	31
3.2	Fitting with Mittag-Leffler function.	32
3.3	$\tau(Q)$ for HAT6 with deuterated tails and protonated HAT6.	33
3.4	$\tau(Q)$ for protonated HAT6 at different temperatures.	34
3.5	$\beta(Q)$ and $\eta(Q)$ for HAT6 with deuterated tails and protonated HAT6.	35
3.6	$\beta(Q)$ and $\eta(Q)$ for protonated HAT6 at different temperatures.	36
3.7	Levy distribution for the jump length.	37
3.8	Temperature dependence of Levy index, α	38
3.9	Orientations of columns in HAT6 in NSE experiment.	39
3.10	Neutron-Spin Echo data and their fitting with Mittag-Leffler function	40
3.11	$\tau(T)$ and $\beta(T)$ for NSE data.	41
4.1	Structures of investigated triphenylene derivatives.	47
4.2	Observed INS spectra of HAT6D, HAT3D and HAT1D.	48
4.3	Examples of in-plane and out-of-plane vibrational displacements of the triphenylene core.	49
4.4	Observed and calculated INS spectra of HAT1D.	50
4.5	Observed INS spectrum of HAT3D compared with the calculated spectrum of HAT1D.	51
4.6	Observed INS spectrum of HAT6D compared with calculated spectra of various simplified models.	52
5.1	Variation of the interaction energy of the HOMOs, β	58
5.2	Variation of the interaction energy of the total energy, α	59
5.3	Correlation between HOMO interaction and total intermolecular interaction.	60

5.4	Frequency spectra for HOMO and total interaction.	61
5.5	Fitting of the intermolecular interaction frequency spectra, α , and HOMO interaction frequency spectra, β , with Lévy distribution.	63
5.6	Frequency spectra of the HOMOs of the dimer and the monomer.	64
5.7	Correlation of the HOMO and HOMO-1 energies of the distorted dimers with the total interaction energy of dimer formation from the distorted monomers.	65
6.1	2,4,7trinitro-9-fluorenone (TNF).	70
6.2	Alignment of HAT6-TNF on different substrates.	72
6.3	Elastic neutron scattering, diffraction pattern.	73
6.4	Geometry of experiment and possible arrangement of HAT6 and TNF.	74
6.5	Calculated neutron diffraction pattern for pure HAT6 and sandwich arrangements for HAT6-TNF.	75
6.6	Models for DFT calculations.	77
6.7	Integrated intensities for different position of sample with respect to X-ray beam.	78
6.8	Comparison of XRD for HAT6 and HAT6-TNF.	79
6.9	Azimuthal scan, χ , of HAT6-TNF at room temperature, $2\theta=5.84^\circ$	80
6.10	Azimuthal scan, χ , of HAT6-TNF at room temperature, $2\theta=108.21^\circ$	81
6.11	Schematic representation of possible HAT6-TNF arrangement.	82
6.12	Relaxation time τ versus Q for HAT6 with deuterated tails, without and with TNF.	83
6.13	3D representation of the dielectric loss $\epsilon''(f, T)$ measured during cooling of a HAT6-TNF complex.	84
6.14	Arrhenius diagram of the four relaxation processes of HAT6-TNF.	85
7.1	Orientation of HAT6 and HAT6-TNF after shear alignment.	91
7.2	Intermediate scattering function $F(Q,t)$ for HAT6 and HAT6-TNF.	92
7.3	Dependence of relaxation time τ via momentum transfer Q for HAT6D and HAT6D-TNF in two orientations, T=370K.	93
7.4	Comparison of $\tau(Q)$ between HAT6D-TNF and HAT6-TNF in two orientations, T=370K.	94
7.5	Dispersion for HAT6 and HAT6-TNF in two orientations.	95
7.6	Conductivity transients for HAT6.	96
7.7	Fits of HAT6 normalized transients using the Mittag-Leffler function.	97
7.8	A comparison of normalized transients for HAT6 and HAT6-TNF.	98
7.9	Conductivity transients for HAT6-TNF at different temperatures including fits with Mittag-Leffler function.	100
7.10	Temperature dependence of dispersion parameter β for HAT6-TNF at $Q=1.12 \text{ \AA}^{-1}$ from PR TRMC and neutron scattering in two orientations.	101

Chapter 1

Introduction

The growing world population and increased demand for energy challenge science in developing new ways of energy production: more efficient and less polluting. Nowadays oil is the most consumed natural energy resource, although its share in the world energy consumption will decrease with time. The percentage of so called alternative and renewable energy sources increases each year, which includes wind power, solar power, hydroelectricity, geothermal power, wave power and bioenergetics [1]. Currently, hydroelectricity makes the greatest contribution to total world energy-production. Although its long-term potential could be quite high, it has a major downside, which is a strong impact on environment. Another example of such sources is wind power which also has great potential, but usage on large scale can impact the global climate. Bioenergetics attract a lot of attention as well, but unfortunately it can also contribute to global warming disturbing natural carbon balance.

Geothermal power has very large potential taking into account all heat that is inside the Earth, but today it is rather limited to special locations, and only two countries, New Zealand and Iceland, use it extensively. Ocean thermal energy and tidal energy that represent wave power sources have great potential when they are properly developed. Clearly, there is considerable scope for solar power usage. At the moment solar cells, which convert solar energy into electricity, are made mostly from highly purified silicon, which is expensive and energy intensive material.

In 2000 Alan Heeger, Alan G. MacDiarmid and Hideki Shirakawa were awarded the Nobel Prize in Chemistry for the discovery and development of conductive polymers in 1977. This discovery has opened the possibility of using organic materials instead of silicon. However, the conjugated double-bond of these materials is sensitive to light and can be broken by shorter wavelengths due to the highly polar nature of the polymers. For this, and other reasons discotic liquid crystals may be a good alternative to conductive polymers. Discotic systems are stable compounds that form columns due to π orbitals overlap, which can be used as 1D path for charge carriers. Due to their liquid crystalline nature the materials have a self annealing mechanism for structural damage. Unfortunately, charge carriers in discotic materials have low mobility. Consequently, the main challenge is to understand how structure and dynamics on different timescales will influence the conductive properties in general and mobility in particular and, therefore, the possible ways to improve it.

⁰Cover design by Svetlana Divina, picture by Andrey Divin taken in Larrabee State Park, WA, USA

1.1 Discotic liquid crystals

Liquid crystals represent the state of the matter which exhibits properties of both liquid and solid states with crystalline long range order. There are many types of liquid-crystal phases depending on their optoelectronic properties such as nematics, smectics, cholesterics and discotics. Molecules that display liquid-crystalline phases are called mesogens. Typically they are rod-shaped organic compounds, which are called calamitic, but also they can have the shape of a disc and are then called discotic mesogens. In most cases any mesogens have the tendency to orient themselves along their long axis. Since molecules having disc-like core are of particular interest we will focus on consideration this type of mesogen. The first discotic liquid-crystal molecule with a benzene ring as

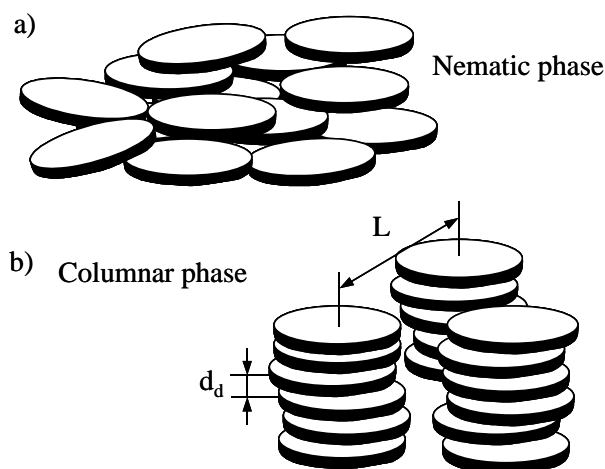


Figure 1.1: a) Nematic discotic phase. Molecules are oriented in the same direction but positional order is absent; b) Columnar discotic phase. Molecules have orientational and positional order.

the core surrounded by six alkyl chains, was found in 1977 by S. Chandrasekhar [2]. Since then a large number of discotic molecules has been found. Triphenylene, coronene, phthalocyanine represent the cores of discotic liquid crystals. Disc-shaped molecules orient along their short axis and have tendency to lie on top of each other forming either discotic nematic phase, which represents only orientational ordering, or discotic columnar phase, which represents orientational and positional ordering, fig. 1.1. Such a tendency occurs due to the presence of delocalized π electrons on the both sides of the molecular core that minimize their energy by $\pi - \pi$ overlapping. This $\pi - \pi$ overlapping defines distance between two discs in a stack which lies within range 3.3-3.6Å for many

aromatic molecules [3]. In this way they form so called "molecular wires" that can be used by electrons or holes as a pathway. This property has attracted a lot of attention as a potential charge transfer system in molecular electronics [4]. The distance between columns will be determined by the length of the molecular "tails" which are attached to disc-like core and which can vary over a wide range.

In this thesis the compound hexakis(n-hexyloxy)triphenylene (HAT6), fig.1.2, is studied. It has molecular structure (core with tails) that is sufficiently large to have an extended π electron system while it is still small enough to allow detailed experiment analysis and modelling. The HAT6 molecule possesses D_{3h} symmetry. The liquid crystalline (LC) phase of HAT6 is within $67^\circ\text{C} < T < 97^\circ\text{C}$ temperature range. In the LC phase HAT6 forms columns in a two dimensional hexagonal crystal structure with distance between discs of $d_d = 3.41 \text{ \AA}$, and distance between the columns of, $L = 18.3 \text{ \AA}$ with density $\rho = 1.04 \frac{\text{g}}{\text{cm}^3}$.

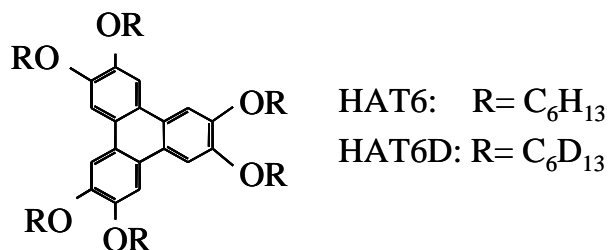


Figure 1.2: Hexakis(n-hexyloxy)triphenylene

1.2 Neutron scattering

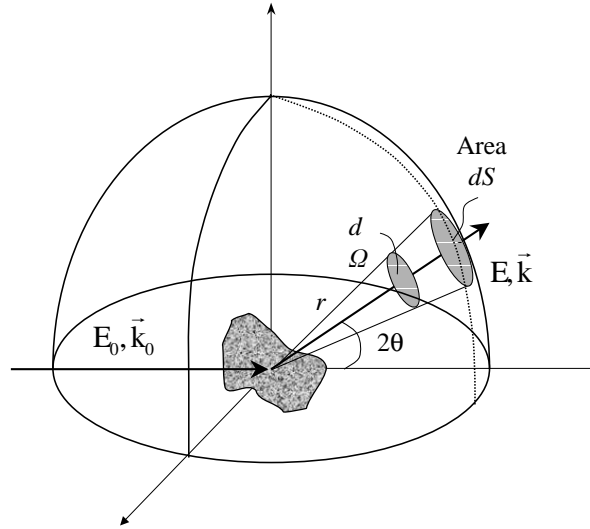


Figure 1.3: Schematic representation of neutron scattering geometry

In the liquid crystalline state the discotic molecules show mobility on timescales that can be probed directly by neutron scattering. Neutrons provide a particularly convenient tool to study dynamics of molecular complexes since their wavelength is comparable with the distance between molecules in solids and liquids and the kinetic energies are comparable with those transferred during dynamical processes. Neutrons interact directly with nuclei allowing certain parts of molecular systems to be highlighted by isotopic substitution since the neutron scattering cross-section varies from isotope to isotope. This is especially important for systems containing hydrogen because although hydrogen has the largest total scattering cross section, 82.02 barns, the total cross section of deuterium is only 7.64 barns. For comparison, carbon neutron cross section is 5.58 barns, aluminum-1.5 barns and oxygen-4.232 barns. Hydrogen nuclei are also good probes for the overall dynamics in a system due to its light mass, which allows it to follow even smallest changes in motion.

Scattering is non-destructive physical process in which some form of radiation, for example, neutrons or X-ray, is made to deviate from its initial direction of propagation due to non-uniformity of the matter through which it passes. The scattering process can change the momentum and the

energy of neutron. The energy transfer can be expressed as

$$\hbar\omega = E - E_0 = \frac{\hbar^2}{2m} (k^2 - k_0^2) \quad (1.1)$$

and its momentum transfer as

$$\hbar\vec{Q} = \hbar (\vec{k} - \vec{k}_0). \quad (1.2)$$

\vec{Q} is called scattering vector and can be calculated from experiment geometry using cosine rule

$$Q = (k^2 + k_0^2 - 2kk_0 \cos 2\theta)^{\frac{1}{2}}, \quad (1.3)$$

fig.1.3.1 . Depending on amount of change in the energy one distinguishes several types of scattering: elastic scattering where energy does not change, $\hbar\omega = 0$, but direction of flight does; inelastic where changes in energy occurs, $\hbar\omega \neq 0$, and quasielastic where energy transfer is infinitely small, $\hbar\omega \ll E_0$, fig. 1.4.2.

The quantity measured in scattering experiment is differential cross-section (fig.1.3.1). It is proportional to the number of scattered particles within energy range ΔE and variation of momentum into solid angle $d\Omega$,

$$\frac{d\sigma}{d\Omega} = \frac{\text{Scattered flux/ Unit of solid angle}}{\text{Incident flux/ Unit of surface}} \quad (1.4)$$

. The scattering cross-section characterizes the ability of an atom to deviate the incident flux from initial path. Let us see what defines scattering the cross-section for one nucleus. The incident neutron beam can be represented as a plane wave with the wavefunction $\Psi_{inc} = e^{-\vec{k} \cdot \vec{r}}$. After scattering on a nucleus the neutron wavefunction transforms into $\Psi_{sc} = \frac{b}{r} e^{-\vec{k} \cdot \vec{r}}$, where b is scattering length (or amplitude). If incident flux is defined as $\Phi_{inc} = |\Psi_{inc}|^2 v$ and scattered one as $\Phi_{sc} = |\Psi_{sc}|^2 v$ then

$$\frac{\partial\sigma}{\partial\Omega} = \frac{\Phi_{sc}/d\Omega}{\Phi_{inc}/dS}. \quad (1.5)$$

Integrating these we obtain an expression for the full cross section, $\sigma = 4\pi b^2$. The scattering length that characterizes the cross section is unique for every element and as mentioned above, it varies from isotope to isotope. Contributions from all types of atoms are obtained by adding amplitudes of scattered waves from all nuclei [5].

1.2.1 Coherent and incoherent cross-sections

The differential cross section for the same atom can be of two types: coherent and incoherent. The average $\langle b_i \rangle$ scattering length over all isotopes is called the coherent scattering length. Therefore, the coherent cross-section will be defined as

$$\sigma_{coh} = 4\pi \langle b \rangle^2. \quad (1.6)$$

The square root of mean square deviation from $\langle b_i \rangle$ determines the incoherent scattering length and will be defined as

$$b_i^{inc} = (\langle b_i^2 \rangle - \langle b_i \rangle^2)^{\frac{1}{2}}. \quad (1.7)$$

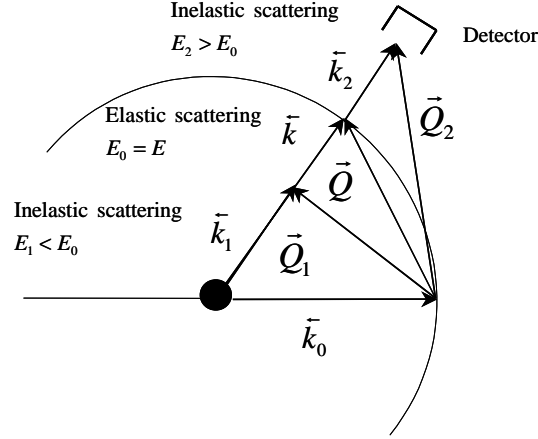


Figure 1.4: Illustration of the neutron scattering types.

That leads to following expression for incoherent cross-section

$$\sigma_{inc} = 4\pi \left(\langle b^2 \rangle - \langle b \rangle^2 \right). \quad (1.8)$$

Then the total scattering cross section is

$$\sigma_{tot} = \sigma_{coh} + \sigma_{inc}. \quad (1.9)$$

In a neutron scattering experiment the intensity is dependent on the energy and the solid angle and is usually expressed as double differential cross section

$$\frac{\partial^2 \sigma}{\partial \Omega \partial \omega} = \frac{k_{sc}}{k_{inc}} \left(\frac{\sigma_{coh}}{4\pi} S_{coh}(Q, \omega) + \frac{\sigma_{inc}}{4\pi} S_{inc}(Q, \omega) \right), \quad (1.10)$$

where k_{sc} , k_{inc} - scattered and incident wavevectors of particles; σ_{coh} , σ_{inc} -coherent and incoherent cross-section; $S_{coh}(Q, \omega)$, $S_{inc}(Q, \omega)$ -coherent and incoherent scattering functions. The coherent

scattering function contains information about particle motion in the same phase (coherent neutron scattering) and about relative positions of atoms (X-ray diffraction or neutron diffraction). The incoherent term provides information about the interference of the nucleus at $t=0$ time and the same nucleus after time t , and gives insight into the local dynamical processes occurring in system.

1.2.2 Scattering function

The neutron scattering function, $S(Q, \omega)$, relates to the pair correlation function in space and in time, $G(\mathbf{r}, t)$, through a Fourier transform [6]. $G(\mathbf{r}, t)$ describes the correlation between the presence of the particle in the position $\mathbf{r}' + \mathbf{r}$ at the time $t' + t$ and the presence of the particle in the position \mathbf{r}' at the time t' .

$$G(\mathbf{r}, t) = N^{-1} \left\langle \int d\mathbf{r}' \sum_{l,j=1}^N \delta(\mathbf{r} + \mathbf{r}_l(0) - \mathbf{r}') \cdot \delta(\mathbf{r}' - \mathbf{r}_j(t)) \right\rangle \quad (1.11)$$

For simple systems the pair correlation function under classical conditions reduces to the average density distribution at time $t' + t$ for "the observer" at time t' . It will be independent from t' , which means that the system described by that function will not have any memory about its previous state and, therefore, correlations.

$$G(\mathbf{r}, t) = N^{-1} \left\langle \sum_{l,j} \delta(\mathbf{r} + \mathbf{r}_l(0) - \mathbf{r}_j(t)) \right\rangle \quad (1.12)$$

However, such an approximation will be no longer valid for complex system, in which correlations have to be taken into account. If we consider a volume element ΔV centered at point \mathbf{r} and define an operator $\Delta P(\mathbf{r}, t)$ then $\Delta P(\mathbf{r}, t) \psi = \psi$ for all states of the system for which at least one particle is in that volume element at time t and $\Delta P(\mathbf{r}, t) \psi = 0$ for all states of the system for which no particle is in ΔV at time t . For a infinitesimal volume one can write

$$\frac{\Delta P(\mathbf{r}, t)}{\Delta V} = \sum_j \delta(\mathbf{r} - \mathbf{r}_j(t)), \quad (1.13)$$

and summing over all identical volume elements around each point one gets

$$G(\mathbf{r}, t) = N^{-1} \Delta V^{-2} \int d\mathbf{r}' \langle \Delta P(\mathbf{r}', 0) \cdot \Delta P(\mathbf{r}' + \mathbf{r}, t) \rangle. \quad (1.14)$$

This expression for the space time correlation function will represent the probability to find a particle, which was in point \mathbf{r}' at time $t' = 0$, in position $\mathbf{r}' + \mathbf{r}$ at time t . The pair distribution $G(\mathbf{r}, t)$ can be represented as

$$G(\mathbf{r}, t) = G(\mathbf{r}) + G'(\mathbf{r}, t). \quad (1.15)$$

$G(\mathbf{r})$ stands for the static pair distribution function and is used in X-ray and neutron diffraction. It represents the probability of finding the particle in the volume element around position \mathbf{r} . This part of the van Hove correlation function gives a set of peaks which correspond to Bragg

reflections. Second term, $G(\mathbf{r}, t)$, gives an information about the dynamics occurring in the system. Conventionally, $G(\mathbf{r}, t)$ can be obtained using Fick's second law

$$\frac{\partial G(\mathbf{r}, t)}{\partial t} = D \nabla^2 G(\mathbf{r}, t), \quad (1.16)$$

which describes a normal diffusion process in the system with the solution $G(\mathbf{r}, t) = \frac{1}{\sqrt{4\pi Dt}} \exp(-\frac{\mathbf{r}^2}{4Dt})$ (details see [5]). But the temporal evolution in complex systems such as glasses, polymers, liquid crystals, proteins etc. [7], deviates from Gaussian behaviour and, therefore, Fick's second law fails to characterize such diffusion kinetics. The continuous time random walk model was used to generalize Fick's second law for anomalous diffusion application.

1.3 The continuous time random walk model

The concept of a continuous time random walk is based on the idea that the length of the jump and the waiting time between two successive jumps can be obtained from the probability distribution function $\psi(\mathbf{r}, t)$ [8]. The distribution of jump lengths

$$\lambda(\mathbf{r}) = \int_0^\infty dt \psi(\mathbf{r}, t). \quad (1.17)$$

and waiting time

$$w(t) = \int_{-\infty}^\infty d\mathbf{r} \psi(\mathbf{r}, t) \quad (1.18)$$

can be obtained from $\psi(\mathbf{r}, t)$ by integration over time t . Therefore, $\lambda(\mathbf{r}) d\mathbf{r}$ specifies the probability for the jump length in the interval $(\mathbf{r}, \mathbf{r} + d\mathbf{r})$ and $w(t) dt$ - the probability for the waiting time in the interval $(t, t + dt)$. Assuming that the jump length and the waiting time are independent, the probability distribution function can be represented as

$$\psi(\mathbf{r}, t) = \lambda(\mathbf{r}) w(t). \quad (1.19)$$

In the case where they are coupled one has an expression for distribution function $\psi(\mathbf{r}, t) = p(\mathbf{r} | t) w(t)$ or $\psi(\mathbf{r}, t) = p(t | \mathbf{r}) \lambda(\mathbf{r})$ meaning that a jump of a certain length will take the relevant amount of time or in that particular time interval only a jump of certain length can be completed.

Several continuous time random walk processes can be distinguished by a characteristic waiting time

$$\tau = \int_0^\infty dt w(t) t \quad (1.20)$$

and by the jump length variance

$$\sigma^2 = \int_{-\infty}^\infty dr \lambda(\mathbf{r}) \mathbf{r}^2 \quad (1.21)$$

being finite or divergent. Using these definitions continuous time random walk can be described through an appropriate master equation [8]

$$\eta(\mathbf{r}, t) = \int_{-\infty}^\infty d\mathbf{r}' \int_0^\infty dt' \eta'(\mathbf{r}', t') \psi(\mathbf{r} - \mathbf{r}', t - t') + \delta(\mathbf{r}) \delta(t), \quad (1.22)$$

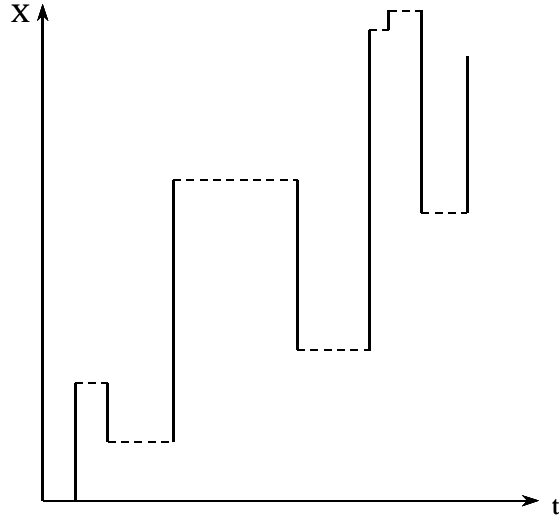


Figure 1.5: Schematic representation of the continuous time random walk.

which relates the probability distribution function $\eta(\mathbf{r}, t)$ of "walker" which just has arrived to a position \mathbf{r} at time t with "walker" which just has arrived to a position \mathbf{r} at the time t' , $\eta(\mathbf{r}, t')$. The second term denotes the initial conditions of the random walk. The probability distribution function $W(\mathbf{r}, t)$ of being in position \mathbf{r} at time t will be expressed as

$$W(\mathbf{r}, t) = \int_0^t dt' \eta(\mathbf{r}, t') \Psi(t - t') \quad (1.23)$$

meaning the arrival on that site at time t' and not moving since. The latter is defined by a cumulative probability

$$\Psi(t) = 1 - \int_0^t dt' w(t') \quad (1.24)$$

where $w(t)$ is assigned to the probability of "no jump" event during time interval $(0, t)$. In the

Fourier-Laplace domain the probability distribution function $W(\mathbf{r}, t)$ will be represented by

$$W(Q, s) = \frac{1 - w(s)}{s} \frac{W_0(Q)}{1 - \psi(Q, s)} \quad (1.25)$$

where $W_0(Q)$ is the Fourier transform of the initial condition. Let us consider the known Brownian motion with the decoupled probability distribution function $\psi(\mathbf{r}, t)$. If the waiting time distribution will be exponential, $w(t) = \tau^{-1} \exp(-\frac{t}{\tau})$, and the jump-length distribution will be Gaussian,

$$\lambda(\mathbf{r}) = (4\pi\sigma^2)^{-1} \exp\left(-\frac{\mathbf{r}^2}{4\sigma^2}\right) \quad (1.26)$$

, then corresponding Fourier-Laplace transform are

$$\begin{aligned} w(s) &\sim 1 - s\tau + O(\tau^2) \\ \lambda(Q) &\sim 1 - Q^2\sigma^2 + O(Q^4) \end{aligned} \quad (1.27)$$

Inserting this into $W(Q, s)$ with the initial condition $W_0(\mathbf{r}) = \delta(\mathbf{r})$ one obtains

$$W(Q, s) = \frac{1}{Q + D_1 s^2}, \quad (1.28)$$

with $D_1 \equiv \frac{\sigma^2}{\tau}$. Transforming this into (\mathbf{r}, t) domain one obtains the known expression for Brownian motion. Fick's second law can be restored by using differentiation theorem for the Fourier and Laplace transform

$$\begin{aligned} F \left\{ \frac{\partial^2 W(\mathbf{r}, t)}{\partial \mathbf{r}^2} \right\} &= -Q^2 W(Q, t) \\ L \left\{ \frac{\partial W(\mathbf{r}, t)}{\partial t} \right\} &= sW(\mathbf{r}, s) - W_0(\mathbf{r}) \end{aligned} \quad (1.29)$$

This expression defines a general formula for the space-time correlation function.

In this way it is possible to construct a generalized equation which will describe anomalous diffusion. The long-tailed waiting time distribution will have asymptotics

$$w(t) \sim A_\beta \left(\frac{\tau}{t}\right)^{1+\beta}, \quad (1.30)$$

which transforms into

$$w(s) \sim 1 - (s\tau)^\beta \quad (1.31)$$

and the jump-length distribution will be expressed in terms of a Levý distribution

$$\lambda(Q) = \exp(-\sigma^\alpha |Q|^\alpha) \sim 1 - (\sigma Q)^\alpha. \quad (1.32)$$

Employing the integration rule for fractional integrals

$$\begin{aligned} L \left\{ {}_0 D_t^{1-\beta} W(\mathbf{r}, t) \right\} &= s^{1-\beta} W(\mathbf{r}, s) \\ F \left\{ {}_\infty D_r^\alpha W(\mathbf{r}, t) \right\} &\equiv F \left\{ \nabla^\alpha W(\mathbf{r}, t) \right\} \equiv -Q^\alpha W(Q, t) \end{aligned} \quad (1.33)$$

one obtains an expression for the fractional diffusion equation which is a generalisation of Fick's second law

$$\frac{\partial W(\mathbf{r}, t)}{\partial t} = {}_0 D_t^{1-\beta} K_\beta^\alpha \nabla^\alpha W(\mathbf{r}, t), \quad (1.34)$$

where K_β^α represents the generalised diffusion constant, $K_\beta^\alpha \equiv \frac{\sigma^\alpha}{\tau^\beta}$. The Riemann-Liouville operator, ${}_0 D_t^{1-\beta} = \frac{\partial}{\partial t} {}_0 D_t^\beta$, is defined through

$${}_0 D_t^{1-\beta} W(\mathbf{r}, t) = \frac{1}{\Gamma(\beta)} \frac{\partial}{\partial t} \int_0^\infty dt \frac{W(\mathbf{r}, t)}{(t-t)^{1-\beta}} \quad (1.35)$$

and the Weyl fractional operator, ${}_\infty D_r^\alpha$, is defined through

$${}_\infty D_r^\alpha W(\mathbf{r}, t) = \frac{\partial^\alpha}{\partial \mathbf{r}^\alpha} \int_r^\infty dQ \frac{W(Q, t)}{(\mathbf{r}-Q)}. \quad (1.36)$$

Although the fractional diffusion equation gives a solution in terms of the van Hove correlation function, $G(\mathbf{r}, t) = W(\mathbf{r}, t)$, it does not provide a definition for relaxation time, τ , and fractional exponents, α and β , which makes it difficult to understand the physical nature of such a process. A suitable model that provides definitions in terms of fundamental physical quantities would be quite desirable. We have adapted a model suggested by Y. Berlin [9].

1.4 Model for relaxation kinetics in correlating environment

Initially, the system under consideration has a static disorder which suggests the presence of a configurational energy distribution acting as traps with depth E_i using notations as given in [9]. The characteristic time of staying in that trap, τ_i , will be determined by

$$\tau_i = \frac{1}{Z w_0} \exp\left(\frac{E_i}{k_B T}\right), \quad (1.37)$$

where Z is the number of states different from the i th state, w_0 is the jump frequency of normal diffusion, k_B is Boltzmann constant, and T is the temperature. Excitation of such media causes a rearrangement of configurational states leading to energy minimization. In complex systems such as polymers, liquid crystals etc., the relaxation rates towards lower energy for different pairs of trapping sites will vary over a very wide range,

$$k_i = k_0 \exp\left(-\frac{\eta E_i}{k_B T}\right), \quad (1.38)$$

where k_0 is pre-exponential parameter, E_i is the depth of the potential well, η is the parameter, whose physical meaning will be discussed further. As mentioned above, the continuous time random walk model defines a waiting time distribution in terms of probability of "no jump". It will be convenient then to describe the evolution of the system by means of a survival probability at initial state, $P(t) = \sum_i p_i(t)$, where the contribution from every relaxation process is taken into account, and is represented by a Kolmogorov-Feller integral equation, which is suitable for solving the kinetic problems,

$$\frac{dp_i(t)}{dt} = -k_i p_i(t) + \sum_{i,j} (w_{ji} p_j(t) - w_{ij} p_i(t)) \quad (1.39)$$

where $w_{ji}(w_{ij})$ represents the conditional probability of the transition from state j to state i (and vice versa) and with the initial condition $p_i(t=0) = p_i^0$.

By assuming uncorrelated transitions

$$w_{ji} = w_j = \frac{1}{Z\tau_j}, \quad w_{ij} = w_i = \frac{1}{Z\tau_i}$$

and introducing a Laplace transform, a general solution is found in terms of the initial population distribution, $G(E)$, and the density of substates, $g(E)$. Solution of kinetic equation with the condition,

$$G(E) = \frac{1}{E_0} \exp\left(-\frac{E}{E_0}\right), \quad E \geq 0, \quad (1.40)$$

will be expressed in the following way in the Laplace space,

$$\tilde{P} = \frac{s^{-1}(\tau s)^\beta}{1 + (\tau s)^\beta}. \quad (1.41)$$

The inverse Laplace transform of this expression will be represented in terms of the Mittag-Leffler function [9],

$$P(t) = E_\beta \left(-\left(\frac{t}{\tau}\right)^\beta \right) = \sum_{k=0}^{\infty} \frac{(-1)^k \left(\frac{t}{\tau}\right)^{\beta k}}{\Gamma(1 + \beta k)}, \quad (1.42)$$

where $\beta = \frac{T}{T_0} < 1$ is a dispersion parameter, T is temperature and T_0 is the the temperature at which the system has Gaussian behavior (where T_0 is related to the parameter E_0 of the exponential distribution of substates). The relaxation time of the system is defined from solution as

$$\tau = \frac{1}{Zw_0} \left[\frac{Zw_0\pi\beta}{k_0 \sin(\pi\beta)} \left(1 + (\eta - 1) \frac{1}{\beta} \right) \right]^{\frac{1}{\beta}} \quad (1.43)$$

Let us analyze the expression for relaxation time. Transforming it with respect to Z we obtain the following representation

$$Zw_0 = \left[\frac{\tau^\beta k_0 \sin(\pi\beta)}{\pi\beta} \right]^{\frac{1}{1-\beta}} \frac{1}{\left(1 + (\eta - 1) \frac{1}{\beta} \right)^{\frac{1}{1-\beta}}}. \quad (1.44)$$

Assuming

$$Z = \left[\frac{w_0^{1-\beta} \pi\beta}{\tau^\beta k_0 \sin(\pi\beta)} \right]^{\frac{1}{1-\beta}} \quad (1.45)$$

we obtain a formula for the distribution of states

$$\frac{Z_i}{Z} = \left(1 + (\eta - 1) \frac{1}{\beta} \right)^{\frac{1}{1-\beta}}. \quad (1.46)$$

In classical thermodynamics the number of states with a certain energy is represented by the Boltzmann distribution, $\frac{N_i}{N} = \exp\left(-\frac{E_i}{k_B T}\right)$, but in the present case the relation gives a different distribution. Comparing it with a Boltzmann distribution generalization, Tsallis distribution,

$$\frac{N_i}{N} = (1 + (q - 1)x)^{\frac{q}{q-1}} \quad (1.47)$$

we see close similarities. The important quantity here is the entropic index, q . The entropic index defines the degree of nonextensivity or, another words, the degree of interaction among parts of the system. If A and B are parts of the system ($p_{ij}^{A+B} = p_i^A p_j^B \forall (i, j)$), then in presence of interactions among parts of the system entropy will be defined as [10]

$$S_q(A+B) = S_q(A) + S_q(B) + (1-q) S_q(A) S_q(B).$$

Since the expression in curved brackets is identical to the Tsallis distribution [10], we will equate η with q and thus connect to the experimentally determined value of β

$$q = \eta = \frac{1}{2 - \beta} \quad (1.48)$$

Let us define the entropic index within the frame of our model. Assuming the system to be in a trap of depth E_i , the barrier height is $E_t = \eta E_i$ [9], the nearest stable configuration is E_{i+1} , and the barrier height is E_{t+1} , as illustrated in fig. 1.6. We define the entropic index as

$$\eta = q = \frac{E_t}{E_{t+1}} = \frac{1}{1 + \frac{\Delta E}{E_t}}. \quad (1.49)$$

This definition enables us to consider the entropic index from the point of view of potential barrier-height fluctuations with respect to the previous barrier. When $0 < \eta < 1$ the next barrier towards a more stable configuration is higher than the previous barrier, the waiting time to release system from the trap will be longer.

1.5 Conductivity

The electrical conductivity, σ , measures the ability of the material to conduct electric current when an electrical potential difference is applied across this material, which makes charged particles move. Typically, the charge carriers are represented by electrons or holes, but in some materials ions can conduct electrical current. The expression for conductivity can be deduced from Drude model which was developed in 1900s by Paul Drude to explain the transport properties of materials, especially metals

$$\sigma = n_e e \mu_e + n_h e \mu_h,$$

where n_e, n_h are the electron and hole concentrations, cm^3 , μ_e, μ_h are their mobilities, $\text{cm}^2/(\text{V}\cdot\text{s})$, and e is the charge they carry, $e = 1.602 \times 10^{-19} \text{ C}$. The value of the conductivity allows us to classify materials as metals, which have high conductivity, $\sigma \geq 10^3 \frac{\text{S}}{\text{cm}}$, insulators with $10^{-12} \leq \sigma \leq 10^3$ and semiconductors with $\sigma \leq 10^{-12} \frac{\text{S}}{\text{cm}}$. To be efficient, good conductors should have high mobility of the charge carriers, which basically characterizes the transport property of the material, and a high enough concentration of charge carriers. Although the majority of organic materials have a low concentration of carriers, it can be increased by injection. It was established by Devos and Lannoo [11] that π -electron (holes), which contribute most to the overall conductivity, are coupled with

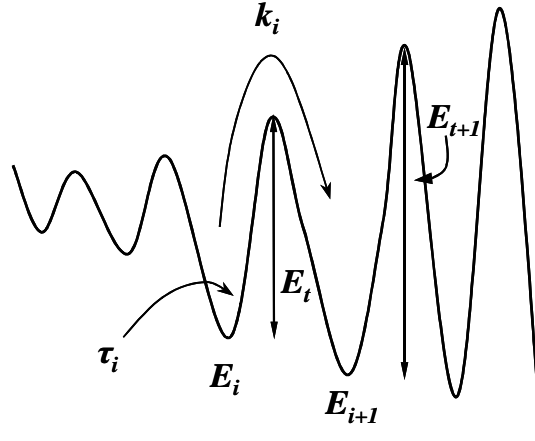


Figure 1.6: Schematic representation of relaxation process with fluctuating potential barrier.

phonons. This coupling, λ , is inversely related to the number of atoms in the molecule involved in π -states, $\lambda \sim N_{\pi}^{-1}$. So, the charge carriers in molecules with large core will be affected less by the motion of the core than that of in molecules with small core. It follows that charge carriers will follow the motion of molecules and their kinetics may be described by the same model that applies for relaxation of molecules. What happens with the charge carriers? They will move until trapped and temporarily immobilized while molecules rearrange themselves. They will contribute again to the conductivity when they escape. In such a way the same relaxation kinetics characteristics will become apparent in the conductivity. The equation of motion for charge carriers in an electric field is given by Langevin equation

$$m \frac{d\mathbf{v}}{dt} = e\mathbf{E} - \frac{m}{\tau} \mathbf{v},$$

where m is the mass of the charge carrier, e is its charge and τ is the relaxation time or so called "mean free time". The steady state solution gives a following expression

$$\mathbf{v} = \frac{e}{m} \tau \mathbf{E} = \mu \mathbf{E}. \quad (1.50)$$

Consequently, the charge carrier will be defined in terms of relaxation time

$$\mu = \frac{e}{m} \tau. \quad (1.51)$$

Since charge carriers will be coupled to the motion of the molecules, we may assume that the mean free time has the same functional form as the relaxation kinetics of the molecules, and its solution in terms of Mittag-Leffler function,

$$P(t) = E_\beta \left(- \left(\frac{t}{\tau} \right)^\beta \right) = \sum_{k=0}^{\infty} \frac{(-1)^k \left(\frac{t}{\tau} \right)^{\beta k}}{\Gamma(1 + \beta k)},$$

which gives the dispersion parameter value and the value for the charge carrier relaxation time. As mentioned above, the dispersion parameter, β , is connected with the entropic index, which describes the behaviour of the energy landscape of the system. Having strong electron-phonon coupling we expect the dispersion parameter to be the same for structural and charge carrier relaxations because we deal with one material. Using this approach and functional form of $P(t)$, the mobility of the quasifree charge carriers can be calculated directly from experimental data, without additional assumptions [12].

1.6 Scope of this thesis

The structure-dynamics-function relation at a microscopic scale is central to understanding the behavior of materials and how they can be improved. The unique structure of discotic mesogen leads to the formation of ordered arrays that consist of ordered 2D hexagonal structure composed from the molecular cores and a space in between filled with liquid-like tails. The presence and the length of the tails appear to determine the temperature range of the liquid crystalline phase [13,14]. Coexistence of such structural order and disorder is reflected in the dynamics where, perhaps not surprisingly, the conventional description based on Gaussian diffusion fails.

It becomes especially visible with quasielastic neutron scattering (QENS) since neutrons follow changes in the behavior of system over quite wide time range and space volume. The generally accepted treatment of QENS implies the separation of elastic and quasielastic motions that is justified when interaction among different parts of the system is negligible. However, discotic liquid crystals are very dense substances and the effects of interaction are essential. Therefore, in order to take into account interactions among different parts of the system we have used a different approach, which assumes static disorder at the beginning followed by hierarchical relaxation. The model we have used for interpretation, combined with the fractional diffusion equation, gives the fundamental parameters which characterize the behavior of system in time and space. Since this approach describes the QENS data well, we have extended its application to the longer timescales with Neutron Spin-Echo spectroscopy that has given us results that are physically consistent with those of QENS.

This anomalous behavior may have its origin at a more fundamental level, so we have performed classic MD simulations to include the influence of thermal motion on the instant energy profile and calculated electronic structure using DFT. Although the model, which has been used for calculation, was simplified the calculation results for the energy profile agree well with those obtained from QENS. The energy profile deviates from the classical Boltzmann distribution, which may be expected for such soft condensed matter as discotic liquid crystals when the interactions among

different parts of the system are present. Such a result leads to an important conclusion. The motion of the electrons, or charge carriers in general, will be significantly altered due to presence of hierarchically constrained dynamics and the underlying geometry. This influence should be taken into account when calculating the electronic properties of discotic liquid crystals.

Another important question is: to what extent will the tails affect the vibrational dynamics of the cores since the core vibrations have the considerable impact on the motion of the charge carriers. We have studied these vibrations with inelastic neutron scattering TOSCA, an instrument at ISIS, Oxfordshire, UK. It appeared that unlike the slower motions, fast vibrations of the core and tails are decoupled. Only the first carbon in tails makes contribution to the core vibrations. Therefore, molecular vibrations of the tails can be excluded from consideration with comparison of the slow thermal motion where the tails play important role in dynamics .

What will happen in system when some other compound with different symmetry, such as TNF, is added? Bearing in mind the influence of the structure on the dynamics we would expect some changes with respect to pure substance. But those changes will depend on the position of TNF. Its location between discs should modify significantly the electronic structure of the cores, decreasing the π overlap. A position of TNF among the tails should slow down both the tail and core motions resulting in improved time averaged π orbital overlapping and, therefore, allowing charge carriers to travel further on average. We have established by means of different techniques that TNF is located among the tails. We also anticipate in this case a slowing down the molecular dynamics. This slowing has been confirmed using QENS and comparing the results for HAT6/TNF with that of pure HAT6. Since the model we have used for the interpretation of the dynamics gives information about changes that occur in the system in terms of energy fluctuations, we can understand those changes on more fundamental level.

If one assumes coupling between molecular motions and movement of the charge carriers a description of the conductivity decay, which reflects the charge carriers motion, can be made using the same model as that for the molecular dynamics interpretation. Its application has given the same fundamental parameter for the carrier mobility that characterizes dynamics of the molecular system itself on the same relevant lengthscale. Therefore, using such a model with strong coupling between molecules and charge carriers, the molecules and charge carriers can be described by the same model, which is sensitive to the structure and reflects the most essential changes in dynamics brought about by it.

Bibliography

- [1] http://en.wikipedia.org/wiki/Renewable_energy
- [2] S. Chandrasekhar, B.K. Sasashiva, A.K.Suresh, *Pramana*, **9**, 471, 1977.
- [3] T. Dahl, *Acta Chemica Scandinavica*, **48** (2), 95-106, 1994.
- [4] R.J. Bushby and O.R. Lozman, *Current opinion in colloid and interface science*, **7**, 343-354, 2002
- [5] M. Beé, *Quasielastic neutron scattering: principles and applications*. IOP Publishing Ltd, Bristol, 1988.
- [6] L. van Hove, *Phys. Rev.*, **95**, 249, 1954.
- [7] J.C. Phillips, *Rep. Prog. Phys.*, **59**, 1133-1207, 1996.
- [8] R. Metzler and J. Klafter, *Phys. Rep.*, **339**, 1-77, 2000.
- [9] Yu. A. Berlin, A. L. Burin, and S. F. Fischer, *Chem. Phys.*, **220**, 25, 1997.
- [10] S.R.A. Salinas and C. Tsallis, *Braz. J. Phys.*, **29**, 1, 1999.
- [11] A. Devos, M. Lannoo, *Phys. Rev. B*, **58**, 8236, 1998.
- [12] J.M. Warman, A.M. van de Craats, *Molecular Crystals and Liquid Crystals*, **396**, 41-72, 2003.
- [13] P. Etchegoin, *Phys. Rev. E*, **56**, 538, 1997
- [14] I. Paraschiv, P. Delforterie, M. Giesbers, M. A. Posthumus A. T. M. Marcelis, H. Zuilhof, E. J. R. Sudhölter, *Liquid Crystals*, **32**, 977, 2005.

Chapter 2

Experimental techniques and calculation methods

Understanding of the liquid-crystal dynamics is a versatile matter, which involves the consideration of the influence of the structure as well. Therefore, application of complementary techniques would be desirable because this kind of approach may reveal significant details that should be taken into account but may be omitted when only one technique is used. In this chapter a description of different techniques, which were used for characterization of structural and dynamical properties, is presented briefly. A more detailed description can be found elsewhere (see references).

2.1 Structure

Bragg's law determines the structure of materials from a scattering experiment,

$$2d \sin 2\theta = n\lambda, \quad (2.1)$$

where d is the spacing between two scattering planes, θ is angle between the incident beam and the scattering plane, λ is the wavelength of incident beam and n is an integer [1]. Waves that satisfy this law interfere constructively and contribute significantly to the intensity of reflected waves, fig.2.1. Bragg's law is used extensively in various diffraction experiments.

2.1.1 X-ray diffraction

The molecular arrangements in different samples were analysed with a Bruker Nonius D8-Discover X-ray diffractometer using Cu K α radiation and equipped with a home-built capillary oven. The HAT6 sample was placed into an X-ray capillary with a 0.7 mm internal diameter and then the capillary tube was placed inside a vertically aligned graphite tube with a transversal hole, which allows the incident X-ray beam to cross freely. The temperature of the graphite tube was controlled by a system formed by a thermo-couple connected to a PID controller and a power supply, which acts as a fast-response online oven ranging from room temperature to 350°C. XRD measurements for HAT6-TNF were made at room temperature. The X-ray measurements were carried out with a sample to detector distance set to 6 cm and spectra were recorded for 30 min.

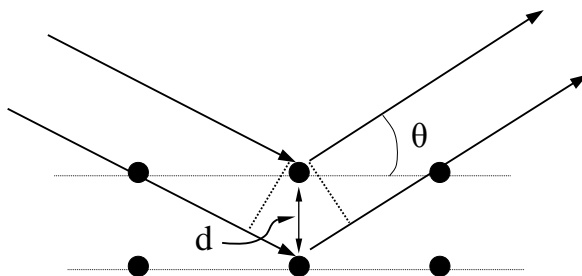


Figure 2.1: Illustration of the Bragg law.

2.1.2 Neutron diffraction

Although IN6 is an inelastic and quasielastic scattering instrument, it was possible to obtain diffraction pattern of reasonable quality by taking the integrated elastic-peak intensity as a function of detector angle.

2.1.3 Density functional theory (DFT)

Density functional theory is used to calculate electronic structure of the molecules. In many-body electronic structure calculations the nuclei of molecules are fixed generating static external potential V , in which electrons move. A stationary electronic state is described by wave function $\Psi(\vec{r}_1, \dots, \vec{r}_N)$ fulfilling the many-body Schrödinger equation

$$H\Psi = [T + V + U]\Psi = \left[\sum_i^N -\frac{\hbar^2}{2m}\nabla_i^2 + \sum_i^N V_i(\vec{r}_i) + \sum_{i<j}^N U(\vec{r}_i, \vec{r}_j) \right] = E\Psi,$$

where H is the electronic molecular Hamiltonian, N is the number of electrons, U is the electron-electron interaction. The T and U operators are called universal operators since they are the same for any system, while V is the system dependent operator. The difference between the single-particle problem and the many-body problem arises from interaction term U .

The DFT provides the way to map the many-body problem onto a single-body problem without U . In DFT the key variable is the particle density, $n(\vec{r})$, which is expressed as

$$n(\vec{r}) = N \int d^3r_2 \int d^3r_3 \dots \int d^3r_N \Psi^*(\vec{r}, \vec{r}_2, \dots, \vec{r}_N) \Psi(\vec{r}, \vec{r}_2, \dots, \vec{r}_N)$$

Hohenberg and Kohn proved in 1964 that the relation expressed above can be reversed to a given ground state density, $n_0(\vec{r})$ it is in principle possible to calculate the corresponding ground state wavefunction, $\Psi_0(\vec{r}_1, \dots, \vec{r}_N)$. In other words, Ψ_0 is a unique functional of n_0 , $\Psi_0 = \Psi_0[n_0]$. Then one uses instead of the Schrödinger equation a Kohn-Sham equation for an auxiliary non-interacting system

$$\left[-\frac{\hbar^2}{2m} \nabla^2 + V + \int \frac{e^2 n_s(\vec{r}')}{|\vec{r} - \vec{r}'|} d^3r' + V_{XC}[n_s(\vec{r})] \right] \phi_i(\vec{r}) = \epsilon_i \phi_i(\vec{r}),$$

which gives solutions in terms of orbitals ϕ_i that reproduce the density of the original interacting system

$$n(\vec{r}) \equiv n_s(\vec{r}) = \sum_i^N |\phi_i(\vec{r})|^2.$$

The term V_{XC} is the exchange correlation potential that includes all the many-particle interactions, the third term in this equation is Hartree term describing the electron-electron Coulomb repulsion. Since the Hartree term and V_{XC} depend on $n(\vec{r})$, which depends on the $\phi_i(\vec{r})$, which in turn depend on the sum from last three terms, the problem of solving the Kohn-Sham equation has to be done in a self-consistent (i.e. iterative) way. Usually one starts with an initial guess for $n(\vec{r})$, then calculates the corresponding sum from three terms and solves the Kohn-Sham equations for $\phi_i(\vec{r})$. From these one calculates a new density and starts again. This procedure is then repeated until convergence is reached [2].

2.2 Dynamics

2.2.1 Quasielastic neutron scattering (QENS)

Time of flight spectrometer, IN6

QENS spectra were obtained using the IN6-time of flight spectrometer, fig. 2.2, at Institute Laue Langevin in France with an incident wavelength of 5.9Å and standard sample temperature-control. Time of flight is the general method of measuring the neutron flight time between two points to determine energy. Selection of the velocities from the mixed velocities of the incident neutron beam was made by crystal monochromator. The angles and positions of the crystals are arranged in the way that the chopper scans the highest angle monochromator first giving the slower neutrons the required head start. Slight differences in the paths followed by the fast and slow neutrons are also optimised to achieve focusing effects, fast neutrons take the long path whilst slow neutrons take a shorter path. Time focusing forces all neutrons, which have transferred the same amount of energy to the sample, to arrive at the detectors together, regardless of their

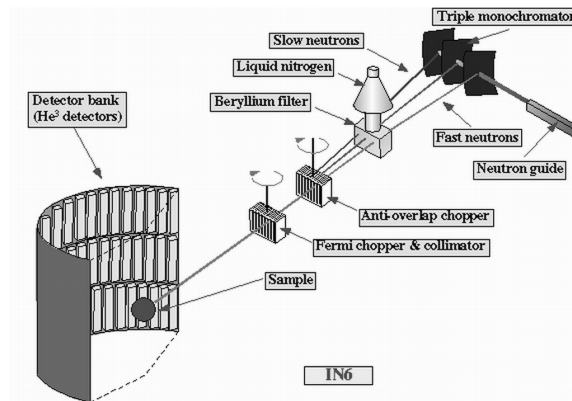


Figure 2.2: IN6 time of flight spectrometer

incident and final energies [3]. Typically, the focusing is made at zero energy-transfer, i.e. the elastic peak.

Neutron Spin-Echo spectrometer, IN15.

Neutron Spin-Echo spectroscopy (NSE) is especially well suited for studies of coherent relaxation phenomena. Other techniques in inelastic neutron scattering obtain data by preparing an incoming beam and analysing the scattered beam. NSE is substantially different. It is based on the determination of changes in neutron velocity. To achieve this the Larmor spin precession is used as a built-in clock attached to each neutron. The neutron flies through a magnetic field in which its spin undergoes the Larmor precession. The total precession angle is proportional to the time the neutron has spent in this field (i.e. inversely proportional to its velocity). Beyond the sample, a coil flips by 180° one component of the neutron spin vector. Then the neutrons fly in a second magnetic field where their spins refocus. The neutrons velocity change is then given by the resulting precession angle. For a neutron beam scattered quasielastically a change in the polarisation beam

is observed. So, it is possible to compare the change in the incoming and outgoing velocities for each individual neutron. For that reason the energy resolution becomes independent of the beam monochromatisation if the neutron energy transfer is determined. This is the unique feature of the method. In NSE the time-dependent Fourier transform $S(Q,t)$ of the sample scattering function is the directly measured quantity and is therefore a valuable tool for quasielastic line shape analysis in slowly diffusing systems [3].

2.2.2 Molecular dynamics simulation

Simulation of molecular dynamics is based on Newton's laws. The force that acts on the i th atom in system can be defined from Newton's motion equation as

$$F_i = m_i a_i, \quad (2.2)$$

where m_i is the mass of the particle and a_i is its acceleration. The force can be expressed as a gradient of potential energy

$$F_i = -\nabla_i U. \quad (2.3)$$

Combining these two expressions one gets

$$-\frac{dU}{dr_i} = m_i \frac{d^2 r_i}{dt^2}, \quad (2.4)$$

which relates the change of the particle position in time to the derivative of potential energy. To obtain trajectories from this expression an integrator is used for a certain statistical ensemble. The obtained trajectories are very sensitive to the initial conditions, so they are difficult to reproduce. We have used NVT ensemble, constant temperature-constant volume canonical ensemble. The temperature for such ensemble is determined by the kinetic energy of the system, because the temperature and the distribution of atomic velocities in a system are related through the Maxwell-Boltzmann equation, and the number of degrees of freedom. To control the temperature during the simulation process we have used direct velocity scaling thermostat. Direct velocity scaling is the way to change the velocities of the atoms so that the target temperature can be exactly matched whenever the system temperature is higher or lower than the target by some amount. The obtained trajectories can be converted into desirable physical quantity [4].

So, the expression 2.4 determines the displacement of molecules through the interactions among molecules. In a molecular dynamics simulation the interactions have been implemented using different force fields. The type of force field is chosen by taking the properties of molecules into account, such as its hybridization state and environment. We have chosen for our study COMPASS force field that is the *ab initio*-based force field. Parameters for this force field have been obtained initially by fitting to *ab initio* potential energy surfaces. Then, they have been optimized to fit the condensed phase properties. The potential energy surface is determined by energy expression as a function of molecular coordinates and structure

$$U_{total} = U_{bond} + U_{cross-term} + U_{non-bond},$$

where U_{bond} is the energy of bond interactions, such as bond stretching, bending, torsion and out-of-plane interactions, $U_{cross-term}$ takes into account the bond or angle interaction caused by nearby molecules, $U_{non-bond}$ includes van der Waals and Coulomb interactions. The refinement of van der Waals parameters is essential when simulating dynamics of condensed phase.

2.2.3 Dielectric relaxation spectroscopy (DRS)

Dielectric relaxation spectroscopy examines interaction of the sample with a time-dependent electric field. The net polarization is expressed in terms of a frequency-dependent complex permittivity that characterized amplitude and relaxation time of charge-density fluctuations within the sample. These fluctuations arise from the reorientation or from the rotation of the permanent dipole moments of the individual molecules. The timescale of such fluctuations depends on the sample and relaxation mechanism. DRS is especially sensitive to intermolecular interactions [5].

2.2.4 Calculation of molecular vibrations

To calculate vibrational frequencies and intensities we have assumed that molecules represent point masses on spring with harmonic interaction potential. The forces acting on such point masses are proportional to displacement of atoms

$$F_i = -\lambda q_i,$$

where q_i is set of generalised coordinates. The force can be expressed as

$$F_i = \ddot{q}_i.$$

Then combining both expressions one gets

$$\ddot{q}_i + \lambda q_i = 0, \quad i = 1, 2, \dots, 3N$$

Solution of this equation is

$$q_i = A_i \cos(\lambda^{1/2}t + \delta),$$

where A_i is amplitude, $\lambda^{1/2}$ is frequency and δ is phase that are determined by the initial conditions. This frequency represents a normal mode at which molecules vibrate after deformation. The set of such normal modes is unique for each structure.

The normal modes and frequencies may be obtained from the matrix of second derivatives, the Hessian matrix, of a molecular system

$$H_{ij} = \frac{\partial^2 E}{\partial q_i \partial q_j},$$

where E is the total energy of the system. The normal mode frequencies are directly related to the eigenvalues and the normal modes to the eigenvectors of this matrix.

2.2.5 TOSCA

TOSCA is an indirect geometry time-of-flight spectrometer at ISIS, Oxfordshire, UK. The time-of-flight technique is used to analyse the energy of the incoming neutrons. The spectrometer is built in such a way that only neutrons scattered from sample under 45° or 135° collide with graphite crystal. Since the scattering angle and the distance between planes in a graphite crystal stay the same, then according to 2.1 only one wavelength will be scattered by the crystal. Then neutrons will be transmitted by beryllium filter, which acts as long wavelength pass filter, and are detected by ^3He filled detector tubes.

The energy transferred from neutrons to sample, E_{trans} , is defined by

$$E_{trans} = E_i - E_f,$$

where E_i and E_f are incident and final energies of the neutrons respectively. The energy of the neutrons can be represented through the neutron mass, m , and velocity, v , as

$$E = \frac{mv^2}{2},$$

then the neutron velocity will be expressed

$$v = \sqrt{\frac{2E}{m}}.$$

Knowing *travel time = distance/velocity*, we can define the neutron travel time

$$T = t_i + t_f = \frac{L}{\sqrt{2E_i/m}} + \frac{l}{\sqrt{2E_f/m}}.$$

Since the distances L and l are known as well as energies then the travel time uniquely defines the energy transfer to the sample, E_{trans} .

The intensity of inelastic neutron scattering is proportional to

$$S(Q, \omega) \propto Q^2 U_i^2 \exp(-Q^2 U_{total}^2) \sigma$$

The result of the collision between the neutron and the molecule will be significant transfer of momentum and energy, because the masses of the neutron and hydrogen are approximately equal. TOSCA is designed in the way that there is only one value of Q for each energy. U_i is the amplitude of the molecular vibration in particular mode. The exponential term represents Debye-Waller factor, U_{total} is the total mean square displacement of molecule by thermal motion. σ is the inelastic neutron scattering cross section of all the atoms involved in the mode [6].

2.2.6 Conductivity

The HOMO-LUMO gap of the disc core in HAT6 is quite large, 4.5 eV, and that of HAT6-TNF is 2.5 eV. For this reason the number of intrinsic charge carriers in the conduction band is extremely low, which leads to very low background conductivities. This makes it difficult to study the electric properties of such materials directly. That means that additional charge carriers should be introduced. It is possible to do so with some radiation that excites system under study and creates an excess of charge carriers.

The study of the conductivity of pure HAT6 and the charge transfer compound, HAT6-TNF, was performed with Pulse Radiolysis Time-Resolved Microwave Conductivity (PR TRMC) technique, fig. 2.3. The rapidly oscillating microwave electric field with low strength causes small perturbation in diffusive motion of the charge carriers. Therefore, effects due to such a field will be excluded and that makes this particular method advantageous with comparison to conventional techniques.

The cell with liquid-crystalline material is irradiated with a single pulse of 3 MeV electrons from a van de Graaf accelerator. The shape of the pulse is close to square with variable width. The beam

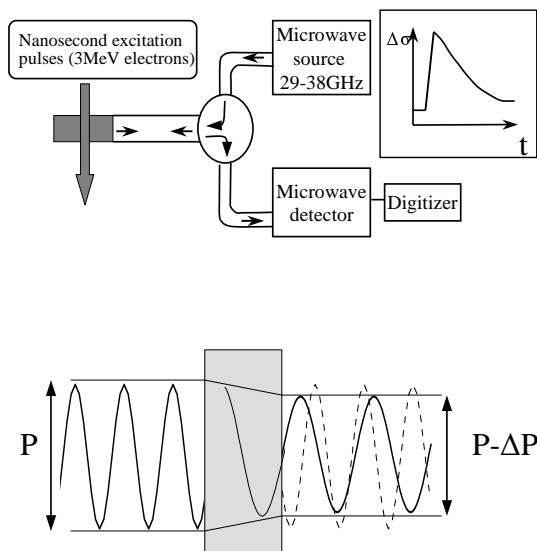


Figure 2.3: Schematic representation of Pulse Radiolysis Time Resolved Microwave Conductivity. In weakly conductive media changes in conductivity are proportional to changes of power.

current can be varied also but usually it is kept close to 4 A. The penetration depth for electrons with such an energy in materials of density 1g/cm^3 is around 15 mm. That is much larger than the sample thickness (3.5 mm) and the half width of the beam cross-section is larger than the size of the sample. This means that the energy deposition and ionisation within sample is close to uniform. The Energy transfer from high energy electrons to the system under study arises via excitations and ionisations along the path of the primary electrons. For an organic material of density approximately 1g/cm^3 ionization events are separated by around 200 nm, and the thermalization distance of the secondary electrons is *ca* 50 Å from a sibling positive ion. Due to these processes the conductivity of the material increases. It is detected as an increase in microwave power absorbed by the sample. The change in conductivity can be measured directly and it is proportional to changes in power

$$\frac{\Delta P}{P} = -AF\Delta\sigma,$$

where F is the fraction of the cell volume occupied by the sample (or the fill factor), A is the sensitivity parameter [7].

Bibliography

- [1] http://en.wikipedia.org/wiki/Bragg_Law.
- [2] http://en.wikipedia.org/wiki/Density_functional_theory.
- [3] http://www.ill.fr/YellowBook/instr_gr/tof.html.
- [4] <http://www.accelrys.com/>
- [5] F. Kremer and A. Schönhalz (eds.), Broadband Dielectric Spectroscopy, Springer, Berlin 2002.
- [6] <http://www.isis.rl.ac.uk/molecularspectroscopy/tosca/>
- [7] J. Piris, Optoelectronic properties of discotic materials for device application, DUP Science, 2004.

Chapter 3

Dispersive kinetics in discotic liquid crystals

3.1 Introduction

Discotic liquid-crystalline systems consist of disk-like molecules that self-assemble into columns as a result of overlap of the π -orbitals of the aromatic cores¹ [2,3]. Electrons and holes hop along the column direction, this having drawn attention to these materials for nanoscale conductive devices. Since the inter-disk hopping occurs on the picosecond timescale [2] and the lifetime of electron-hole pairs is on a nanosecond timescale, we anticipate that dynamics within these timescales will be particularly relevant for conductivity. The conductivity is sensitive to the dynamics of the cores, but the alkoxy tails not only assist the self-assembly (by phase separation of aromatic and aliphatic parts), but also play a crucial role in the dynamics of the cores. We chose QENS because this technique simultaneously follows hydrogen-atom dynamics over these timescales, and length-scales of Ångströms. As it was established by van Hove [4] the neutron scattering function, $S(Q, \omega)$, which is measured in QENS experiment, represents the Fourier transforms over r and t of the pair distribution function in space and time, $G(r,t)$. In general it describes the correlation between the presence of the particle in the position $r'+r$ at time $t'+t$ and the presence of the particle in position r' at time t' . Under certain conditions it can be simplified and represents average density for homogeneous statistically independent systems. Such an approximation allows us to use classical models for $G(r,t)$ and to depict $S(Q,\omega)$ as a sum of the elastic and quasielastic parts [5]. This assumption will be no longer valid for complicated systems [6] in which interaction within the system should be taken into account. Discotic liquid crystals are a very good example of complicated systems where the conventional, simplified, approach fails.

For data interpretation we use the model for relaxation kinetics in a correlating system that takes into account the interaction between different parts of system and correlation effects. Combined with the fractional diffusion equation it allows us to construct the space-time correlation function for the system, $G(r,t)$. Additional analysis on the subject of the hierarchical order of relaxation has been performed for data obtained from Neutron Spin-Echo (NSE) experiment.

¹Part of this chapter is based on paper: O. Kruglova, F. M. Mulder, S. J. Picken, J. A. Stride, I. Paraschiv, H. Zuilhof and G. J. Kearley, *J. Chem. Phys.*, **2006**, submitted

3.2 Experimental techniques

QENS spectra for HAT6 were obtained using the IN6 spectrometer at the Institute Laue Langevin in France with an incident neutron wavelength of 5.9Å and standard temperature-control. Measurements were performed at a temperatures of T=340K, 352K, 358K, 364K and 370K for the protonated samples and at T=367K for the tail-deuterated analogue. Formally, 340K corresponds to the crystalline \rightarrow liquid crystalline phase transition and T=370K to the liquid crystalline \rightarrow liquid phase transition. Data were corrected using standard algorithms and analyzed using locally written routines. We have extended our previous measurements on this system by using samples in which the alkoxy tails are deuterated [7] in order to highlight the dynamics of the aromatic disk cores.

Sample alignment was achieved by placing the sample in a shallow (0.5 mm) rectangular recess of an aluminium plate that formed one half of the sample container. An aluminium cover-plate that was 1.5mm smaller than the recess was placed over the sample and then displaced, under slight pressure, to provide mechanical shear on the sample. In practice it was found easier to perform the alignment operation within the temperature-control device. This was used to first melt the sample in the recess and then cool to just below the melting point before applying the shear. The container was then sealed with the cover plate in place, and the sample environment closed. Intermediate scattering spectra were obtained using the IN15 spectrometer at the Institute Laue Langevin in France. In order to obtain values of momentum transfer: $Q=0.1$ and 0.2 \AA^{-1} , measurements were performed with an incident wavelength $\lambda=10.5 \text{ \AA}$ at scattering angles every 10° and 20° , temperatures T=348, 368 K for aligned sample and T=348, 358 and 368K for unaligned one.

3.3 Results and discussion

3.3.1 Dynamics

As was mentioned in the introduction, the conventional approach and treatment of the data fails when dealing with such complicated system as liquid crystals. As can be seen in figure 3.1 HAT6 with deuterated tails mainly gives a signal from the 6 core protons. Figure 3.1 represents fitting of neutron scattering data for HAT6 having such deuterated tails with δ -function embodying the elastically scattered part and two Lorentzian curves depicting contributions to the quasielastic part of curve from two kinds of core motions: in-plane and out-of-plane. Such model was used for a tail protonated sample that mainly showed the motions of the tails [2]. One can clearly see from the picture that agreement between this model and data is rather poor. The tails, which are liquid-like, were deuterated to reduce their contribution to the signal. In this case $S(Q, \omega)$ will reflect mostly the response from the cores, which are ordered in a hexagonal lattice and, therefore, should follow the conventional diffusion equation on lattice [15]. Therefore, this example becomes especially illustrative. Of course, fitting with three or even more Lorentzian functions would give better fit although the physical meaning of such an introduction would be ambiguous. The liquid-like contribution from the alkoxy tails is largely removed in the sample with deuterated tails, and spectra from this sample show a great deviation from the simple two-Lorentzian quasielastic profile. For interpretation of our data we have used a different approach and a model for relaxation kinetics in a correlating environment. To analyze data in the time domain, $S(Q, \omega)$ has to be converted to the time domain using an inverse Fourier transform (IFT) and dividing by the IFT of the measured resolution function to obtain the pure response of the system. This allows us not

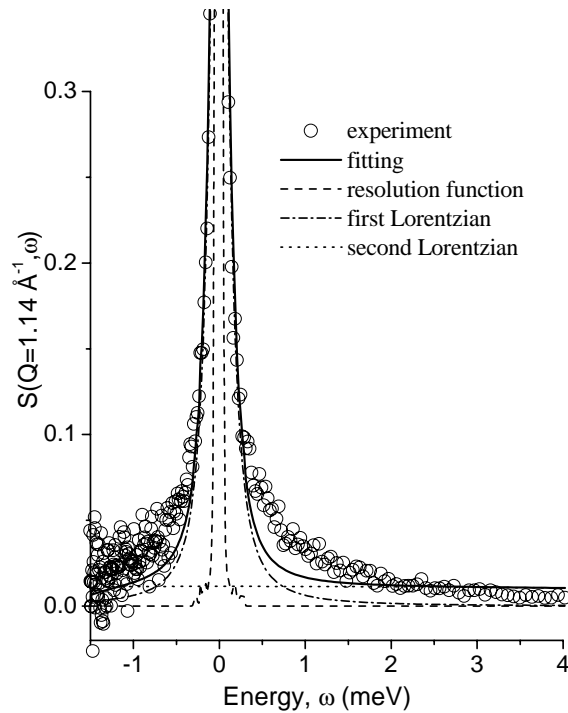


Figure 3.1: Fitting of neutron scattering function of HAT6 with deuterated tails, measured at $T=367\text{K}$, $Q=1.14 \text{ \AA}^{-1}$, with 2 Lorentzian functions. The difference between real data shape and fitted shape is clear. Evidently, the model with two simple motions does not describe the behaviour of system properly.

to separate signal on elastic and quasielastic parts and to study the evolution of the system as a whole. All intermediate scattering functions, $F(Q, t)$, have non-exponential slopes, fig. 3.2, this fact indicates that the motion of molecules in the system is very complex. Our interest here is in the time dependent entanglement of the alkoxy tails, and how this affects the dynamics of the aromatic cores.

For the fitting procedure we have used 25 terms from sum of equation (1.42) since more than 25 terms does not change overall fitting lineshape. Figure 3.2 illustrates the result of fitting the IFT of QENS by equation 1.42 with τ , β as free parameters. The behavior of HAT6 is described quite well by expression 1.42. This indicates that we are essentially probing a single relaxation process of the core hydrogen atoms, reflecting a system of collective motion, in the data.

By examining the value of τ as a function of momentum transfer, Q , (Figures 3.3 and 3.4) we can follow the changes of the relaxation time and see how it depends on the temperature and phase of the discotic material. Figure 3.3 presents the dependences of τ on Q at $T=340\text{K}$ and 370K for the protonated sample (phase transition temperatures HAT6) and at $T=367\text{K}$ (phase transition

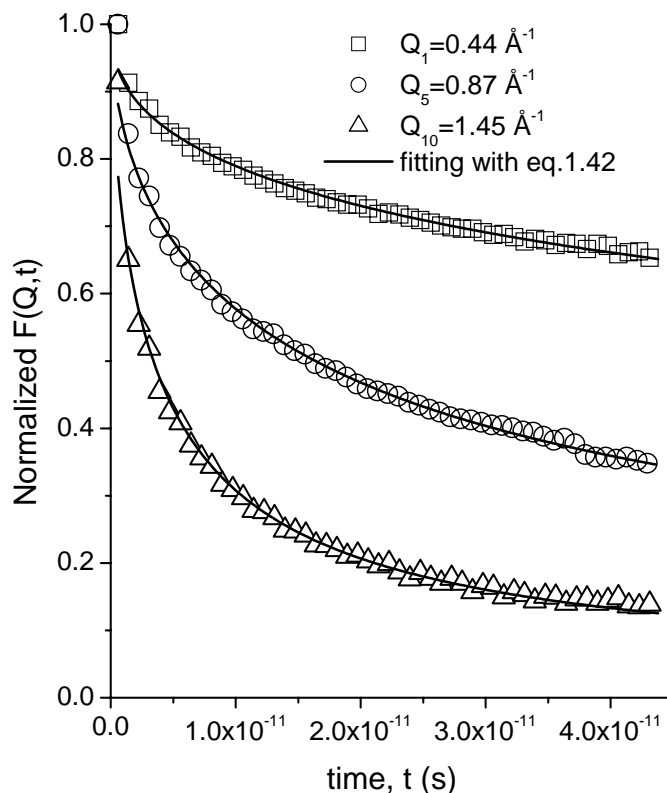


Figure 3.2: Intermediate scattering function $F(Q, t)$ for HAT6 at $T=358\text{K}$ for $Q=0.44, 0.87, 1.45 \text{ \AA}^{-1}$ fitted with equation 1.42. As it can be seen from graph fitting is rather good.

temperature) for HAT6 with deuterated tails. The most striking feature on this figure is that the behavior of HAT6 with protonated tails at 340K resembles that of the core motion coming from the sample with deuterated tails at 367K until $Q \sim 0.66 \text{ \AA}^{-1}$, which is approximately the disc-core diameter. This would indicate that at a lengthscale shorter than the core diameter we see the fast local relaxation of the chains in the protonated tail sample, and at longer scales we see more the effect of the core dragging on, and confining, the entangled tails. Comparing this with $\tau(Q)$ at 370K one can tell that the relaxation time becomes significantly faster and it is possible that motion of the tails as visible in the protonated sample plays a determinative part. The cores are still slower as can be seen from the deuterated tail sample at a similar temperature. It is interesting to see how the relaxation time will change in the temperature range $340\text{K} < T < 370\text{K}$, figure 3.4, where the system is in the liquid crystalline phase. We see on figure 3.4 for protonated tail sample that the value of the relaxation time decreases when the temperature increases. In the region, $Q > 0.6 \text{ \AA}^{-1}$, values of the relaxation time are almost the same except for $T=352\text{K}$ and they tend to diverge for $Q < 0.6 \text{ \AA}^{-1}$. It is likely that at $T=352\text{K}$ the effect of the core motion on slowing down the tail motion is still pronounced, although somewhat reduced.

The dynamics in the discotic core-tail system are clearly correlated due to the chemical bond

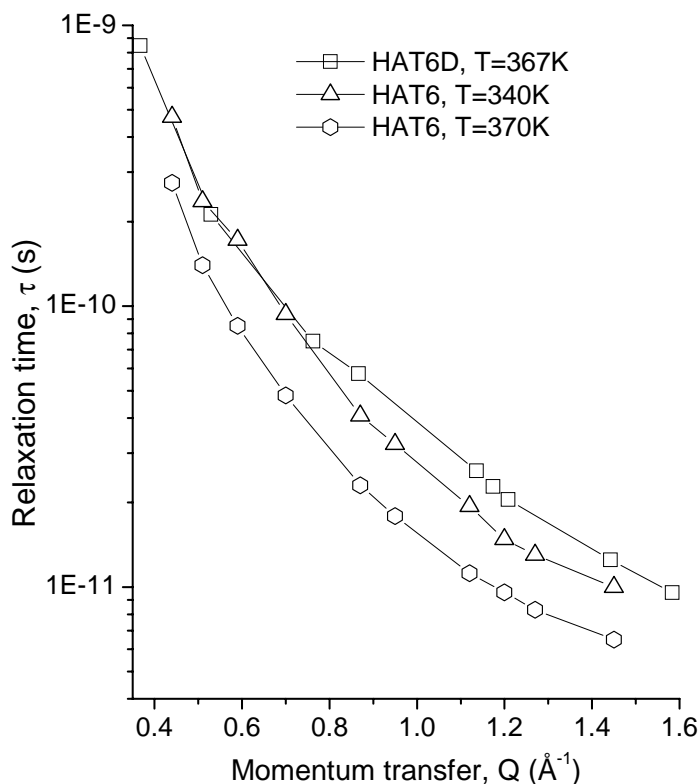


Figure 3.3: Relaxation time, t , dependence with momentum transfer, Q , for HAT6 with deuterated tails at $T=367\text{K}$ and HAT6 at temperatures close to phase transition $T=340\text{K}$ (crystalline→liquid crystalline) and $T=370\text{K}$ (liquid crystalline→isotropic)

between them, the detailed dynamics of the tails not being simply additive to that of the cores. Figures 3.5 and 6 represent change in dispersion parameter, β , with momentum transfer, Q . The dispersion parameter increases gradually with increasing value of Q , but it is always less than 1, which indicates that motion in HAT6 takes place in subdiffusive regime. Again, values $\beta(Q)$ for the sample with deuterated tails and protonated tails at $T=340\text{K}$ are very close to each other for $Q < 0.66 \text{\AA}^{-1}$ which illustrates the importance of the core motion on this lengthscale at low temperatures. As one can see from figure 3.5 the potential-barrier fluctuation of the core is comparable with that of the tails, indicating that the core is not a rigid disc, but rather a mobile structure exploring the energy landscape. The tail motion plays a crucial role at temperatures close the liquid crystalline→isotropic phase transition and, of course, at short lengthscales. Since the relaxation in these discotic liquid crystals occurs in the subdiffusive regime ($0 < \beta < 1$) [10], figures 3.5 and 3.6, the entropic index will be $\eta = q < 1$ as predicted by [11-13]. The Tsallis distribution of states indicates the presence of hierarchical order in relaxation and, therefore, the presence of long-range correlations in our system, which vary depending on the lengthscale [14]. This definition enables us to consider the entropic index from the point of view of potential barrier-height fluctuations

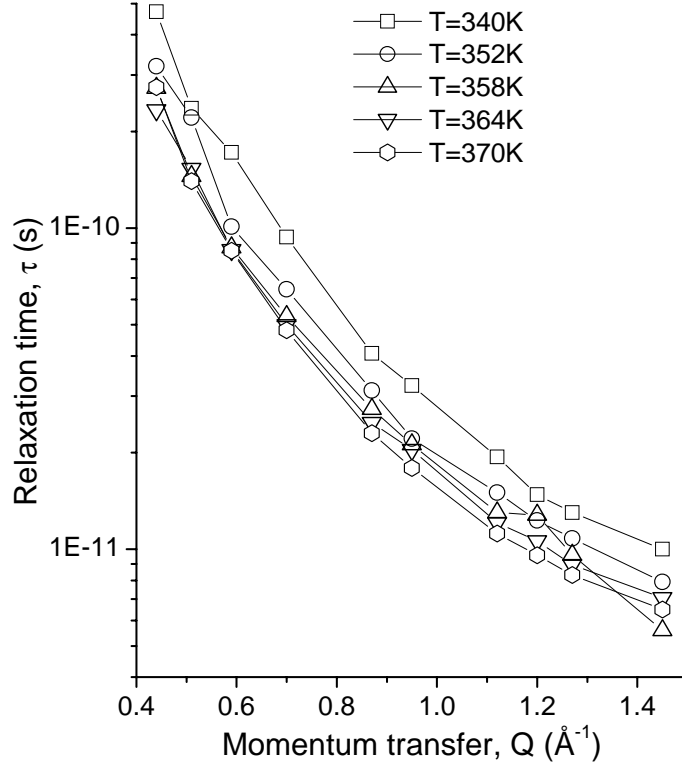


Figure 3.4: Relaxation time τ dependence from momentum transfer, Q , for different temperatures $T=340, 352, 358, 364$ and 370K , protonated HAT6.

with respect to the previous barrier, eq.1.49. When $0 < \eta < 1$ the next barrier towards a more stable configuration will be higher than the previous barrier, the waiting time to release system from the trap will be longer, fig.1.6. The analysis of dispersion and entropic index behavior, figure 3.5 and 3.6 shows that β changes with Q more steeply than η . That means that the system is very sensitive to small parameter changes by which we mean height fluctuations of the potential barrier. Small fluctuations of potential barrier cause prolonged waiting time in potential well compared with simple Brownian diffusion since dispersion parameter specifies the rate of the relaxation time alteration.

It is clear from the fig. 3.3 and 3.4 that the relaxation time, τ , is Q -dependent. This dependence would be a Gaussian distribution function in the conventional approach [15]. However, in our case the shape of the curves is far from Gaussian and normal distributions. Therefore, we might deal with the system where variance of jump length diverges. Such a case in fractional diffusion approach is represented by Lévy distribution [10]. It is possible that in such a complex system as liquid crystals, the distribution of jump lengths will obey Lévy distribution, which is a generalization of normal and Gaussian distributions,

$$\lambda(Q) = e^{-aQ^\alpha}, \quad (3.1)$$

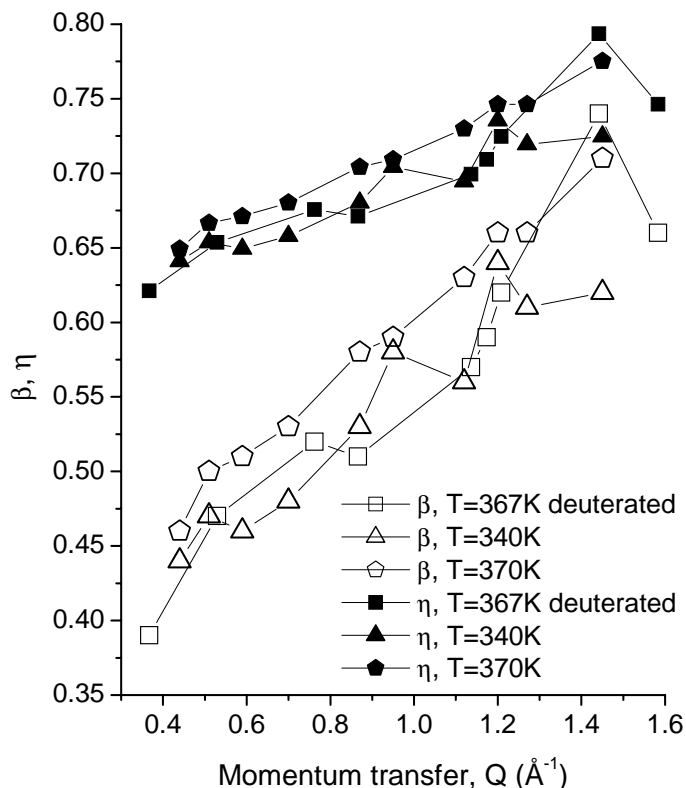


Figure 3.5: The dispersion parameter β and entropic index η dependences from the momentum transfer, Q , for HAT6 with deuterated tails at $T=367\text{K}$ and HAT6 at temperatures close to the phase transition $T=340\text{K}$ (crystalline \rightarrow liquid crystalline) and $T=370\text{K}$ (liquid crystalline \rightarrow isotropic)

where a is the amplitude parameter and α is Lévy index, which determines the degree of the jump-length fluctuation and varies between $0 < \alpha < 2$ [16]. Figure 3.7 represents fitting of $\tau(Q)$ at different temperatures with a Lévy distribution. Depending on the Q range, lower Q or higher Q , there appear to be two possible jump length distributions within model, since it was possible to obtain a reasonable fit with two different curves. This may be not surprising because the structure of discotic liquid crystals is represented at low Q by larger influence of the more ordered and anisotropic cores and at high Q with only the influence of the more isotropic tails. Possibly, this explains why we have set of two limits of characteristic jump lengths (figure 3.8). The values of both Lévy indexes stay almost constant over the measured temperature range. Although the momentum-transfer value Q at which one would switch the distribution is temperature-dependent, one may conclude that the change in the rate of the characteristic jump happens around the lengthscale of the alkoxy tails or core diameter.

Knowing how the waiting times and jump lengths are distributed, and using the solution of the fractional diffusion equation [10], we can construct the van Hove correlation function from a general expression, eq.(1.25), where $s = \sigma + i\omega$ - complex frequency, $w(s)$ -transition probability and

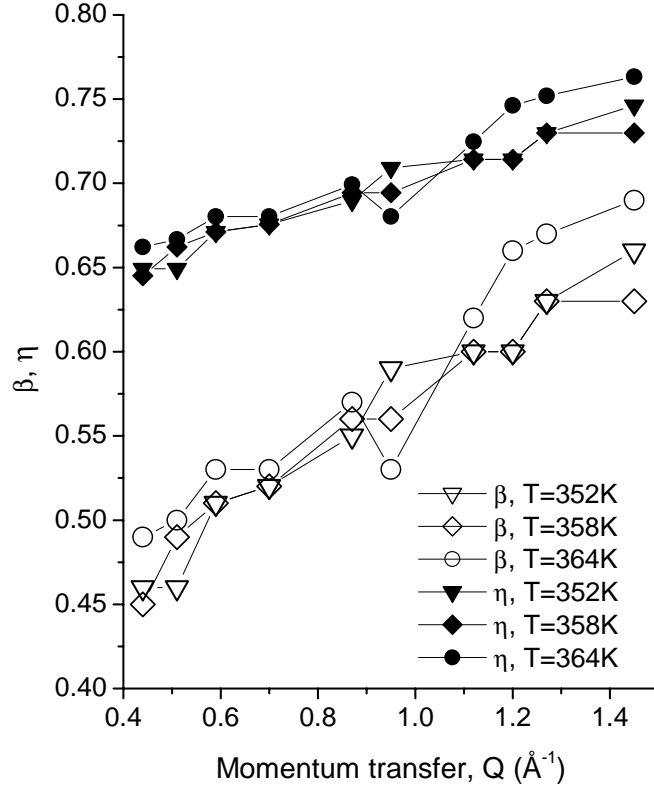


Figure 3.6: Dispersion parameter β and entropic index η dependences from momentum transfer Q for HAT6 in "true" liquid crystalline phase at $T=352, 358$ and 364K .

$\psi(Q, s)$ -probability distribution function of making a jump of reciprocal length Q in the frequency interval s to $s + ds$. The Mittag-Leffler function, which corresponds to the survival probability at initial state, has direct representation in a frequency domain and is equal to [1]

$$\tilde{P}(s) = \frac{s^{-1} (\tau s)^\beta}{1 + (\tau s)^\beta}.$$

The probability distribution function of making jump, $\psi(Q, s)$, is decoupled for ordered arrays, as pointed out by J. Klafter [17]. Since discotic liquid crystals can be treated as ordered arrays we can express the probability distribution function as

$$\psi(Q, s) = w(s) \lambda(Q). \quad (3.2)$$

Then it will be represented in terms of s and Q as

$$\psi(Q, s) = \frac{e^{-aQ^\alpha}}{1 + (\tau s)^\beta}. \quad (3.3)$$

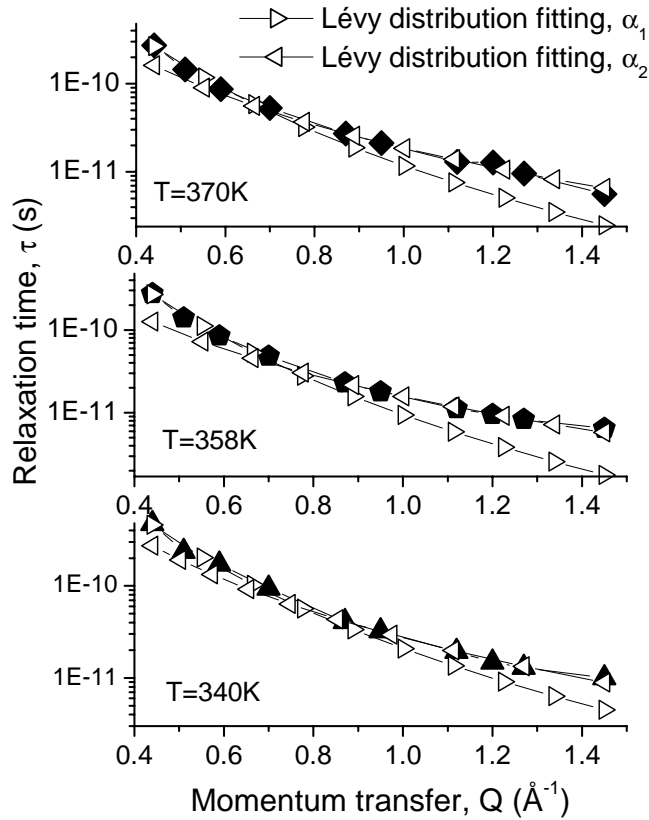


Figure 3.7: Fitting of $\tau(Q)$ with Levý distribution of jump length. Clearly, two limiting geometries may be recognised at higher and lower Q respectively.

Finally, the expression for Laplace-Fourier space transform van Hove correlation function will be

$$S(Q, s) = \frac{s^{-1} (\tau s)^\beta}{1 + (\tau s)^\beta - e^{-aQ^\alpha}}. \quad (3.4)$$

So, the fractional space exponent α and the time exponent (or dispersion parameter) β are fundamental characteristics of the dynamics in liquid crystalline system within the chosen model.

3.3.2 Influence of alignment on relaxation in HAT6

To analyze the quasielastic neutron scattering data from IN6 we have converted $S(Q, \omega)$ into the intermediate scattering function $F(Q, t)$. Although these curves are not smooth and have small humps, it is hard to distinguish whether they represent the artifact of the Fourier transform or appear to be the result of superimposed contributions from individual relaxation channels. Therefore,

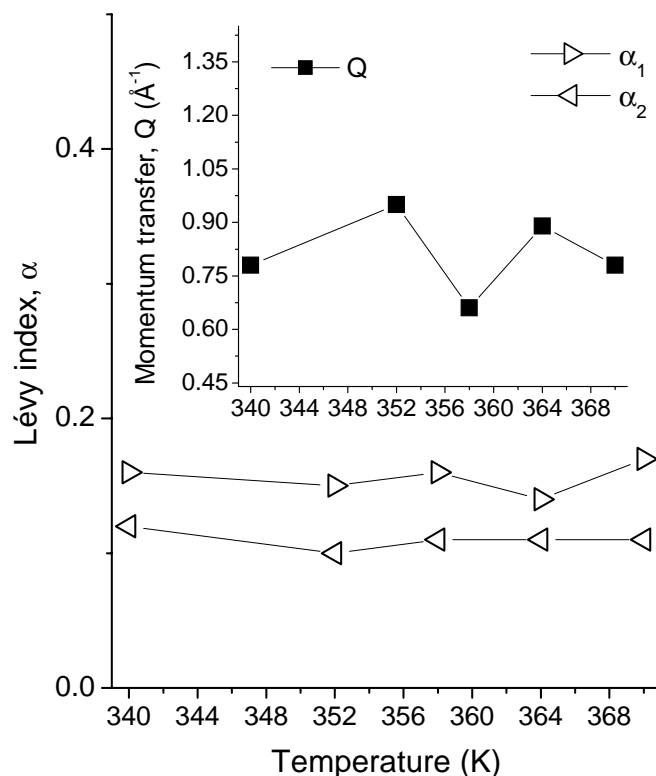


Figure 3.8: Dependence of Lévy index from temperature; inset: temperature dependence of momentum transfer, Q , at which switch of diffusion geometry occurs.

measurements obtained from Neutron Spin-Echo experiment will be particularly valuable for such an analysis since they naturally represent the dependence in the time domain.

Measurements have been performed with aligned and unaligned HAT6. The alignment procedure is described in experimental section. The unaligned sample had a homeotropic orientation in which the molecules form columns perpendicular to the substrate, fig. 3.9. The figure represents Neutron Spin Echo data obtained at two orientations and temperatures, and their fitting with a Mittag-Leffler function. The difference for unaligned and aligned HAT6 is obvious at $T=348\text{K}$. The response from aligned sample decays faster than that of unaligned one. When the temperature approaches the phase-transition temperature the decays become indistinguishable. Comparing the dependence of relaxation time, τ , and dispersion parameter, β , for the two orientations one concludes that in the proximity of phase transition the orientation of the columns ceases to affect the dynamics of the system, figure 3.11.

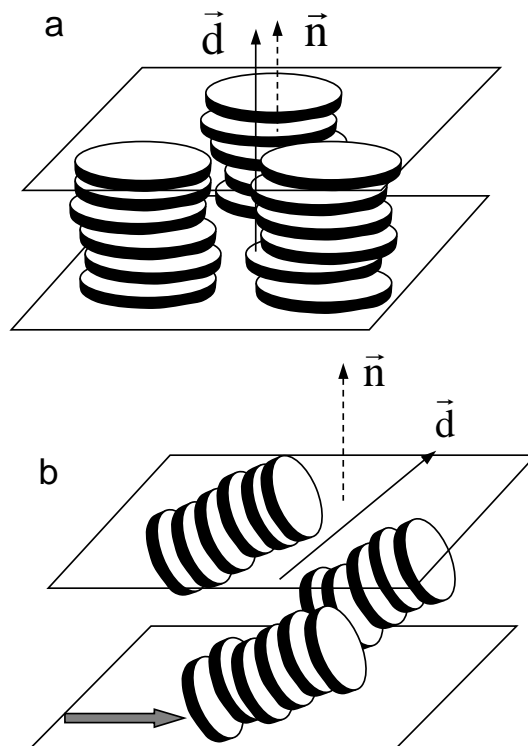


Figure 3.9: Orientations of columns in HAT6: a) homeotropic orientation, which is formed without alignment, plane normal, \vec{n} , is perpendicular to the column director, \vec{d} ; b) orientation which is formed after alignment by shear, plane normal, \vec{n} , forms an angle with column director, \vec{d} .

3.4 Conclusion

The present work demonstrates that the rather simple model for rate processes agrees quite well with the quasielastic neutron-scattering data and gives a physically reasonable model with meaningful parameters. One may state that slow motions of the aromatic cores are controlled by disentanglements of the alkoxy tails whose motions are on a much shorter and faster timescale. Static disorder will define the relaxation path of the system that is quite sensitive to small changes. This will lead to relatively long-range correlations in discotic liquid crystals with a nonextensive character on the scale of the core diameter, which is inherent a strongly hierarchical structure. Such correlations have been taken into account by means of the fluctuation of barriers to neighboring states, providing a good picture of the complex dynamics of discotic liquid crystals and how these vary as a function of temperature and phase. It is likely that many other systems could be reanalyzed in the physical manner of this model that we have described here, which would lead to a better understanding of the evolution of underlying dynamics in terms of the physical parameters that are consistently produced within the model.

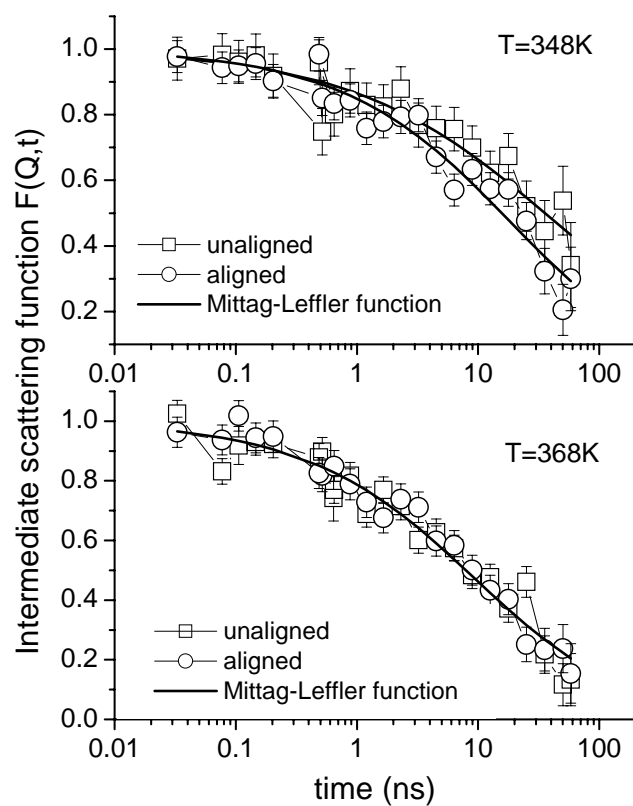


Figure 3.10: Intermediate scattering functions $F(Q, t)$ for aligned and unaligned HAT6 obtained by means of Neutron Spin-Echo spectroscopy for $Q=0.2 \text{ \AA}^{-1}$ at $T=348, 368\text{K}$ and their fitting with Mittag-Leffler function.

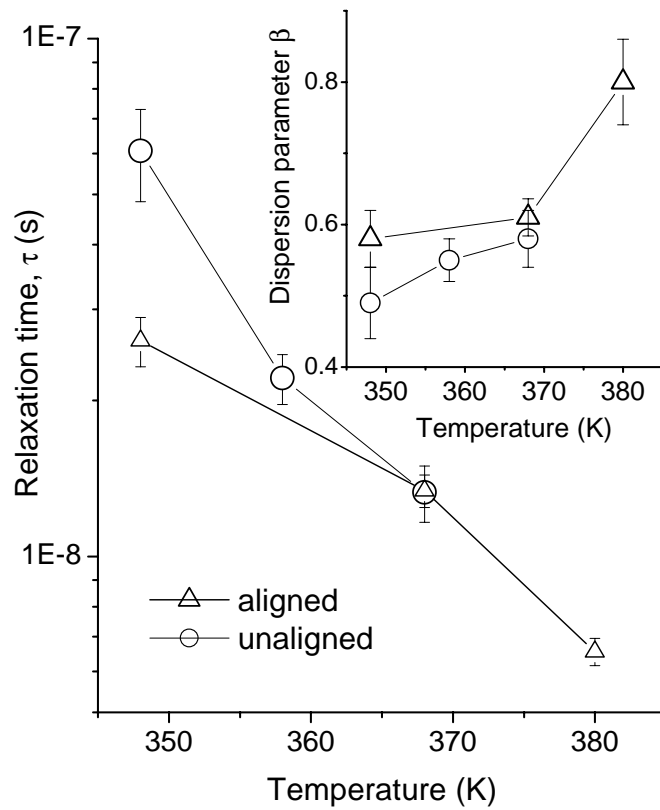


Figure 3.11: Temperature dependence of relaxation time for aligned and unaligned HAT6, $Q=0.2 \text{ \AA}^{-1}$; inset: temperature dependence of dispersion parameter for aligned and unaligned HAT6, $Q=0.2 \text{ \AA}^{-1}$.

Bibliography

- [1] Yu. A. Berlin, A. L. Burin, and S. F. Fischer, *Chem. Phys.* 220, 25 (1997).
- [2] F. M. Mulder, J. A. Stride, S. J. Picken, P. H.J. Kouwer, M. P. de Haas, L. D.A. Siebbeles, and G. J. Kearley, *J. Am. Chem. Soc.* 125, 3860 (2003).
- [3] C. W. Struijk, A. B. Sieval, J. E.J. Dakhorst, M. van Dijk, P. Kimkes, R. B.M. Koehorst, H. Donker, T. J. Schaafsma, S. J. Picken, A. M. van der Craats, J. M. Warman, H. Zuilhof, and E. J.R. Sudhölter, *J. Am. Chem. Soc.* 122, 11057 (2000).
- [4] L. van Hove, *Phys. Rev.*, 95, 249 (1954).
- [5] G. R. Luckhurst and C.A. Veracini, *The Molecular Dynamics of Liquid Crystals*, Kluwer Academic Publishers, 451(1994).
- [6] W. K. Kegel and A. van Blaaderen, *Science*, 287, 290 (2000).
- [7] Alkoxy side chain deuteration was achieved via reaction of 2,3,6,7,10,11-hexa-hydroxy triphenylene with pre-deuterated n-hexyl bromide (Aldrich) under basic conditions (K_2CO_3) in 2-butanone under reflux conditions for 24 hours in a nitrogen atmosphere.
- [8] T. Kanaya and K. Kaji, *Advances in Polymer Science* 154, 87 (2001).
- [9] J. Colmenero, A. Arbe, A. Alegria, M. Monkenbush, and D. Richter, *J. Phys. Cond. Matter* 11, A363 (1999).
- [10] R. Metzler and J. Klafter, *Phys. Rep.* 339, 1 (2000).
- [11] S.R.A. Salinas and C. Tsallis, *Braz. J. Phys.* 29, 1 (1999).
- [12] A. N. Petridis, Drake University physics technical note, drake-phys 2002-1
- [13] J. Naudts, *Rev. Math. Phys.* 12, 1305 (2000).
- [14] S. Denisov, *Physics Letters* 235, 447 (1997).
- [15] M. Bee, "Quasielastic Neutron Scattering", Adam Hilger, Bristol (1988).
- [16] Y. Zhang, L. Liu and Y. Wu, *Z. Phys. C*, **71**, 499501, 1996.
- [17] J. Klafter, A. Blumen, M.F. Shlesinger, *Phys. Rev. A* 35 (1987) 3081.

Chapter 4

A Compact Model For Electron-Phonon Calculations

4.1 Introduction

In the previous chapter we have acknowledged the flexibility of the discotic core and the influence of the tail motion on the motion of the core, which has been revealed by means of quasielastic neutron scattering. Therefore, it will be useful to obtain information about the influence of the fast vibrational dynamics of the tails, on that of the cores, since it might also contribute into overall relaxation dynamics. In the present chapter we are interested in model systems based on well-known symmetrical hexaether derivatives of triphenylene (figure 1.2, page2). The aromatic core is surrounded with six alkoxy tails that are required for columnar liquid crystal phase formation. The optimum side-chain length that gives the broadest mesophases range is found between five and seven carbons in the alkyl tail. Further increase or decrease of the tail length alters the temperature range of Col_h mesophases formation. For that reason 2,3,6,7,10,11-hexakis(hexyloxy)triphenylene (HAT6) is the most studied member from the whole homologous series. Slow whole-body motions of the disks on the pico- and nano-second timescale perturb the charge-transfer between neighboring molecules, and there have been a number of recent publications on this issue.[2-7] In the present study however, we are concerned with the faster vibrational motions of the triphenylene core that are responsible for the relaxation of the electronically excited-states created by absorbed photons. The study of these excited states is rather difficult for two reasons. Firstly, although density functional theory (DFT) calculations are routinely used to establish the vibrational modes of modestly sized molecule systems, such calculations in the electronically excited states are not straightforward. This difficulty can be at least partially overcome by using large aromatic systems in which the distortion of the nuclear structure in the electronically excited states tends to be spread over the whole molecule, leading to only slight changes in the vibrational eigenvectors. That is, the normal modes of vibration in the electronically excited will be rather similar to those in the ground state. Secondly, even in the electronic ground-state accurate electronic-structure calculations for discotic

⁰This chapter is based on paper: O. Kruglova, F. M. Mulder, A. Kotlewski, S. J. Picken, S. Parker, M. R. Johnson and G. J. Kearley, *Chem. Phys.* **330**, 360 (2006).

systems are somewhat time consuming, and in order to proceed, we need to establish the smallest model that accurately reproduces the vibrational dynamics of the aromatic cores. Even in the solid-state the tail conformation is uncertain and the longer timescale dynamics in the liquid-crystalline columnar Col_h phase are rather complex. These effects are difficult to model at the DFT level and again, it would be convenient to establish that whilst the tails are required for the structure, they can actually be ignored in the study of the core vibrations. Excluding the tails may not be as obvious as it first appears since we know that on the picosecond timescale the dynamics of the cores and tails are strongly coupled.[6,7] Further, interdigitation of the tails between disks on neighbouring columns could bring the terminal methyl group on molecule into close proximity of a core of a different molecule. In order to establish the minimum model we need to measure the vibrations of the cores in the presence of the tails, and establish the sensitivity of the core-vibrations to tail length. This can be conveniently achieved using INS, which reports mainly on H-atom motion, see for examples ref.8 and references therein. By deuteration of the alkoxy tails, we see only the vibrational dynamics of the H-atoms that are attached directly to the cores, and any spectral changes arising from alteration of the tail length reflect sensitivity to tail length and/or tail conformation. By comparing the measured INS spectra with those from DFT calculations we can establish the validity of the DFT method in these systems, and the relative importance of intermolecular interactions in the vibrational dynamics of the aromatic cores. It transpires that a single isolated disk with rather short tails has almost the same vibrational dynamics in the core as that measured for a discotic molecule with tails that are 6 C-atoms long in the bulk material. Nevertheless, there is some spectral sensitivity to the conformation of the alkoxy group itself, and this can be reproduced by DFT calculations on a single molecule.

4.2 Experimental techniques

4.2.1 Preparation

2,3,6,7,10,11 Hexakismethoxytriphenylene (HAT1) and deuterated analogue HAT1 (D) were made by oxidative trimerization of 1,2-dimethoxybenzene and 1,2 dimethoxybenzene(D6), respectively, using molybdenum(V) chloride⁷. 2,3,6,7,10,11 hexakisethoxytriphenylene (HAT6) and 2,3,6,7,10,11 hexakispropyloxytriphenylene (HAT3) and their deuterated analogues HAT6D, HAT3D were made by alkylation of 2,3,6,7,10,11 hexahydroxytriphenylene with appropriate alkylbromides in DMF in the presence of potassium carbonate.[9,10]

4.2.2 INS spectra

These were measured on the TOSCA spectrometer at the ISIS pulsed neutron source at the Rutherford Appleton Laboratory, Chilton, UK. This spectrometer has an energy resolution $\frac{\delta E}{E} < 2\%$. Samples were sealed in aluminium containers and cooled in a closed circuit refrigerator to 20K in order to sharpen the vibrational fundamental bands by reducing the effects of the Debye-Waller factor. The occurrence of phase transitions on cooling to this temperature has not been established, but is not of concern to the current study. Data were corrected for detector efficiency and other instrumental effects using the standard algorithms provided by ISIS.

4.2.3 Computational methods

Initial molecular structures were optimised using the ab-initio COMPASS force field and then further refined using the density function theory (DFT) code DMol3[11] which uses localised numerical atomic-orbitals. The dnp atomic basis set was used that includes polarization functions, with the generalised gradient corrected (GGA) functional by Perdew and Wang (P91). A fine grid was used in the numerical integration and a global real-space cutoff of 3.7\AA . The convergence criterion in structure optimisations was 10^{-5} H. The vibrational spectra for the minimised structure were calculated in the harmonic approximation by using the direct method to obtain the forces from *ab-initio* calculations using atomic displacements of 0.03\AA in positive and negative directions along the three Cartesian directions. CLIMAX[12] was then used to calculate the neutron spectral profile including multi-phonon contributions at frequencies given by the sum of the one-phonon components.

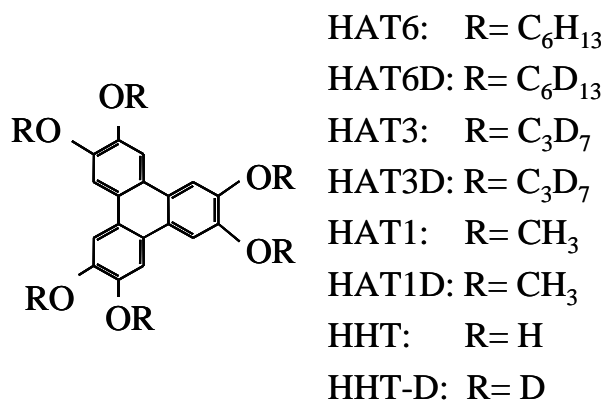


Figure 4.1: Structures of investigated triphenylene derivatives.

4.3 Results and Discussion

4.3.1 Observed INS spectra, sensitivity of core-modes to tail-length

Discotic systems are only of technological interest in their columnar phases, which are normally stable over a fairly narrow temperature range around room temperature. At lower temperatures the order increases and the molecules tend to adopt a herringbone arrangement with stronger intermolecular interactions. Our INS spectra were recorded at 20K in order to avoid the broadening effect of the Debye-Waller factor, and consequently, our spectra will reflect the stronger intermolecular interactions of the more crystalline phase, rather than those of the columnar phase. Since we will show that an isolated molecule approach is satisfactory even in the presence of these stronger interactions, it is clear that the details of the crystal structure are not relevant to the present study.

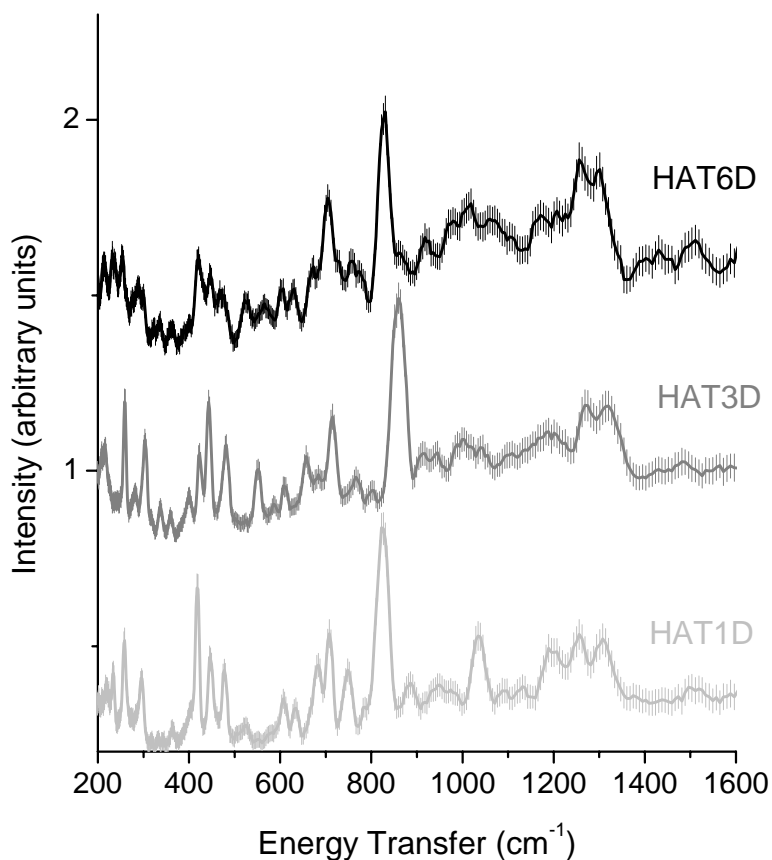


Figure 4.2: Observed INS spectra of HAT6D, HAT3D and HAT1D.

INS spectroscopy was chosen for 2 reasons. Firstly because it is fairly straightforward to calculate the intensities, and secondly because the incoherent scattering of the D-nucleus (and almost all other

nuclei) is many times lower than that of the H-nucleus. Measured INS spectra of three triphenylene derivatives HAT1D, HAT3D and HAT6D, are illustrated in figure 4.1, the integers referring to the number of carbon atoms in the alkoxy tails, and the "D" being used to denote that the H-atoms of the tails were deuterated. It is immediately apparent that the spectra of the homologues are remarkably similar. These spectra arise from the 6 H-atoms that are directly connected to the aromatic rings, and we can see that to a very good approximation the vibrational dynamics of the triphenylene cores are independent of the aliphatic tails.

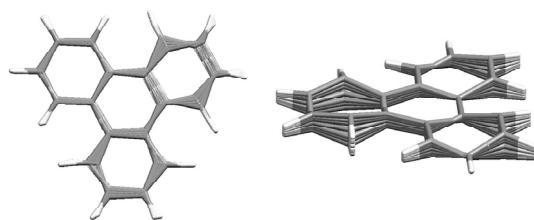


Figure 4.3: Examples of in-plane (left) and out-of-plane (right) vibrational displacements of the triphenylene core. These motions are highlighted in the experiment by deuteration of the alkoxytails (not shown, see figure 4.1).

Examples of the vibrational displacements of the cores are illustrated in figure 4.3, where the participation of the H-atoms connected to the cores can be seen. The most significant difference is upward shift of the strong peak at around 850 cm^{-1} in HAT3D compared with HAT1D and HAT6D, which we will discuss later. Other small differences at higher energies almost certainly arise from the tails. At these high energy and momentum transfers the total neutron scattering cross section

can be treated as incoherent, the so-called incoherent approximation. The total scattering cross section of the tails: OCD_3 , $\text{O}(\text{CD}_2)_2\text{CD}_3$ and $\text{O}(\text{CD}_2)_5\text{CD}_3$ are 32.2, 73.2 and 134.7 barns per tail, respectively, which has to be compared 81.7 barns per H-atom on the triphenylene core. Clearly, the contribution of the tails to the INS spectrum is drastically reduced by deuteration, but even for perfect deuteration, some small differences will be visible due the difference in composition of the tails. The similarity of the INS spectra of HAT6D and HAT1D would also tend to suggest that intermolecular interactions have little effect on the core vibrations, since even though the low-temperature crystal structures of these are unknown, they are unlikely to be identical.

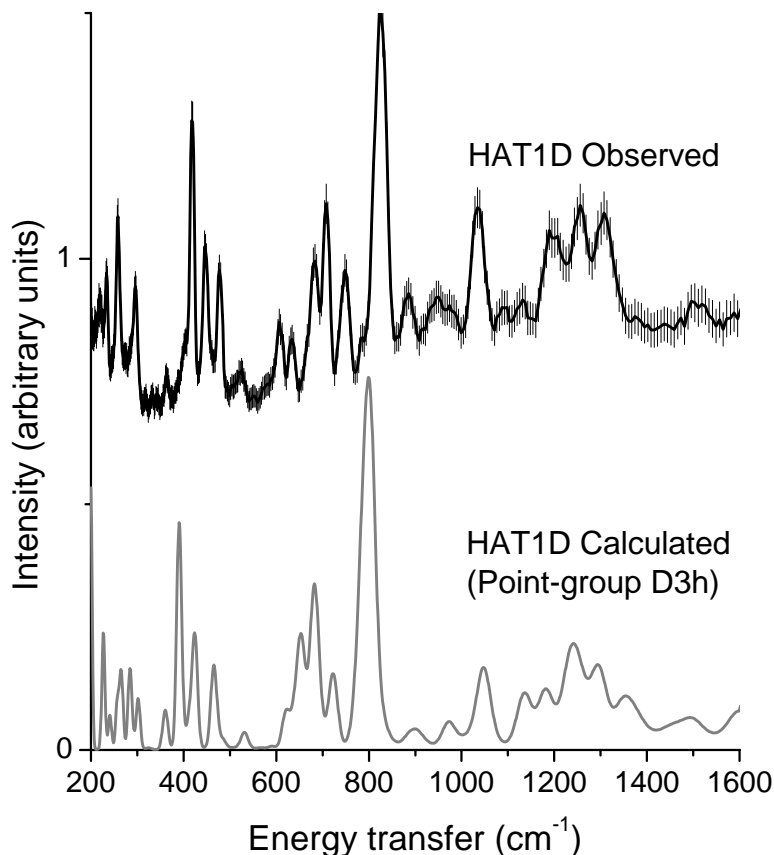


Figure 4.4: A comparison of observed and calculated INS spectra of HAT1D. The molecule was constrained to a planar conformation with D_{3h} point-group symmetry in the calculation.

4.3.2 Calculated Spectra

INS spectra are also very suitable for comparison with calculations because the spectral intensity is fairly simply related to the displacement-amplitude of the H-atom nuclei. By comparing observed

INS spectra with those calculated for isolated molecules we should be able to confirm the negligible effect of intermolecular interaction on the core-vibrations, and establish the effect of the conformation of the alkoxy group. Clearly, this will also confirm that a particular quantum-chemistry algorithm provides a good molecular structure and vibrational displacements for electronic-structure calculations of the triphenylene system.

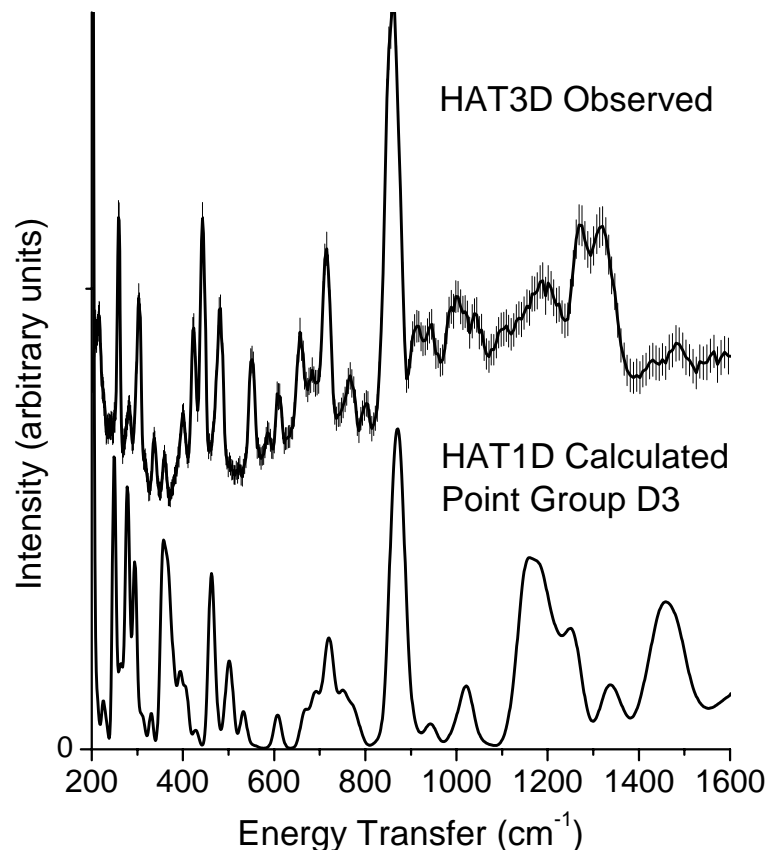


Figure 4.5: Observed INS spectrum of HAT3D compared with the calculated spectrum of HAT1D in the out-of-plane conformation constrained to D3 point-group symmetry.

4.3.3 HAT1 core vibrations

We will begin with HAT1 and HAT1D because the spectrum of HAT3D is slightly different, and as we will show, seems to reflect a sensitivity to tail conformation. For HAT1D we tested a number of conformations of the methoxy tails and found that the conformation with D_{3h} point-group symmetry was the lowest energy minimum found, and also gave best agreement with the measured INS spectrum. Observed and calculated spectra of HAT1D are compared in figure 4.4. Considering

the complexity of the system, the overall agreement is rather satisfactory. Because the methyl group has been deuterated the INS signal comes from mainly from the 6 H-atoms that are connected to the triphenylene core, so that this agreement strongly suggests that the harder modes of the core, above about 300 cm^{-1} , are not influenced by the molecular environment. Nevertheless, we would expect the torsional coordinates of the methoxy tails to be sensitive to intermolecular effects, and this may explain the limited agreement below 300 cm^{-1} . This comparison shows clearly that the isolated molecule approximation is perfectly adequate for studies in which we are primarily concerned only with internal vibrations of the aromatic core.

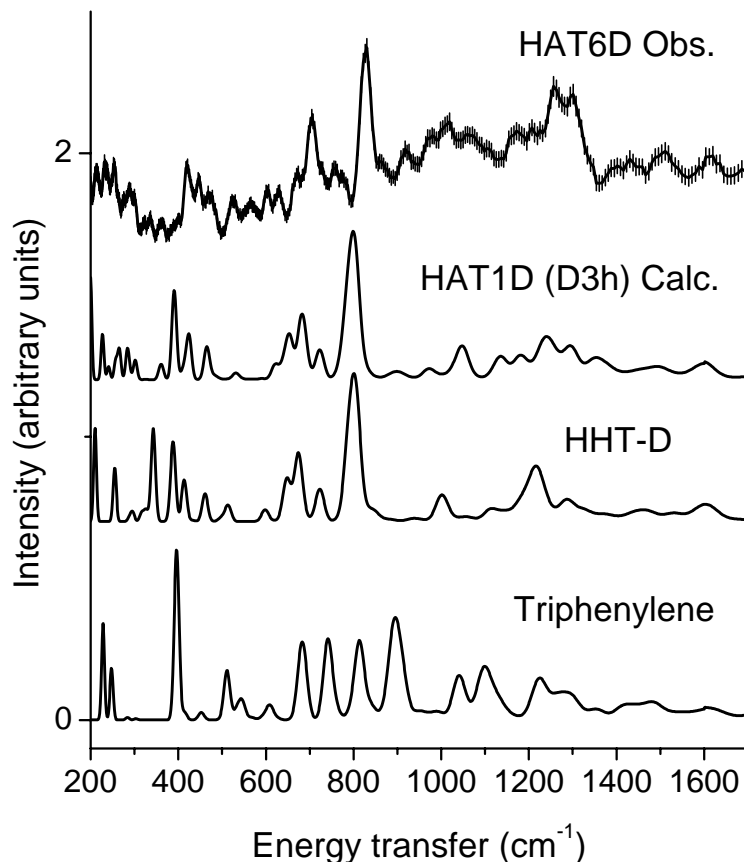


Figure 4.6: Observed INS spectrum of HAT6D compared with calculated spectra of various simplified models. Triphenylene is clearly unsatisfactory, but there is little to choose between the other two models.

4.3.4 Conformation of the methoxy tail

It is likely that there is frozen disorder in the longer tails, and conformations of these are of no interest to the present work. Nevertheless, even when the alkoxy tails are deuterated (figure 4.2)

it is clear that the intense feature due to the out-of-plane (ring puckering motion) at around 850 cm^{-1} is at noticeably higher energy in HAT3D than in the other homologues, HAT1D and HAT6D. The frequency of these modes is rather sensitive to the conformation of the O-CH₃ with respect to the triphenylene cores. We cannot provide definitive structural information on the basis of one peak, but we can determine which limiting conformations give best agreement with the observed spectrum. It was found that whilst the in-plane conformation of the O-CD₃ group (D_{3h} point-group symmetry for the whole molecule) gives the best agreement with the ring-puckering modes of HAT1D and HAT6D, and alternate up/down conformation of these groups (D_3 for the molecule) provides better agreement for HAT3D as illustrated in figure 4. The total energy for HAT1D in the D_{3h} conformation is 0.3eV less than the D_3 model, the latter being a local minimum. This energy is probably compensated in HAT3 by intermolecular interactions of the tails that may reflect some odd-even behaviour for tails longer than 1, which is a well known effect for both calamitic and discotic liquid crystals.

4.3.5 Other models and electronic effects

Given the sensitivity to methoxy conformation above, it is interesting to enquire whether an even smaller model could be used. The limiting case is triphenylene, and the calculated spectrum of this molecule, with alternate H-atoms being replaced by deuterium, is illustrated in figure 5. A comparison with the spectrum of HAT1D reveals that this model is rather extreme and gives only approximate agreement with HAT1D. In contrast, HHT-D which is a derivative which instead of methyl has six phenol groups with deuterium atoms around aromatic core leads to a calculated spectrum that is in remarkably good agreement with the experimental spectrum of HAT6D (figure 5). Since these materials are of interest for organic solar cells, it is also important that the electronic structure of the model remains similar to that of triphenylene with alkoxy tails. The important splittings, between the HOMO and the LUMO, and between the HOMO and the HOMO-1 levels, are collected for the various models in table 1. It is clear from this table that the electronic structure of HHT-D (in the planar D_{3h} conformation) around the "gap" is very similar to that of HAT1D in the same conformation, and that this overall is the best model. Perhaps surprisingly, the electronic structure of HAT1D in the D_3 conformation and triphenylene are rather similar to each other, but different from the D_{3h} HAT1D and HHT-D structures, within the limitations of the energy-levels used here.

	HAT1 (D_3)	HAT1 (D_{3h})	HHT-D	Triphenylene
HOMO-(HOMO-1) eV	0.495	0.826	0.814	0.415
HOMO-LUMO, eV	3.344	3.197	3.127	3.589

4.4 Conclusions

Whilst the alkoxy tails play a vital role in the phase diagram of triphenylenes and the whole-body dynamics of the disks, they have only a slight effect on the vibrational dynamics of the triphenylene cores. Nevertheless, there is a difference between the kinetic coupling of the out-of-plane dynamics of the core with in-plane or out-of-plane conformation of the alkoxy stem, and it is important that this is correct in the model. The experimental data shows that the vibrational dynamics of the tails, beyond the first C-atom, is independent of the cores and that a short-tail model should correctly reproduce the essential characteristic of the core vibrations. Although a completely tail-less model, triphenylene, does not reproduce the core vibrations of the HAT molecules correctly, replacement of

the alkoxy group by OH reproduces not only the correct vibrational dynamics, but also the correct electronic energy-level spacing. Both the electronic structure, and the vibrations of the triphenylene core are sensitive to the conformation of the alkoxy (methoxy) conformation with respect to the molecular plane, which could provide a means of improving the performance of these materials in solar-cell applications.

Bibliography

- [1] L. Schmidt-Mende, A. Fechtenkötter, K. Müllen, E. Moons, R.H. Friend, J.D. MacKenzie, *Science* 293 (2001) 1119 and comments: J. Nelson, *Science* 293 (2001) 1059.
- [2] J. Cornil, V. Lemaire, J-P. Calbert, J-L. Brédas, *Adv. Mater.* 14 (2002) 726.
- [3] K. Senthilkumar, F.C. Grozema, F.M. Bickelhaupt, L.D.A. Siebbeles, *J. Am. Chem. Soc.* 119 (2003) 9809.
- [4] B.R. Wegewijs, L.D.A. Siebbeles, N. Boden, R.J. Bushby, B. Movaghar, O.R. Lozman, Q. Liu, A. Pecchia, L.A. Mason, *Phys. Rev. B.* 65 (2002) 245112.
- [5] V. Lemaire, D.A. da Silva Filho, V. Coropceanu, M. Lehmann, Y. Geerts, J. Piris, M.G. Debije, A.M. van de Craats, K. Senthilkumar, L.D.A. Siebbeles, J.M. Warman, J-L. Brédas, J. Cornil, *J. Am. Chem. Soc.* 126 (2004) 3271.
- [6] F.M. Mulder, J. Stride, J., S.J. Picken, P.H.J. Kouwer, M.P. de Haas, L.D.A. Siebbeles, G.J. Kearley, *J. Am. Chem. Soc.* 125 (2003) 3860.
- [7] G.J. Kearley, F.M. Mulder, S.J. Picken, P.H.J. Kouwer, J. Stride, *Chem. Phys.* 292 (2003) 185.
- [8] G.J. Kearley, M.R. Johnson, J. Tomkinson, *J. Chem. Phys.* 124 (2006) 44514.
- [9] R. Zniber, R. Achour, M. Zoubar Cherkaoui, B. Donnio, L. Gehringer, D. Guillon, *J. Mater. Chem.* 12 (2002) 2208.
- [10] A. Schultz, S. Laschat, M. Morr, S. Diele, M. Dreyer, G. Bringmann, *Helvetica Chimica Acta*, 85 (2002) 3909.
- [11] B. Delley, *J. Chem. Phys.* 92(1) (1990) 508.
- [12] G.J. Kearley, *Nuclear Instrum. Meth.* A354 (1995) 53.

Chapter 5

Coupling Between Local Vibrations and Charge Transport

5.1 Introduction

Low charge-mobility and rapid quenching of excited states severely limits the application of many organic molecules for electronics applications. Static defects certainly reduce charge transfer and limit delocalisation, but in self-healing materials such as the columnar discotic liquid-crystalline materials that we are concerned with here, the effect of thermal motion on the electronic structure is probably more important. In the most simple picture, thermal motion of the disks alters the overlap of the π -systems, which reduces the conducting properties. Consequently, a number of studies[2-5] have correlated translation and rotation of aromatic disks with the charge transfer between disks by using finite displacements of two rigid-body aromatic cores. The electronic structure of the core-dimer was calculated at each incremental step to map out the charge transfer integral along the chosen coordinate. In the present paper we use a molecular-dynamics (MD) simulation to provide molecular conformations that are distorted by thermal motion. This approach has the advantage that a correct distribution of realistic distortions is produced, within the constraints of the ab-initio based force field that was used. It has the disadvantage however, that the molecular units are distorted from their time-averaged symmetry and there is no straightforward way in which quantitative correlations between the energy-levels of the molecular units can be made. Discotic systems are normally regarded as electron-hole conductors, and consequently charge transport will be related to the HOMO energy level. It follows that we can obtain a qualitative measure of charge transport in the thermally distorted system by following the temporal changes in the HOMO level during the MD simulation. It has recently been shown that vibrational distortions play an important role in determining the electronic properties of conducting polymers[6-10], which suggests that small molecular distortions in other organic conductors may also be important. Secondly, which are the most important inter or intra molecular distortions when we also take account of the maximum amplitude that is accessible at around room temperature? For this we must include the interactions

⁰This chapter is based on paper: O. Kruglova, F. M. Mulder, L. D. A. Siebbeles and G. J. Kearley, *Chem. Phys.*, **330**, 333 (2006)

and dynamics of the tails, otherwise all intermolecular interactions will be too soft. Our approach is to extract the atomic coordinates of a central discotic-dimer from time-steps of a molecular dynamics (MD) simulation, using the same molecular model that has previously been published for this system [11]. This model is important because it has previously been validated for the ps timescale against experimental quasielastic neutron scattering data, and whilst the details of the force field do not reproduce the vibrational spectrum of HAT6 particularly well, the errors in frequencies do not seriously affect our main conclusions.

5.2 Method and Theory

The MD simulation was carried out using the COMPASS force field [12] following thermalisation and equilibration runs with a total duration of 600 ps at a simulation temperature of 300K. The analysis

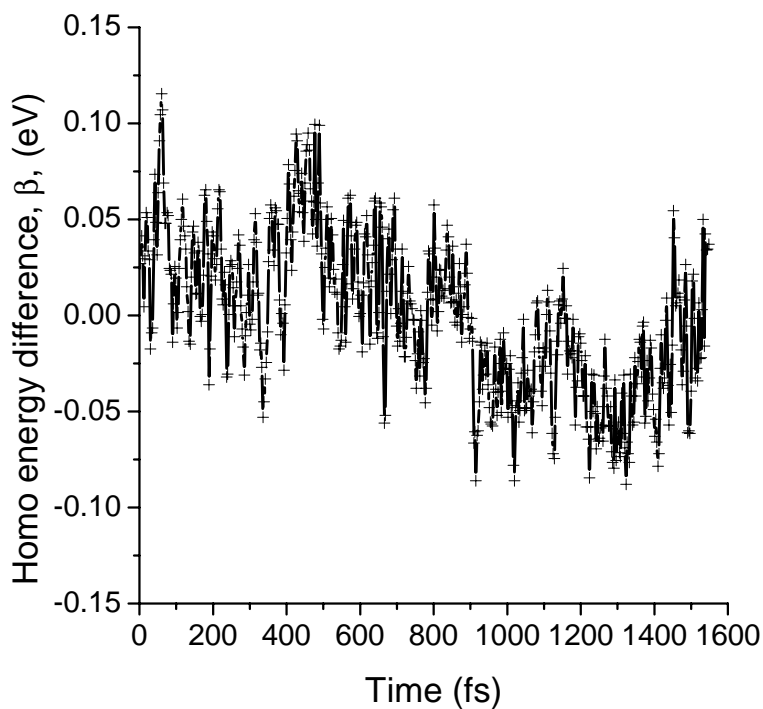


Figure 5.1: Variation of the interaction energy of the HOMOs, β , in the distorted monomers in the formation of the dimer. See equation 5.1. The average interaction energy (0.25499 eV) has been subtracted to enable direct comparison with figure 5.3.

was made from the following 1536 frames with a time-step of 1 fs, every third frame being used to provide 512 frames with a 3 fs step for the final analysis. This choice is consistent with the desired spectral characteristics (energy-range of around 5000 cm^{-1} with a resolution around 20 cm^{-1}),

reasonable statistical sampling, good level of DFT calculation and available computing resources. Although the MD simulation was made with a stack of 4 molecules of HAT6, including the alkoxy tails, for the DFT calculations the frames were reduced by selecting the central 2 molecules and then replacing the alkoxy tails of these with H-atoms. This produced a dimer-model for the thermally distorted triphenylene cores containing 60 atoms. DFT calculations on the resulting dimers were made using DMol3 [13]. This code allows an all electron calculation to be performed without the uncertainties associated with the pseudopotential construction. Localised basis sets were used,

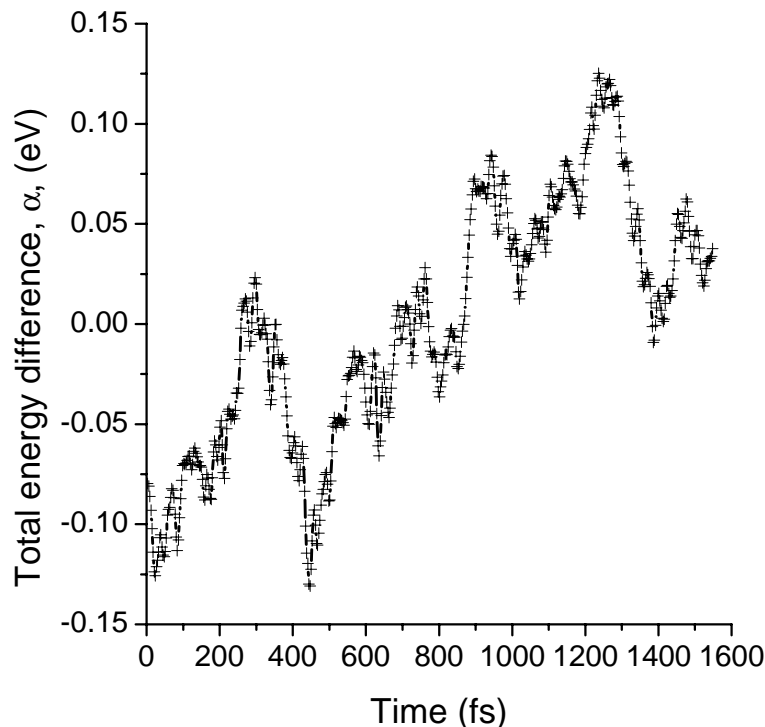


Figure 5.2: Variation of the interaction energy of the total energy, α , in the distorted monomers in the formation of the dimer. See equation 5.2. The average interaction energy (-0.6958 eV) has been subtracted to allow direct comparison with figure 5.1.

represented as a numerical tabulation: a DND double numerical basis set with polarisation functions for carbon was used. A large number of energy calculations are necessary, and because we are not attempting a quantitative analysis we restricted ourselves to the Local Density Approximation LDA (Perdew-Wang). The orbital energy of the HOMO in the dimer (E_{hd}) at any time step can be related to the corresponding HOMO energies in the distorted monomers (E_{ha} and E_{hb}) by defining a term, β that arises from the orbital interaction between the two molecules:

$$\beta = E_{hd} - \frac{1}{2}(E_{ha} + E_{hb}) \quad (5.1)$$

where E_{ha} and E_{hb} are orbital energies of the HOMOs calculated for the isolated monomers, a and b. The total interaction energy between the two molecules, α , will depend mainly on the molecular separation and orientation and can easily be obtained for each time-step from the total energy of the distorted dimers E_{td} , and the total energies of the distorted monomers, E_{ta} and E_{tb} :

$$\alpha = E_{td} - (E_{ta} + E_{tb}) \quad (5.2)$$

A comparison of α and β reveals the effect of the intermolecular interaction energy on the HOMO-HOMO interaction.

5.3 Results and Discussion

The temporal variation of the orbital interaction term, β , and the total interaction, α , are illustrated in figures 5.1 and 5.2, respectively, the average values of β and α having been subtracted for the purpose of comparison. Variations on a number of timescales are clear, but perhaps the most

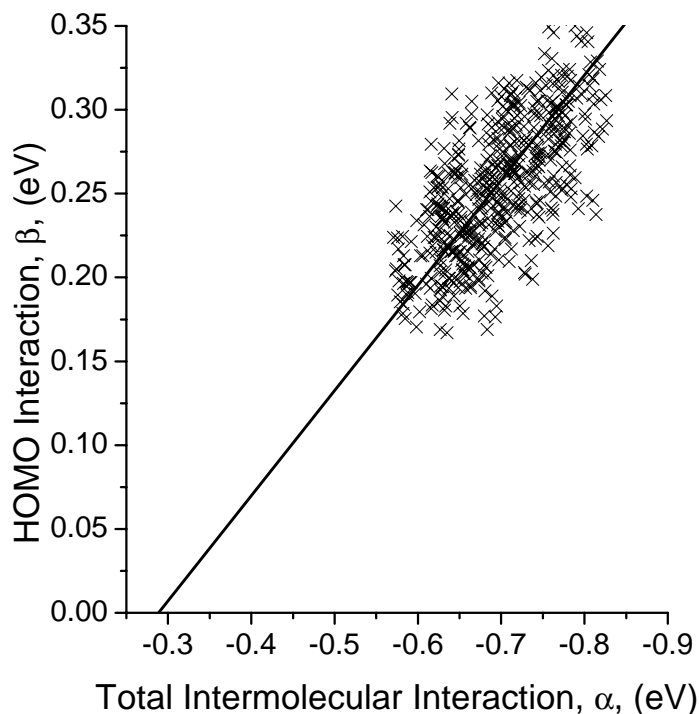


Figure 5.3: Correlation between the data in figures 5.1 and 5.2. The line is a fit to the data illustrating that when the binding energy is less than ~ -0.4 eV the interaction between the HOMOs will be very slight.

important are those in figure 5.1 with an amplitude of around 0.1 eV over the period of a few

fs, which are almost absent in figure 5.2. These reflect variations of the HOMO interactions on the vibrational timescale, whilst the slower variations that are present in both figures are due to inter-molecular motions. Comparison of the results in figures 5.1 and 5.2 reveals some correlation of the slower variations, this being illustrated in figure 5.3. From this figure it can be seen that the magnitude of the orbital interaction, β , decreases (less positive) as the total (intermolecular interaction), α , decreases (less negative), and although we would not anticipate a linear dependence (the intercept should be at zero) a straight-line fit clearly shows that β will be very small when the total intermolecular interaction is below about 0.3 eV. The scatter about the fitted line is caused by the short-timescale molecular vibrations that are superimposed on the longer timescale whole-body motions, these being evident in the differences between figures 5.1 and 5.2, respectively. We will now examine the frequency distribution of these fluctuations.

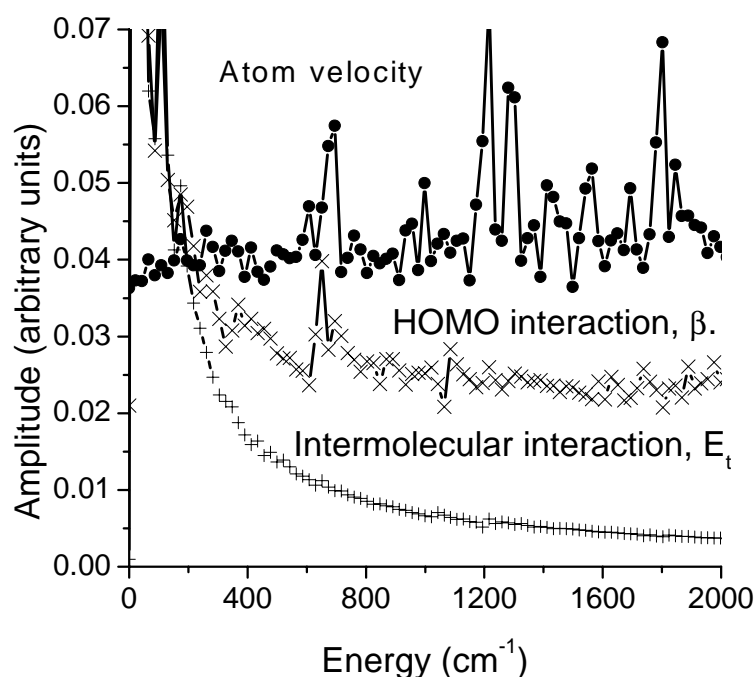


Figure 5.4: A comparison of the frequency spectra from figure 5.2 (intermolecular interaction, total energy), figure 5.1 (interaction of the HOMOs of the monomers in forming the dimer), and the frequency spectrum of the motion of the dimer-model atoms. The upper plot has been displaced by 0.02 for ease of presentation .

In order to obtain the frequencies of the fluctuations, the auto-correlation functions were calculated for α and β and for the velocities of all atoms. These were then Fourier transformed to the frequency domain. The results are compared in figure 5.4 where it can be seen that the total

interaction, α has a smooth spectrum with a profile that would be expected from a Boltzmann distribution at the simulation temperature (300K). The frequency spectrum for atomic motion shows peaks in the expected regions for molecular vibrations, although the peaks at about 1900 cm^{-1} are rather higher than expected and probably reflect the limitations of the COMPASS force-field for C-C stretching coordinates in triphenylene systems. The spectrum for the orbital interaction, β , has much less of an increase at low energies than that of α , and shows at least one distinct feature at around 700 cm^{-1} that approximately coincides with the atomic frequency spectrum. Molecular modes in this region arise from in-plane ring-deformation and puckering modes of the triphenylene core, and these seem to have an important effect on the HOMO-HOMO interaction of the dimer. The increase at frequencies below 200 cm^{-1} is due to the whole-body motions of the disks that have already been shown to be important in charge transport.

Although one would expect to have Boltzmann distribution for the total interaction α and orbital interaction β the shapes of curves seem to be different from exponential law trend. As we established in Chapter 3, the dependence of the relaxation time from momentum transfer (or the distribution of the jump length), $\tau(Q)$, is Lévy distribution. Since we consider HOMO and total interactions distorted by thermal motion, which we have measured by QENS, it would be logical to expect the change in shape for distribution of interaction energies as well. Fitting of both curves reveals the Lévy distribution behavior, figure 5.5. Lévy index for HOMO interaction is 0.07, which is quite close to the Lévy index obtained from relaxation dynamics for $Q > 0.53\text{ \AA}^{-1}$, 0.11, and for total interaction is 0.25. The discrepancy may have arisen from the model that have been used for calculations. The long range correlations that may be present in HAT6 were not properly taken into account in 4 disc model. Therefore, it would be interesting to analyze data obtained from simulation with periodic boundary conditions.

Figure 5.6 shows the frequency spectra of variations in the HOMO level of the dimer and of the monomer, compared with the atomic frequency spectrum. Although the statistics of the data are limited, it is clear that the spectra in this figure are rather similar, with the exception of the peaks due to C-H stretching at around 3300 cm^{-1} , and show that the energy-levels themselves are sensitive to virtually all molecular vibrations. However, since this effect is almost equally present in the monomers and the dimer, there is little net-effect on the orbital interaction, β , except for the peak at around 700 cm^{-1} discussed above.

Because of the loss of symmetry in the thermally distorted system it is rather difficult to make an orbital-by-orbital analysis of charge transport, and hence we restrict ourselves to qualitative arguments using equation 5.1. This difficulty arises because there is no general way in which the energy-levels in the distorted monomers can be related to those in the dimer. It is therefore interesting to enquire how the HOMO and HOMO-1 levels in the dimers change with increasing intermolecular interaction, α . As with the HOMO interaction, β , (figure 5.1), the HOMO and HOMO-1 levels have an approximately linear dependence, with scatter caused by the high-frequency motions (figure 5.7). Both the HOMO and the HOMO-1 go to higher (less negative) energies as the interaction increases, and the overlap of the scatter of the HOMO and the HOMO-1 is a manifestation of the problem alluded to above. Nevertheless, straight-line fits to the two sets reveal that the average HOMO and HOMO-1 would merge at an intermolecular interaction energy of about 0.2 eV, this being in reasonable agreement with the x-axis intercept in figure 5.7. The HOMOs of the distorted monomers are also illustrated on the left-hand side of the plot (all corresponding to zero on the x-axis) and it can be seen that these agree reasonably well with the straight-line fits.

The picture that emerges is of a system with 2 timescales. A slow timescale in which the orientation and position of the molecules relative to each other modulates the binding interaction

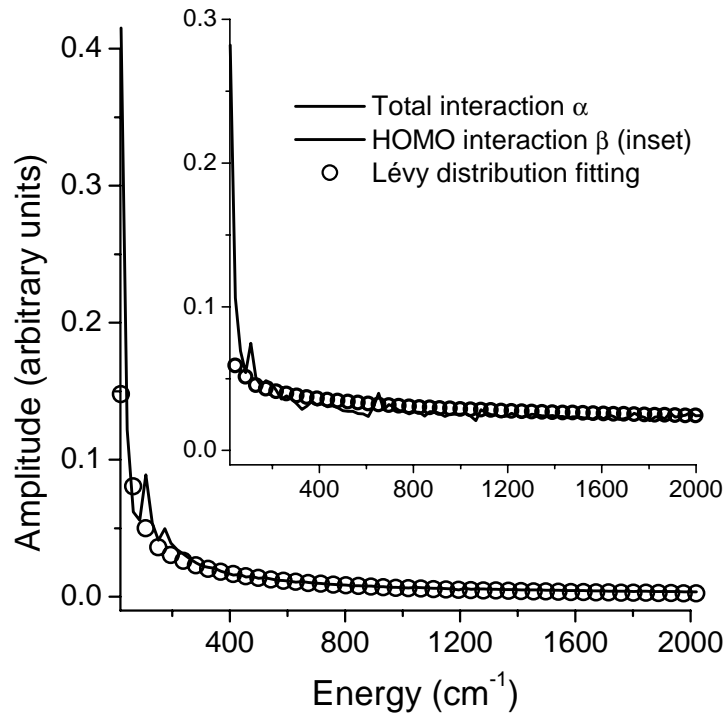


Figure 5.5: Fitting of the intermolecular interaction frequency spectra, α , and HOMO interaction frequency spectra, β , (inset) with Lévy distribution, eq. 3.1.

between the molecules. On the faster timescale it seems that almost all molecular vibrations alter the energies of the HOMOs, but these have no net effect on the interaction between the HOMOs except at lower frequencies and in particular ring deformation modes.

5.4 Conclusions

Despite the difficulties caused by the loss of symmetry in the molecular units and their dimer, it has still been possible to show that we can analyse the mixing of the monomer HOMOs in the formation of the dimer HOMOs. This can be achieved by separating the timescales of the interactions. The molecular vibrations have little effect upon the binding energy between the two molecules but they do have a relatively "instantaneous" effect on the HOMOs of the monomers and the dimer. These rapid changes in the difference between the dimer HOMO energy and the average of the HOMO energies of its constituent monomers gives an indication of the effects of the molecular degrees of freedom on charge transport, this being important for applications.

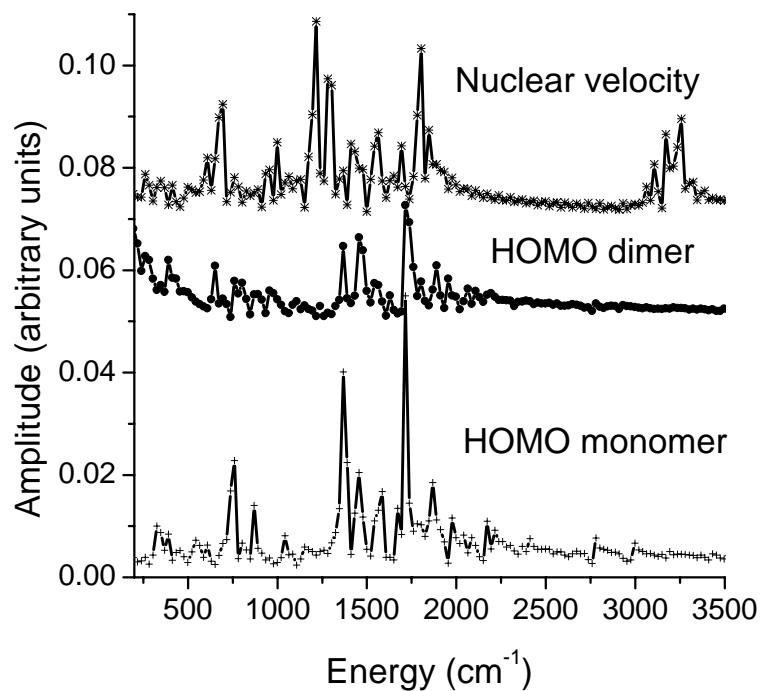


Figure 5.6: Frequency spectra of the HOMOs of the dimer and the monomer compared with the frequency spectrum of the motion of the dimer-model atoms.

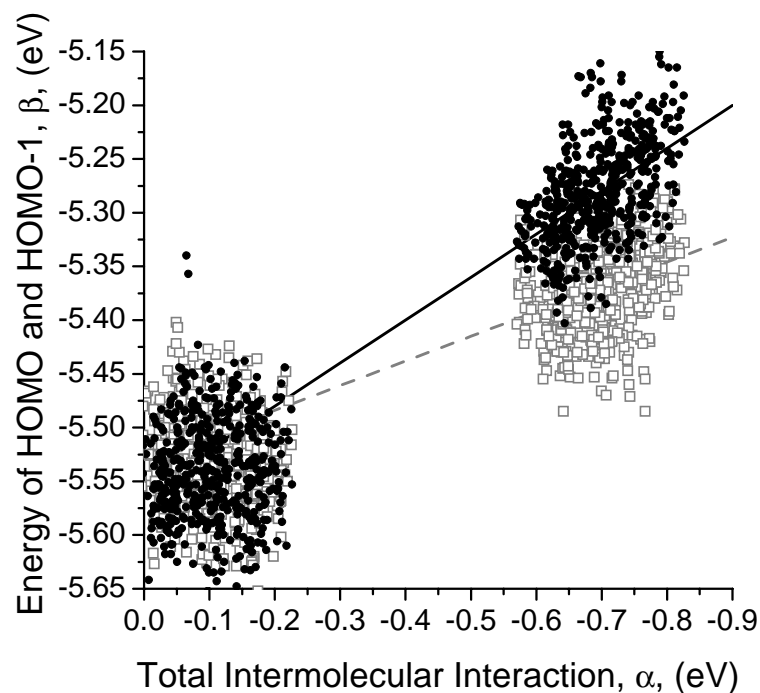


Figure 5.7: Correlation of the HOMO (filled circles) and HOMO-1 (open squares) energies of the distorted dimers with the total interaction energy of dimer formation from the distorted monomers. The lines are fits to the two sets. The points on the left of the plot are the HOMOs of the distorted monomers and all correspond to a total interaction of zero. They are displaced along the x-direction only for clarity, otherwise they all superimpose at $\alpha = 0$.

Bibliography

- [1] J. Cornil, V. Lemaur, J-P Calbert , J-L Brdas, Adv. Mater., 2002, **14**, 726.
- [2] K. Senthilkumar, F. C. Grozema, F. M. Bickelhaupt, L. D. A. Siebbeles, J. Am. Chem. Soc., 2003, **119**, 9809.
- [3] B. R. Wegewijs, L. D. A. Siebbeles, N. Boden, R. J. Bushby, B. Movaghar, O. R. Lozman, Q. Liu, A. Pecchia, L. A. Mason, Phys. Rev. B., 2002, **65**, 245112.
- [4] V. Lemaur, D. A. da Silva Filho, V. Coropceanu, M. Lehmann, Y. Geerts, J. Piris, M. G. Debije, A. M. van de Craats, K. Senthilkumar, L. D. A. Siebbeles, J. M. Warman, J-L Brdas, J. Cornil, J. Am. Chem. Soc., 2004, **126**, 3271.
- [5] S. Tretiak, A. Saxena, R. L. Martin and A. R. Bishop, Phys. Rev. Lett. 2002, **89**, 097402.
- [6] S. Tretiak, A. Saxena, R. L. Martin and A. R. Bishop, Phase Transitions 2002, **75**, 725.
- [7] I. Franco and S. Tretiak, J. Am. Chem. Soc., 2004, **126**, 12130.
- [8] N. Ishii, E. Tokunaga, S. Adachi, T. Kimura, H. Matsuda, T. Kobayashi, Phys. Rev. A, 2004, **70**, 23811.
- [9] L. van Eijck, K. Senthilkumar, L. D. A. Siebbeles, G. J. Kearley, Physica B 2004, E220, **350**.
- [10] F. M. Mulder, J. Stride, S. J. Picken, P. H. J. Kouwer, M. P. de Haas, L. D. A. Siebbeles, G. J. Kearley, G.J., J. Am. Chem. Soc. 2003, **125**, 3860.
- [11] H. Sun, H. J. Phys. Chem. 1998, **102**, 7338.
- [12] B. Delley, J. Chem. Phys. 2000, **113**, 7756.

Chapter 6

Structure of charge transfer complex

6.1 Introduction

The ability of some discotic liquid crystals to form columns has made them attractive candidates for conductive devices¹. The π - π orbital overlap of the aromatic-core carbon atoms forms a 1D path for charge carriers to travel along column direction. The important quantity, which characterizes efficiency of such charge transfer, is mobility. The charge carrier mobility is connected to dynamics and, therefore, to the structure of the system under consideration via the diffusion coefficient. At present, hexabenzocoronene, possess the highest charge carrier mobility amongst the liquid crystalline materials [1,2]. Introduction of dopants (donor or acceptor) might improve the situation and make transfer even more efficient since it facilitates charge-separation and prevents recombination. TNF is one of the such an electron acceptor molecules. For about the last decade it has been assumed that within the columnar phases, the TNF acceptor molecules lie between the discotic molecules within the same column [3-7]. Perhaps surprisingly there has been no detailed examination of the structural aspects of these mixed charge transfer complexes. The purpose of this paper is to bring together neutron scattering, x-ray diffraction and density functional theory (DFT) calculations to elucidate the juxtaposition of the charge transfer and discotic molecules in the complex materials. We will show that introduction of dopant leads to formation of a system with three-fold symmetry, each acceptor lying at the corner of equilateral triangle with the donor situated at the centre of this triangle. We have used the model system, hexakis(n-hexyloxy)triphenylene (HAT6), which acts as the donor, and 2,4,7trinitro-9-fluorenone (TNF) as the acceptor, fig.6.1. We denote this complex HAT6-TNF. It is fortunate that these materials can be aligned by shear flow, and we use this to achieve a preferential orientation that simplifies our analysis. Pure HAT6 forms a hexagonal columnar phase between 67 and 99° C. The addition of TNF increases the stability-range of the columnar phase to below room temperature to 237° C, indicating a fairly strong interaction between the two species.

¹This chapter is based on paper: O. Kruglova, E. Mendes, Z. Yildirim, M. Wübbenhorst F. M. Mulder, J. Stride, S. J. Picken and G. J. Kearley, *ChemPhysChem*, **2006**, submitted

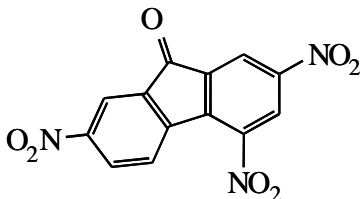


Figure 6.1: 2,4,7trinitro-9-fluorenone (TNF).

6.2 Experimental

6.2.1 Preparation

HAT6 with isotropically normal [10] and with deuterated side chains and TNF were mixed at 1:1 molar proportion in dichloromethane, and then evaporated to dryness at room temperature. To remove any traces of solvent, and to ensure the correct phase-behaviour, the resulting HAT6-TNF was heated to the isotropization temperature, $T=237^{\circ}\text{C}$, then cooled slowly.

6.2.2 Alignment

For the neutron scattering experiments sample alignment was achieved by placing the sample in a shallow (0.5mm) circular recess of an aluminum plate that formed one half of the sample container. An aluminum disk that was 1.5mm smaller than the recess was placed over the sample and then displaced, under slight pressure, to provide mechanical shear on the sample. In practice it was found easier to perform the alignment operation within the temperature-control device of the spectrometer. This was used to first melt the sample in the recess and then cool to just below the isotropization/clearing point before applying the shear. The container was then sealed with the

¹Alkoxy side chain deuteration was achieved via reaction of 2,3,6,7,10,11-hexa-hydroxy triphenylene with pre-deuterated n-hexyl bromide (Aldrich) under basic conditions (K_2CO_3) in 2-butanone under reflux conditions for 24 hours in a nitrogen atmosphere.

disk in place, and the sample environment closed. For the XRD measurements the HAT6-TNF was heated to the isotropization temperature, cooled and aligned by shear flow on kapton foil at $T=373\text{K}$ and then cooled slowly to room temperature.

6.2.3 Neutron scattering

QENS spectra for HAT6 and HAT6-TNF were obtained using the IN6 spectrometer at Institute Laue Langevin in France with an incident wavelength of 5.9\AA^{-1} and standard sample temperature-control. Background spectra and spectra from a 1 mm vanadium plate were used to correct the data using standard data-treatment algorithms. The neutron diffraction is obtained by taking the intensity of the elastic peak as a function of scattering angle.

6.2.4 X-ray diffraction

The molecular arrangements in different samples were analysed with a Bruker Nonius D8-Discover X-ray diffractometer equipped with a home-built capillary oven. HAT6 sample was placed into an X-ray capillary with 0.7 mm internal diameter and then the capillary tube was placed inside a vertically aligned graphite tube with a transversal hole, which allows the incident X-ray beam to cross freely. The temperature of the graphite tube was controlled by a system formed by a thermo-couple connected to a PID controller and power supply, which acts as a fast-response online oven ranging from room temperature to 350 C. XRD measurements for HAT6-TNF were made at room temperature. The X-ray measurements were carried out with a sample to detector distance set to 6 cm and spectra were recorded for 30 min.

6.2.5 Optical polarization microscope (OPM)

The optical textures of the present phases and the related transition temperatures were analyzed by a Nikon Eclipse E600 optical polarizing microscope that was equipped with a Mettler FP 82HT hot stage controlled by a Mettler FP 80 central processor. The heating/cooling rate was 5C/min. The alignment property of HAT6-TNF complex was investigated on two different substrates, glass and Al-foil. Both pristine and sand-paper rubbed surfaces were checked.

6.2.6 Dielectric relaxation spectroscopy (DRS)

Samples for DRS measurements were prepared by heating the powder-like solid material, together with quartz fibres (50 ± 5 m in diameter), between circular brass electrodes (effective diameter 20 mm) above the clearing temperature. After subsequent cooling, samples with well-defined area and thickness were obtained. Dielectric measurements were performed using a high resolution dielectric analyser (ALPHA analyzer, Novocontrol Technologies) in combination with a Novocontrol Quatro temperature system providing excellent stability of the sample temperature (<0.05 K). Temperature dependent experiments were prepared by consecutive isothermal frequency sweeps (10^{-1} – 10^7 Hz) in the temperature range from $+250^\circ\text{C}$ to -120°C in steps of 5K, which resulted in an effective (mean) cooling rate of about 0.5 K/min. For an accurate determination of the relaxation time $\tau(T)$ and other relaxation parameters we fitted the dielectric loss spectra $\epsilon''(\omega)$ to the empirical Havriliak-Negami (HN) relaxation function [12]. A comprehensive description of analysis methods for dielectric data can be found in [13, 14].

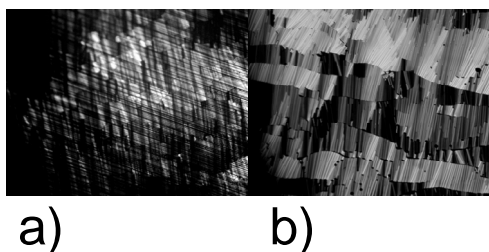


Figure 6.2: Pictures are taken in a) the reflection mode of the microscope, cooling scan, at 215.0°C, after shear applied on Al foil; b) the transmission mode of the microscope with crossed polarizers, cooling scan, at 221.7°C, after shear applied on glass. The magnification is the same in each case (x200).

6.2.7 DFT calculation

Initial molecular structures were optimised using the ab-initio COMPASS force field [15] and then further refined using the density function theory (DFT) code Dmol3 [16], which uses localised numerical atomic-orbitals. The dnd atomic basis set was used with the local density approximation (LDA) and effective core potentials. A medium grid was used in the numerical integration and a global real-space cutoff of 3.3. The convergence criterion in structure optimisations was 2×10^{-5} H.

6.3 Results and discussion

In liquid crystals, and in discotic liquid crystals particularly, the length of the tails is responsible for the phase transition temperature and for the existence of the liquid crystalline phase itself [8,9]. Therefore, the dramatic increase of the liquid crystalline phase temperature range for HAT6-TNF with comparison to pure HAT6 may be explained by location of TNF among the tails. To validate such a conclusion we have studied structure and dynamics of the pure compound and the charge transfer complex using alignment.

The optical texture of aligned HAT6-TNF by shear flow on glass and Al foil substrates taken

using optical microscope is shown on figure 2. These results show good quality alignment that is almost the same on both substrates, suggesting that the degree of alignment is independent of the substrate surface. Further information about geometry of alignment can be obtained from the diffraction patterns. Although IN6 is an inelastic and quasielastic scattering instrument, it was possible to obtain diffraction pattern of reasonable quality by taking the integrated elastic-peak intensity as a function of detector angle, these being shown for the sample in the two orientations in figure 6.3. We define two orientations for this experiment: "vertical" in which the shear axis is perpendicular to the scattering plane, and "horizontal" in which the column axis lies in the scattering plane (figure 6.4A).

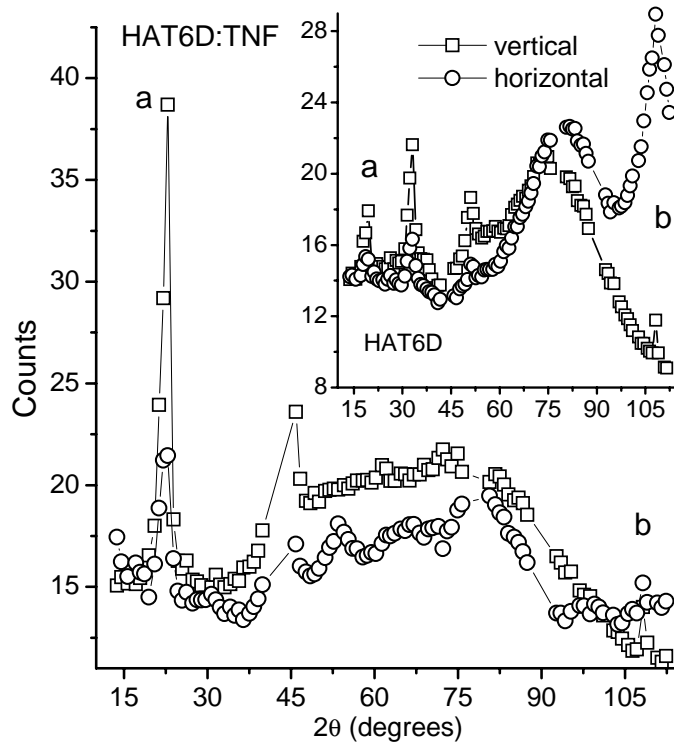


Figure 6.3: Diffraction pattern from quasielastic neutron scattering for HAT6 with deuterated tails, $T=367$ K (inset), and HAT6 with deuterated tails-TNF, $T=370$ K. "Vertical" in which the shear axis is perpendicular to the scattering plane, and "horizontal" in which the column axis lies in the scattering plane.

This has the advantage that the Bragg peak corresponding to the column separation will be most intense in the vertical orientation, whilst the peak due to the separation between disks in a given column will be more intense in the horizontal orientation [6]. A comparison of the relative intensities provides a measure of the degree of alignment, and by considering the geometry of experiment we are able to evaluate the geometry of alignment. In the case of the perfect orientation along the

shear direction the intensity of the Bragg peak corresponding to disc-separation will be equal to zero when momentum transfer vector is perpendicular to the columnar-director.

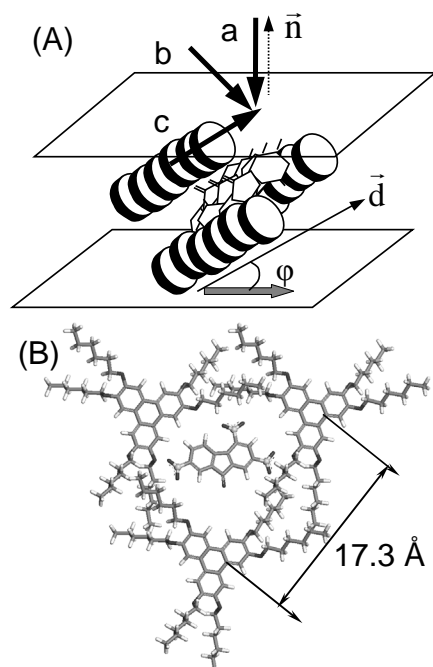


Figure 6.4: (A) Possible position of HAT6-TNF and experimental geometry for XRD and quasielastic neutron scattering: a) X-ray beam \perp shear plane (vertical orientation in QENS experiment); b) 45° angle between beam and shear plane; c) beam is almost parallel shear plane (horizontal orientation in QENS experiment); (B) schematic representation of TNF position among HAT6.

In the neutron scattering experiment we have used HAT6 in which the hydrogen atoms of the alkoxy tails have been replaced by deuterium in order to reduce the incoherent background. We will refer to this isotopomer as HAT6D. The diffraction patterns from IN6 for the two samples HAT6D-TNF and pure HAT6D are illustrated in figure 6.3 and the inset, respectively, for the two orientations, vertical and horizontal. The most important features are at 2θ values of 22.9° for HAT6D-TNF (19.5° -for HAT6D) and 108.2° that arise from the column-column and disk-disk separations, respectively. It is immediately evident that whilst the relative intensities of these peaks change between the two samples, the diffraction angles remain almost the same. This simple observation militates strongly against the formerly proposed structure in which the TNF molecules are located between the disks [3-7], since this would increase the disk-disk separation, probably by about a factor of 2. The difference in intensities of these Bragg-peaks between the two samples reveals that whilst the basic separations have been only slightly modified, the details of the structure

and symmetry may have changed significantly.

One would assume that the distance between HAT6 and TNF in "sandwich" arrangement will be similar to that between two HAT6 molecules. This would be reflected in neutron diffraction pattern. We have compared calculated neutron diffraction patterns for HAT6 and HAT6-TNF with "sandwich" arrangement for periodical structures using the same distance between the columns, fig. 6.5. The Bragg peak at around 17 Å, which corresponds to this separation, decreases in intensity when TNF is intercalated between the discs of HAT6, due to the overall reduction in scattering density of the columns. More importantly, the peak at about 3.5 Å, which corresponds to the disc-disc separation is almost absent in the calculated diffraction pattern of the HAT6-TNF complex, whilst there is a clear peak at this position for pure HAT6. This decrease reflects the loss of the periodicity in the sandwiched arrangement which is in direct conflict with the experimental observations. It is worth noting that if the scattering density of the two chemically distinct species were comparable (they are rather different here), it would be very difficult to distinguish between the two models.

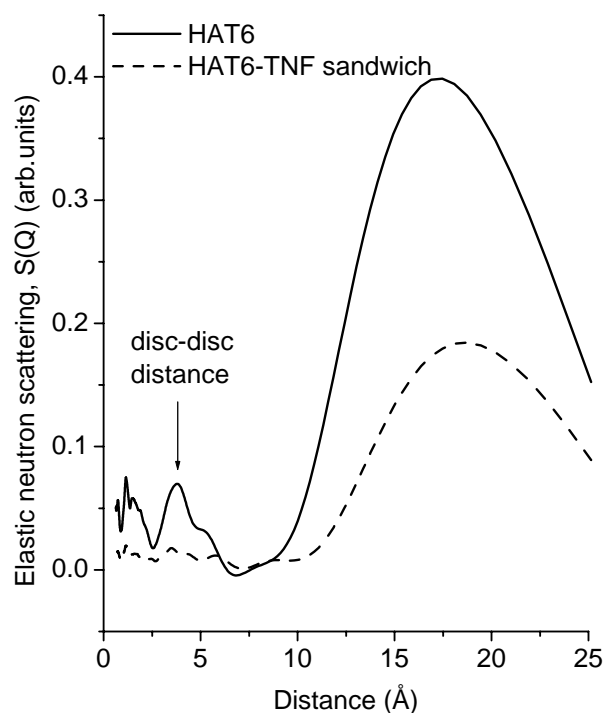


Figure 6.5: Calculated neutron diffraction pattern for pure HAT6 and sandwich arrangements for HAT6-TNF.

Previous calculations using XED (extended electron distribution) force field method [4,5] have also only considered models in which the TNF molecule is sandwiched between HAT6 molecules within a column. In view of the diffraction results above, it is interesting to enquire whether the energy of other TNF-sites, within the free volume afforded by the alkoxy tails of neighbouring columns, might also be energetically favourable, figure 6.4B. Clearly, a large number of possibilities exist and it is not feasible at present to use DFT methods to elucidate the global energy minimum in extended models of such complexity. Nevertheless, we have compared the energy gain of placing TNF between the two HAT1 disks (for simplicity the $O(CH_2)_5CH_3$ tails replaced by OCH_3) with the energy gain of placing the TNF and in juxtaposition within the tails of HAT6. These models are illustrated in figure 6.6. The local structures of these models were first optimised using the compass ab-initio based force-field, and then further optimised using DFT methods to determine the energies. Calculations were also made for optimised HAT dimers with the TNF constrained to be at a large distance from the dimer in order to determine the interaction energies. In both models the energy gain was close to 1.6eV from which we conclude that in terms of enthalpy, either location for TNF is equally possible. The probable explanation of position uncertainty may lie in the number of molecules that has been used for calculation. It was established experimentally that at small concentration discotic molecules have loose packing [17]. Although dimer formation energy was found to be almost constant it changes slightly depending on molecule concentration as well as length of the tails. Therefore, to calculate TNF position with more certainty one has to use a model consisting of a large number of HAT6 and TNF. The actual location of the TNF molecule could then be determined by entropy, which would tend to favour the positions between the tails, rather than the disks.

We have also performed X-ray diffraction on aligned samples to test our proposal that the TNF molecules lie within the tails of HAT6. Integrated intensities for different orientations of the aligned sample are shown in figure 6.7. Fig 6.4A represents possible orientation of HAT6-TNF columns with respect to film plane in XRD experiment. The Bragg peak corresponding to distance between columns is shifted from 17.31 for HAT6 to 15.12 in HAT6-TNF, fig.6.8, as was also observed in the neutron diffraction. A similar decrease has been detected in another charge transfer compound hexa (hexylthio) triphenylene-iodine, HHTT- I_3^- where ion I_3^- (acceptor) is located in between columns [18]. In agreement with the neutron-diffraction data, the position of the Bragg peak due to disk-disk separation is the same for HAT6 and HAT6-TNF, and again, as with the neutron-diffraction data for HAT6-TNF intensity is low. The X-ray intensity changes for HAT6-TNF substantially when the orientation is changed. We have fitted the X-ray diffraction data with Gaussian functions to determine the most probable number of peaks involved. The best χ^2 was obtained using 9 Gaussian functions to fit the experimental data in figure 6.7. We conclude that the increase in intensity, width and asymmetry at the base of the main feature of HAT6-TNF, compared to that of HAT6, arises from the superposition of several similar distances.

An analysis of χ scans at fixed 2θ can provide more information about structure of HAT6-TNF. The χ -variation of the integrated intensity of the main feature at $2\theta=5.84$, which arises from the column-column separation, is presented in fig.6.9. The presence of six similar features in this profile when sample has position a with respect to the X-ray beam implies that HAT6 molecules form a hexagonal lattice. The splitting of each of the main features further suggests that the hexagonal structure is hexagonal distorted, this being supported by the absence of high-order reflections that have been observed in pure HAT6 [19]. If the profile in figure 6.9b arose from a single reflection, the two major features would reveal the overall alignment of the sample. The observed splitting of these features probably arises from the presence of other reflections within the envelope of the

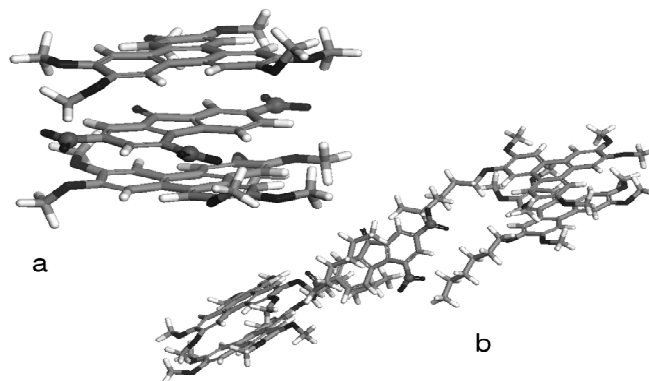


Figure 6.6: Models that have been used for DFT calculations. a) "sandwich"-TNF lies between two HAT1 molecules; b) TNF lies in tails of two HAT1 dimers with one tail containing six carbons.

peak in 2θ . In fact, the general pattern of peaks in figure 6.9a-c is consistent with a distorted hexagonal lattice for HAT6 with extra reflections due to the presence of TNF on ordered sites. The diffraction pattern of pure HAT6 [19] taken when the beam was parallel to the molecular plane of the disc contains arcs that correspond to alignment of columns and discs. In the case of HAT6-TNF alignment can be seen in orientation b) for columns and c) for discs, figure 6.9b and 6.10, respectively. Moreover, the χ scan reveals the presence of additional features, figure 6.9c, which may point to a twofold symmetry and the possibility of existence another unit cell formed by addition of TNF molecules. It seems likely that the HAT6 structure is perturbed in the complex, and that the lowering in symmetry is due to the presence of the TNF molecules.

The integrated intensity as a function of χ for the reflection at $2\theta=26.14^\circ$, corresponding to a disk-disk spacing 3.41 \AA^{-1} , is presented in figure 6.10. This profile can be fitted with 3 Gaussians of relative intensity 1:2:1. This strongly suggests that the major component arises from HAT 6 disk-disk spacings, and that the TNF-TNF has the same spacing. Further, the relative orientations of these spacings must be close to 68° . Based on the stoichiometry and the arguments above, we suggest a structure for HAT6-TNF as presented on fig.6.11.

It transpires that the shear alignment of HAT6 does not lead to the columns lying parallel to the substrate. This can be deduced from figure 6.3 where it is clear that in the pattern for HAT6D-TNF and HAT6D (in the inset) the peak in the vertical orientation from the disc-separation at $2\theta=108.2^\circ$ has significant intensity. This reflects the deviation of the alignment to the substrate,

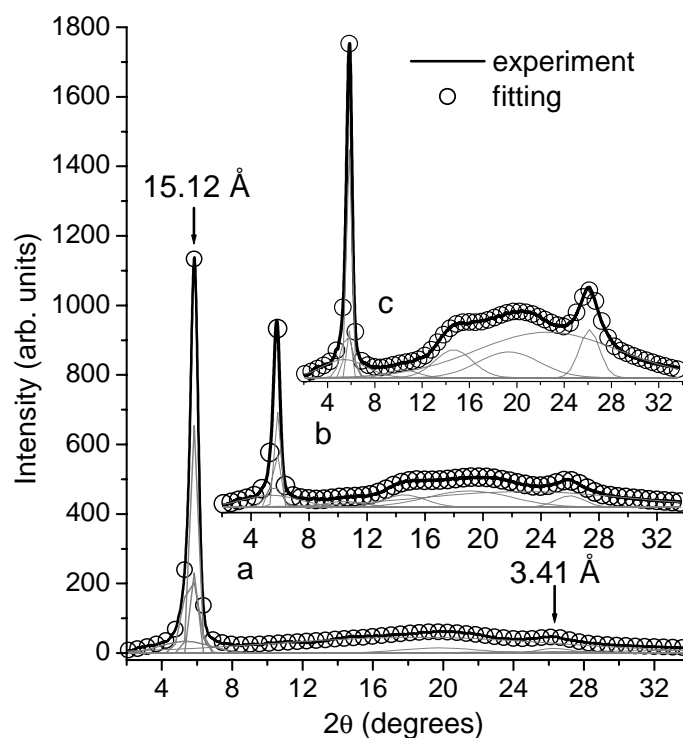


Figure 6.7: Integrated intensities for different position of sample with respect to X-ray beam at room temperature: a) beam is perpendicular; b) beam forms 45° angle with surface of sample; c) beam is almost parallel.

the ratio of the vertical and horizontal intensities being the tangent of the deviation. Comparing these relative intensities for HAT6D and HAT6D-TNF we find that the orientations with respect to the shear direction are 22° and 43° , respectively.

The inset in figure 6.12 shows the quasielastic neutron spectra of HAT6D at $T=367$ K and HAT6D-TNF at $T=370$ K in the two different orientations, horizontal and vertical, and the main part of figure 6.12 shows the relaxation curves obtained from the quasielastic spectra. For HAT6D we see no difference in relaxation, this being consistent with the orientation of the column vector (22° out of the sample plane), which gives components both in, and out of, the discotic molecular plane within the experimental scattering plane. HAT6D has six remaining H-atoms on the core that were not deuterated, whilst the non-deuterated TNF has 5. In HAT6D-TNF we therefore expect an almost equal contribution to the scattering from both types of molecule. What we observe in this case is a faster relaxation with the sample in the horizontal orientation and a much slower relaxation in the vertical orientation. The lower mobility of the HAT6 cores arises from reduced degrees of freedom that is induced by the presence of TNF. Without the mixture containing deuterated TNF it is difficult to interpret these data unambiguously. Nevertheless, it is clear from the spectrum of HAT6D that we would expect the same spectrum in both orientations for this molecule and we assume it gives a slow component to the spectra of the mixture in both orientations. The fast

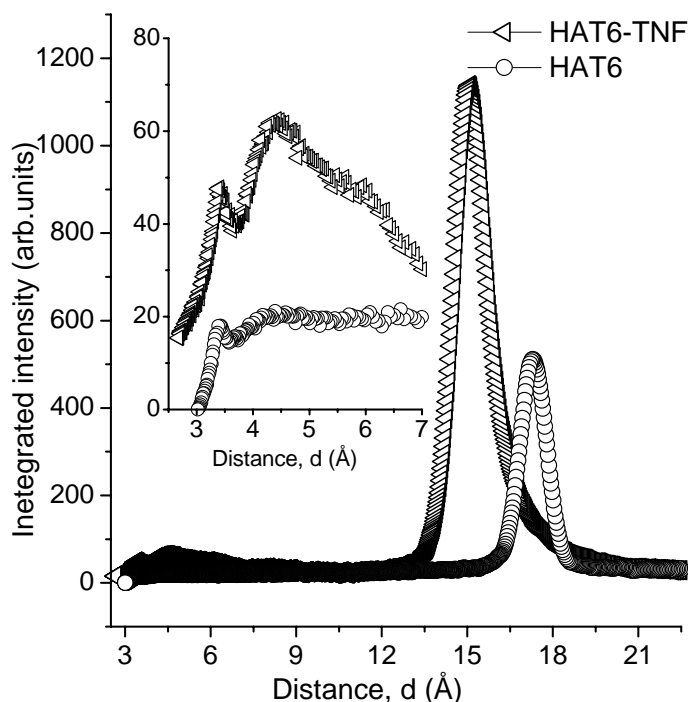


Figure 6.8: Integrated intensities over χ for pure HAT6 and charge transfer mixture as a function of d spacing. HAT6 diffraction has been performed at $T=80^\circ\text{C}$ on cooling and HAT6-TNF-at room temperature, both for 30 min.

component that is seen in the spectrum of the horizontal orientation arises from TNF, which is overlaid on the narrower quasielastic signal from HAT6D, and becomes a "probe" of the motion of the tails. This would require that the molecular planes of TNF are aligned close to perpendicular with the shear direction, that is at about 43° to the HAT6D molecular planes. We clearly have to be cautious, but this proposal is consistent with our proposed structure. This strongly suggests that addition of TNF as an acceptor stiffens HAT6 columns, this being consistent with the structural data, quasielastic scattering, and the wider stability-range of the columnar phase.

Further indirect evidence for our structural model comes from dielectric measurements, which provided detailed information about the slow and medium-fast dynamics of HAT6-TNF complexes. Figure 6.13 displays the frequency and temperature dependence of the dielectric loss $\varepsilon''(f, T)$ revealing three well-resolved molecular relaxation processes (α_1 , α_2 and γ). The respective peak relaxation times $\tau(T)$, obtained by an Havriliak-Negami fit, are summarised in an Arrhenius plot (Fig. 6.14, filled symbols) together with data recently measured on pure HAT6 and an asymmetrically substituted HAT6 variant (HAT6-C₁₀Br) [20]. While the γ -process, associated with local conformation fluctuations in the alkyl tails, appears to be very similar in all three compounds, major differences are seen in the two, "curved" relaxation processes α_1 and α_2 , which have been assigned in a previous study [18] to the columnar glass transition (α_2) and a low-temperature

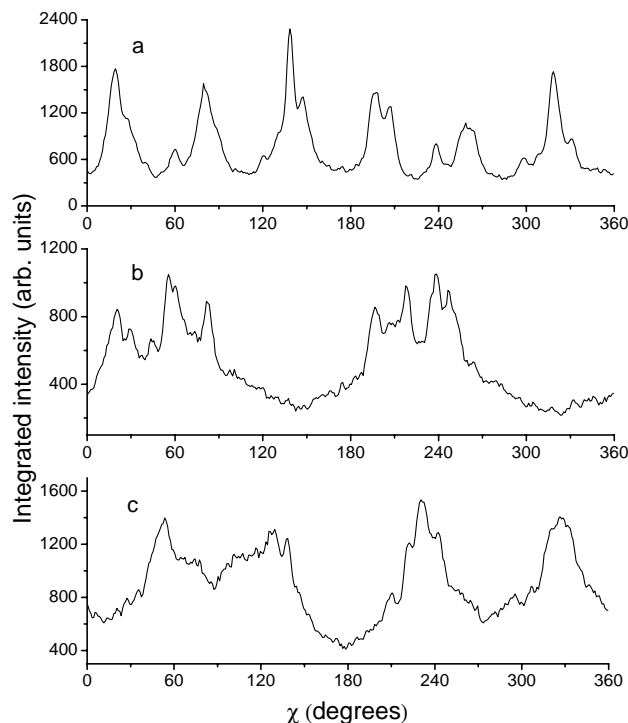


Figure 6.9: Azimuthal scan, χ , of HAT6-TNF at room temperature, $2\theta=5.84^\circ$: a) X-ray beam is oriented perpendicular to the plane of the sample; b) 45° angle between sample plane and beam; c) beam is oriented almost parallel with respect to the plane.

poly(ethylen)-like glass transition (α_1) indicating cooperative dynamics of a nano-phase separated tail-fraction.

The appearance of the high temperature dielectric process (α_1) for HAT6-TNF leads us to the following conclusions: i) In contrast to neat HAT6 that lacks the dielectric manifestation of its columnar glass transition for symmetry reasons, i.e. due to the absence of a net radial dipole moment linked to the rotational diffusion of HAT6 cores around the columnar axis, such an α_2 relaxation is very prominent for the complex HAT6-TNF. Obviously, TNF-molecules couple to the (cooperative) rotational diffusion of HAT6 moieties in such a way, that the dynamic HAT6-TNF complexes become asymmetric and thus show net polarity. ii) To address the question whether the polar TNF molecules act as polar "probes" in an intra-columnar or inter-columnar arrangement, we will now discuss the short time dynamics of the relaxation time curves $\tau_{\alpha_2}(T)$ given in Fig. 6.14. While the relaxation times $\tau_{\alpha_2}(T)$ for HAT6-C₁₀Br and HAT6-TNF show an increasing discrepancy towards lower temperatures, which is an expression of different columnar glass transition temperatures as the result of differences in the molecular packing, there is a remarkable coincidence in the high-temperature data. Having in mind that the cooperative rotational dynamics of HAT6 cores should be very sensitive to the packing and specific interactions between stacked discotic constituents, the coincidence in the relaxation time data clearly implies a high degree of structural similarity in the

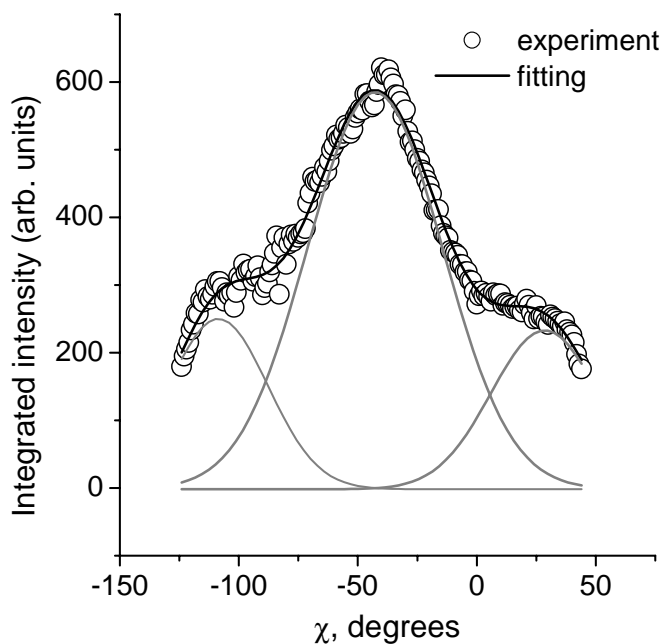


Figure 6.10: Azimuthal scan, χ , of HAT6-TNF at room temperature, $2\theta=108.21^\circ$, when beam is oriented almost parallel with respect to the plane. Fitting has been performed with 3 Gaussian functions.

interdisc packing in both compounds.

Additional support for the idea, that TNF molecules are located on inter-columnar positions, can be obtained from a comparison of the temperature dependences of the relaxation time data $\tau_{\alpha_1}(T)$, which relate to the cooperative dynamics of the disordered aliphatic tails. From Fig. 6.14 it is evident that at high temperatures, the dynamics of HAT6-TNF resembles that of HAT6-C₁₀Br, while τ_{α_1} for pure HAT6 becomes relatively slow. The respective differences between HAT6 and HAT6-C₁₀Br have been discussed earlier [20] and were rationalised by the different position of the sensing dipolar group within the aliphatic tail. In this picture it is plausible that for HAT6 the ether group linking the triphenylen core to the spacer senses the slowest contribution of the cooperative "aliphatic" glass transition, while for HAT6-C₁₀Br the bromid group emphasises the faster dynamics of the unconstrained tail ends. Hence, the striking analogy in the high temperature behaviour of the α_1 -relaxation times between HAT6-C₁₀Br and HAT6-TNF again implies a position of the TNF moieties on a peripheral position in analogy to the bromid dipole.

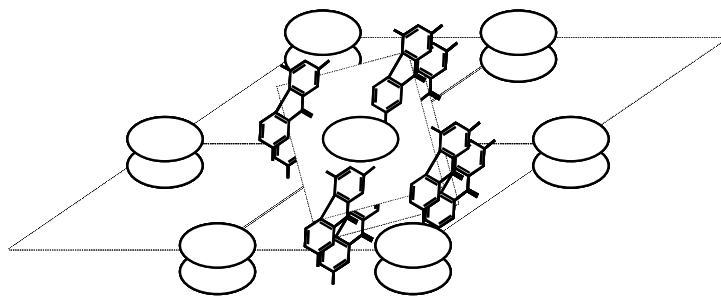


Figure 6.11: Schematic representation of possible HAT6-TNF arrangement. Discs represent triphenylene cores, tails are omitted for clarity. TNF lies between columns and forms columns.

6.4 Conclusions

Whilst it would take a rather thorough crystallographic study to obtain the details of the crystal structure of the HAT6-TNF complex, all of our data, neutron scattering, x-ray diffraction and DFT calculations combine to show unambiguously that the TNF molecules are not sandwiched in a coplanar manner between HAT6 molecules, but are located between the columns within the tails of the discotic molecules. This juxtaposition stiffens the columns, this being consistent with the extended stability range of HAT6-TNF compared with pure HAT6, the greater resistance to shear, and the slower local dynamics as shown by quasielastic neutron scattering. This new structure has important consequences for the potential use of discotic materials, since the "sandwiched" structure would be expected to reduce the charge-transfer rate along the columns due to the reduced π -overlap. It now transpires that the TNF is between the columns where its stiffening effect would tend to improve the overall charge-transfer rate along the columns, and could eventually help in charge-separation of excitons, again leading to improved performance.

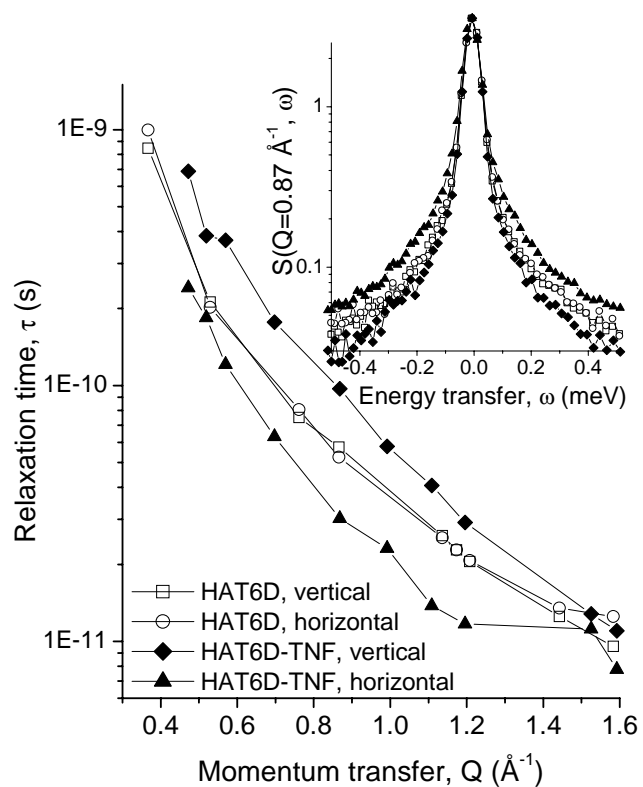


Figure 6.12: Relaxation time τ versus Q for HAT6 with deuterated tails, without and with TNF presence in two different orientations. Inset: quasielastic neutron scattering curves for HAT6D, $T=367\text{K}$, and HAT6D-TNF, $T=370\text{K}$.

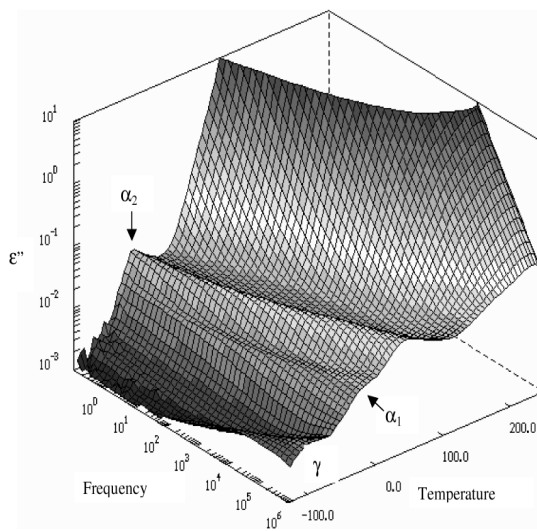


Figure 6.13: 3D representation of the dielectric loss $\epsilon''(f, T)$ measured during cooling of a HAT6-TNF complex.

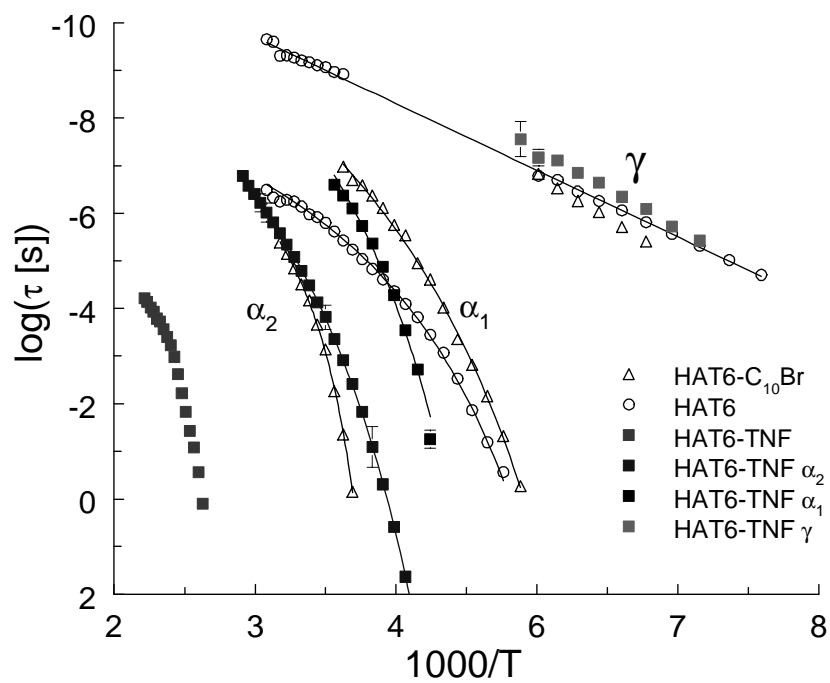


Figure 6.14: Arrhenius diagram of the four relaxation processes of HAT6-TNF (squares) in comparison with reference data from pure HAT6 and the asymmetrically substituted derivate HAT6-C₁₀Br.

Bibliography

- [1] L. D. A. Siebbeles and B. Movaghar, *J. of Chem. Phys.*, 1999, 110, 10162.
- [2] L. Schmidt-Mende, A. Fechtenkötter, K. Müllen, E. Moons, R. H. Friend, J. D. MacKenzie, *Science*, 2001, 293, 1119.
- [3] D. Markovitsi, H. Bengs and H. Ringsdorf, *J. Chem. Soc. Faraday Trans.*, 1992, 88, 1275.
- [4] O. R. Lozman, R.J. Bushby and J.G. Vinter, *J. Chem. Soc. Perkin Trans.*, 2001, 2, 1446.
- [5] N. Boden, R. J. Bushby and O.R. Lozman, *Mol. Cryst. Liq. Cryst.*, 2004, 411, 345.
- [6] K. Praefcke and J. D. Holbrey, *J. of Inclusion Phenomena and Molecular Recognition in Chemistry*, 1996, 24, 19.
- [7] H. Bengs, O. Karthaus, H. Ringsdorf, C. Baehr, M. Ebert and J. H. Wendorff, *Liquid Crystals*, 1991 10, 161
- [8] P. Etchegoin, *Phys. Rev. E*, 1997 56, 538.
- [9] I. Paraschiv, P. Delforterie, M. Giesbers, M. A. Posthumus A. T. M. Marcelis, H. Zuilhof, E. J. R. Sudhölter, *Liquid Crystals*, 2005 32, 977.
- [10] C. W. Struijk, A. B. Sieval, J. E.J. Dakhorst, M. van Dijk, P. Kimkes, R. B.M. Koehorst, H. Donker, T. J. Schaafsma, S. J. Picken, A. M. van der Craats, J. M. Warman, H. Zuilhof, and E. J.R. Sudhölter, *J. Am. Chem. Soc.*, 2000 122, 11057.
- [11] B. Hammouda, J. Mang and S. Kumar, *Phys. Rev. E*, 1995, 51, 6282.
- [12] S. Havriliak, S. Negami, *Polymer* 8 (1967) 161.
- [13] M. Wübbenhorst, J. van Turnhout, *J. Non-Cryst. Solids* 305 (2002) 40-49.
- [14] J. van Turnhout, M. Wübbenhorst, *J. Non-Cryst. Solids* 305 (2002) 50-58.
- [15] H. J. Sun, *Phys. Chem.* 102, 1998, 7338.
- [16] B. Delley, *J. Chem. Phys.*, 1990, 92, 508.
- [17] E. Y. Sheu, K.S. Liang and L. Y. Chiang, *J. Phys France*, 50 (1989), 1279-1295
- [18] G. B. M. Vaughan, P. A. Heiney, J. P. McCauley, Jr., and A. B. Smith, III, *Phys. Rev. B*, 1992, 46, 2787.

- [19] A.M. Levelut, *J. Phys.*, 40(15), 1979, L-81.
- [20] Z. Yildirim, M. Wübbenhorst, E. Mendes, S. J. Picken, I. Paraschiv, A. T. M. Marcelis, H. Zuilhof, and E. J. R. Sudhölter, *J. Non-Cryst. Solids*, **351**, pp. 2622-2628, 2005.

Chapter 7

Conductivity of discotic liquid crystals

7.1 Introduction

Some discotic molecules are capable of assembling themselves into columnar liquid-crystal phases, and these have attracted considerable attention over the past decade as potential photovoltaic materials¹ [1,2]. The stacking provides π overlap between neighbouring molecules providing a 1D path that allows mobility of the charge carriers. Their mobility in the direction of the overlap exceeds that in perpendicular direction making electronic transport highly anisotropic [3]. Discotic liquid-crystals have a range of band-gaps, depending among other factors on the molecular size, and generation of charge carriers opens the possibility to use such materials in the future. Unfortunately, carrier mobility appeared to be low. Until recently the average value of mobility for discotic liquid-crystals was approximately $0.001\text{-}0.1\text{ cm}^2\text{V}^{-1}\text{s}^{-1}$ [4]. It has been established [5] that doping increases the mobility and concentration of the charge carriers by separating electron-hole pair and preventing their recombination. Although carrier mobilities for different hydrocarbon liquids, discotics and charge-transfer complexes have been evaluated extensively [6], recent studies have revealed large discrepancies with previous evaluations [7,8]. Since hydrocarbon liquids are conformationally similar to the liquid crystalline tails [9] and their electron mobility was underestimated one would assume that charge carrier mobility of discotic liquid crystals was underestimated as well. The main reason for this is the approach that was used [10], which does not take into account dynamics of molecules and the phase transition characteristics that affect electrons or/and holes. In the present paper we investigate the complex dynamics of the model system, HAT6, and then relate these dynamics to the scattering rate of the charge carriers. The central question addressed in this paper is: can we relate the relaxation processes measured by quasielastic neutron scattering to those that scatter the electron (or hole), despite the large differences in the timescales involved. In order to achieve this we use a model suggested by Y. Berlin [11], which not only gives physically meaningful parameters, but in principle provides parameters that characterize the whole system over a very wide range of timescales.

¹This chapter is based on paper: O. Kruglova, F. C. Grozema, R.D. Abellon F.M. Mulder, J.A. Stride, S.J. Picken and G.J. Kearley, in preparation

We have chosen to study two systems. Firstly, pure hexakis(n-hexyloxy) triphenylene (HAT6) and secondly the complex, HAT6-TNF, where HAT6 acts as the donor, and 2,4,7-trinitro-9-fluorenone (TNF) as the acceptor. The dynamics of the system over all timescales are characterised by the parameters β and τ from equation 1.42, and if the motion measured by quasielastic neutron scattering (faster than ~ 100 ps) is related to the dynamics by which holes or electrons find their way to traps, we would anticipate similar values of b for the two experimentally distinct processes.

7.2 Experimental techniques

7.2.1 Quasielastic neutron scattering

QENS spectra for HAT6 were obtained using the IN6 spectrometer at Institute Laue Langevin in France with incident wavelength of 5.9Å and standard temperature-control. Measurements were performed at temperatures of T=364K, 370K for the protonated HAT6 and at T=367K for the tail-deuterated analogue. HAT6-TNF were measured at T= 358K, 370K, 400K for horizontal orientation (see below) and T=370K, 400K, 440K for vertical orientation. Formally, T=370K for HAT6 corresponds to the liquid crystalline→liquid phase transition. Data were corrected using standard algorithms and analysed using locally written routines. To study dynamics of pure HAT6 and HAT6-TNF in more detail we have aligned both samples. This was achieved by heating the sample to its melting point and then cooling, with the alignment by shear-flow being made as soon as the columnar liquid-crystal phase was formed. It has been established [12] that discotic liquid-crystals are not oriented along shear flow but rather form an angle with direction of the shear. In case of pure HAT6 the angle between liquid-crystalline director and alignment direction is $\varphi \sim 22^\circ$ and in the case of HAT6-TNF it is $\varphi \sim 43^\circ$, fig 7.1. We distinguish two orientations in the neutron scattering experiment. "Vertical orientation" refers to the arrangement in which the shear-direction is perpendicular to the scattering plane, fig.7.1, and "horizontal orientation" in which the shear-direction is in the scattering plane, fig.7.1.

7.2.2 Pulse-Radiolysis Time-Resolved Conductivity

For the PR-TRMC measurements a cell was used which consists of a 14 mm length of rectangular, 7.1x3.55 mm, copper wave guide closed at one end with a metal plate. Approximately 30 mg of the HAT6-TNF mixture was placed in a 6x3x2 mm cavity in a polyamide block that exactly fits inside the copper microwave cell. Charges were generated in the sample by irradiation with 3 MeV electrons from a Van de Graaff accelerator [13-15].

7.3 Results and discussion

7.3.1 Dynamics

For interpretation of the quasielastic neutron scattering data and the time resolved conductivity measurements we have used the model for relaxation kinetics in correlating environment as described in Chapter 1. Since the neutron data are measured in the frequency domain, these were transformed to the time domain using an inverse Fourier transform in order to obtain the intermediate scattering function, $F(Q,t)$. The resolution function of IN6 was deconvoluted by dividing the sample $F(Q,t)$ by that of vanadium in which there is no quasielastic signal. Figure 7.2 illustrates $F(Q,t)$, for HAT6

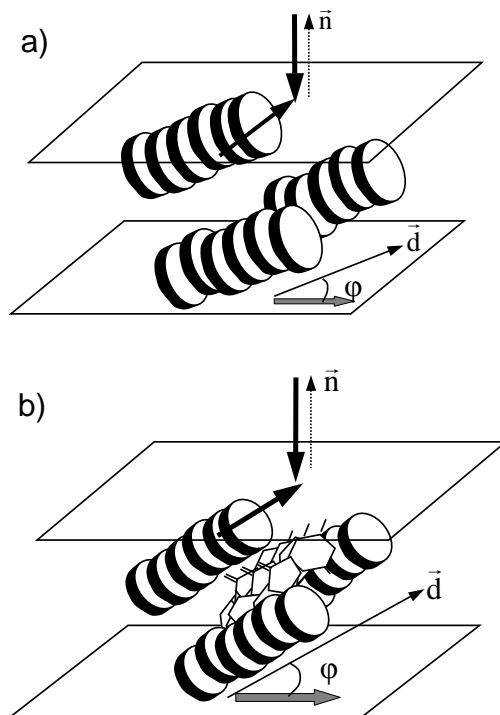


Figure 7.1: Orientation of HAT6 and HAT6-TNF after shear alignment; \vec{n} is the normal to the sample holder plane, \vec{d} is liquid-crystal director, and the grey arrow shows the direction of orientation. φ is the angle between director and orientation of alignment. The black arrows represent the incident neutron beam, and the orientation where normal is parallel to the neutron beam is denoted as "vertical" and orientation where normal is perpendicular to the neutron beam is denoted as "horizontal".

and HAT6-TNF in the vertical orientation, and it is clear that the shapes of these are Q-dependent. The relaxation is also sensitive to the presence of TNF, which show a slowing of the relaxation at both Q-values, as might be expected from the wider stability-range of the columnar phase for the HAT6-TNF complex.

7.3.2 Effect of TNF on the molecular relaxation processes

By fitting the data with equation 1.42 we have obtained the relaxation time as a function of Q, $\tau(Q)$, this being shown for HAT6 with deuterated tails (HAT6D) and HAT6 with deuterated tails-TNF (HAT6D-TNF) in both orientations in figure 7.3. For HAT6D the quasielastic signal comes mainly from the 6 core H-atoms and it seems that this signal is essentially the same in both orientations, as anticipated from figure 7.1. This is in marked contrast with the large difference between $\tau(Q)$ for the two orientations of HAT6D-TNF. The motion seen in vertical orientation of the complex is

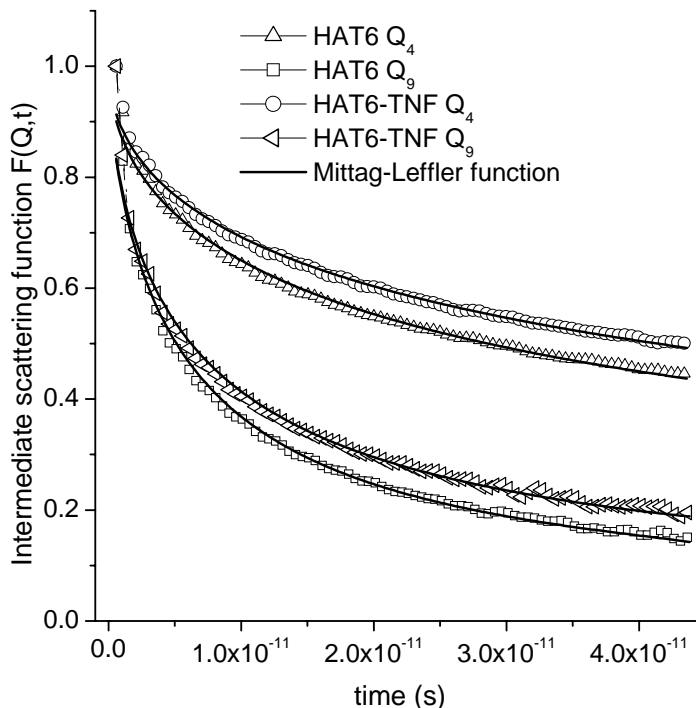


Figure 7.2: Intermediate scattering function $F(Q,t)$ for HAT6 and HAT6-TNF in vertical orientation, $Q_4=0.7 \text{ \AA}^{-1}$ and $Q_9=1.27 \text{ \AA}^{-1}$ for $T=370\text{K}$ fitted with Mittag-Leffler function.

slower than that of HAT6D, whilst the situation is quite the opposite for the horizontal orientation. Not only is the alignment angle, a , different for the complex, but also a significant portion of the measured signal comes from the TNF molecule, and it follows that the observed differences in $\tau(Q)$ are consistent with our recent proposal that the TNF molecules are situated amongst the alkoxy-tails of HAT6 [12]. The slower relaxation seen in the in vertical orientation of the complex reflects the net movement of HAT6 cores and TNF molecules, whilst the faster relaxation seen in the horizontal orientation arises from other TNF motions amongst the HAT6 tails.

This interpretation is supported by the orientation dependence of relaxation time dependence for protonated samples illustrated in fig 7.4. There is only a slight difference in $\tau(Q)$ between the two orientations of protonated HAT6-TNF, and the result for HAT6D-TNF horizontal is also rather similar to these. The deviation of the latter above $Q=1.2 \text{ \AA}^{-1}$ may be related to the size of the TNF molecule.

7.3.3 Fluctuations

As described in Chapter 1 our main interest is to understand the potential-barrier fluctuations, $\frac{\Delta E}{E} = 1 - \beta$, that are an essential part of our model since these determine both the molecular dynamics, and the dynamics of the charges that are coupled to the molecular system. QENS

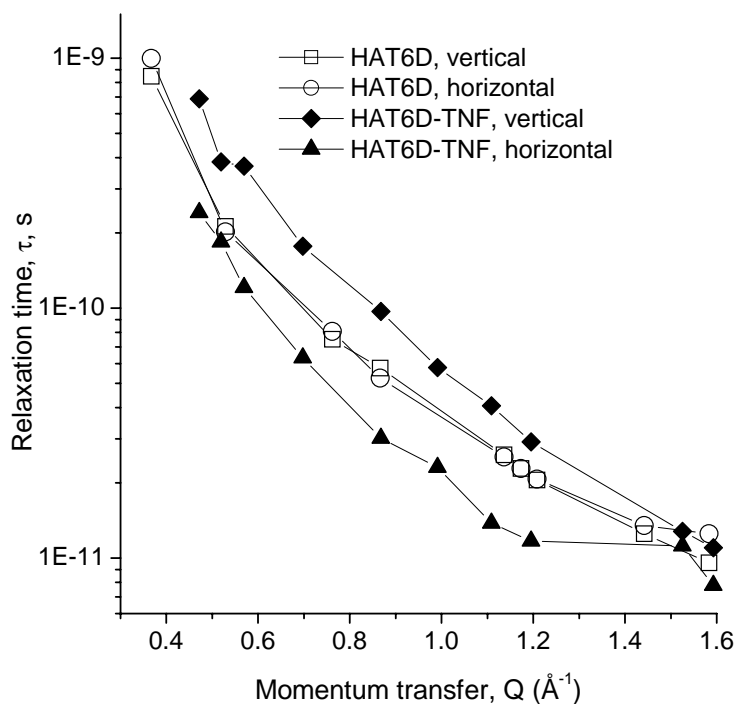


Figure 7.3: Dependence of relaxation time τ via momentum transfer Q for HAT6D and HAT6D-TNF in two orientations, $T=370\text{K}$.

has the advantage that it measures the spatial dependence of the molecular relaxation, whereas TRMC decay measures the mobility of charges over some distance that is related to the microwave frequency. These can only be connected via β on a length scale where these distances coincide.

In figures 7.5a, we illustrate the Q -dependence of β for HAT6, with protonated alkoxy tails, and HAT6D, with deuterated tails. It can be seen that there is rather little difference between these since the cores and tails are part of the same overall dynamical system. At high Q the curves tend to separate as the length-scale starts to approach the segment-length of the tails. Figure 7.5b shows that the addition of TNF has little effect on β (but a strong effect on τ) except in the vertical sample orientation when the HAT6 tails are deuterated. This arrangement measures the movement of the HAT6 cores and the TNF molecules in the plane perpendicular to the shear direction. Comparison with figure 7.5a shows that the difference here has been caused by the addition of TNF which has increased the overall dispersion as measured in the direction above. This indicates that the TNF increases the trapping (and dispersion) within the plane of the discotic molecules, but has little effect on trapping in the column direction which is consistent with the TNF being located within the alkoxy tails of HAT6 rather than between the cores as is sometimes supposed.

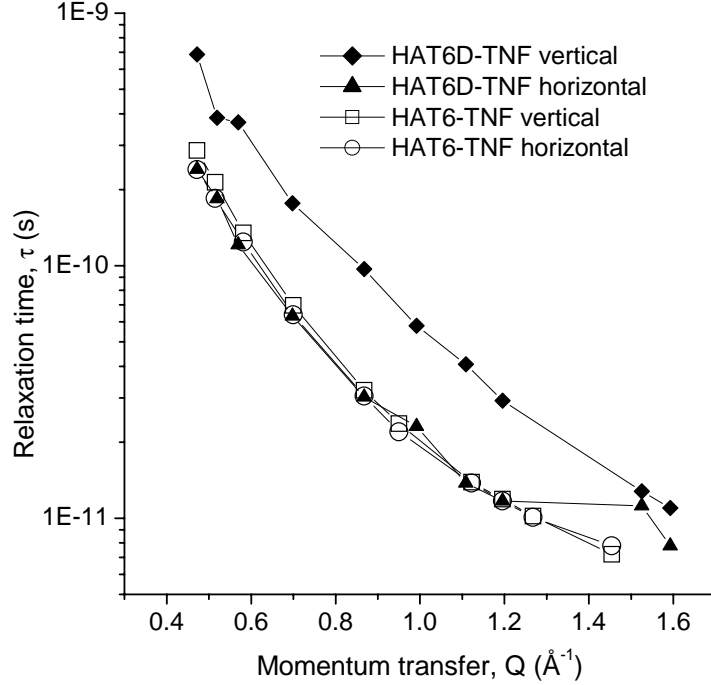


Figure 7.4: Comparison of $\tau(Q)$ between HAT6D-TNF and HAT6-TNF in two orientations, $T=370K$.

7.3.4 Conductivity

It was established by Devos and Lannoo [16] that those π -electron (holes) that contribute the most to the overall conductivity are coupled to the phonons. This coupling, λ , is inversely related to number of atoms in molecule involved in π -states, $\lambda \sim N_{\pi}^{-1}$. Clearly, charge-carrier motion is related to molecular motion and in the present paper we enquire to what extent they may be described by a common relaxation model. We would then be able to use the same equation 1.39, p. 11 that was used for the molecular relaxation kinetics, and its solution in terms of Mittag-Leffler function, eq. 1.42.

From the Drude model the electron mobility can be expressed as

$$\mu = \frac{e}{m_e} \tau, \quad (7.1)$$

where e is elementary charge, m_e is electron mass and τ is the collision or scattering time. We have assumed that the effective mass equals the electron mass. The Drude model implies free or quasifree electrons [17], and because in the experiment the observed change in conductivity is mostly due to quasi-free charge carriers (in particular holes) we can use this model to estimate the charge carrier mobility. The relaxation (scattering) time of the charge carriers can be obtained from eq. 7.1. Within our assumption the charge carriers will move along with the molecular rearrangements until they become trapped, and the experiment therefore measures the mobility of the charge-carriers on

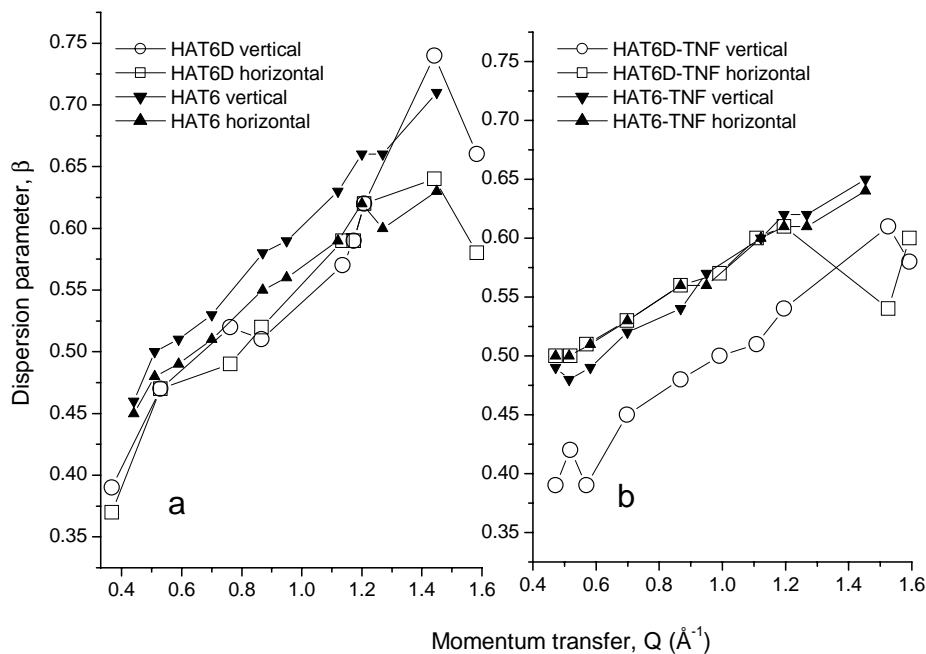


Figure 7.5: a) Dispersion, β , versus Q for HAT6D and HAT6 in the two orientations. b) Dispersion, β , versus Q for the complex HAT6-TNF in the two orientation with protonated and deuterated HAT6 tails. Both figures are for a sample temperature of 370K.

their way to the traps. As mentioned above, the dispersion parameter, β , is connected with entropic index, eq. 1.48, which describes the behavior of the energy landscape of the system. Because there is strong coupling between molecular and charge-carrier motion, we would anticipate that β should be rather similar for the two processes, albeit that we actually measure these on very different timescales. Further, if true, this supposition would allow us to calculate the mobility of quasifree charge carriers directly, without additional assumptions [7].

7.3.5 Conductivity and dynamics of HAT6 and complex HAT6-TNF

In figure 7.6 the radiation induced conductivity in HAT6 is shown as a function of time both in the crystalline phase at 298K, and in the columnar liquid-crystalline phase at 363K. The inset shows the raw data as obtained directly from the experiment. Although the raw data shows clear difference in intensity between 298 and 363K, after normalization to their maxima the curves have fallen together. This illustrates that the decay kinetics of charge carriers is independent of the phase. This fact can be explained if one takes into account that main contribution to conductivity is the core charge carriers. During phase transition, C \rightarrow LC, core orientational order parameter does not change much ranging from 0.95-0.9. So, cores stay highly ordered [18] One would expect then that qualitative picture of molecular dynamics will not change much either from crystalline to liquid crystalline phase. Since charge carrier and molecular motions are coupled the shape of the

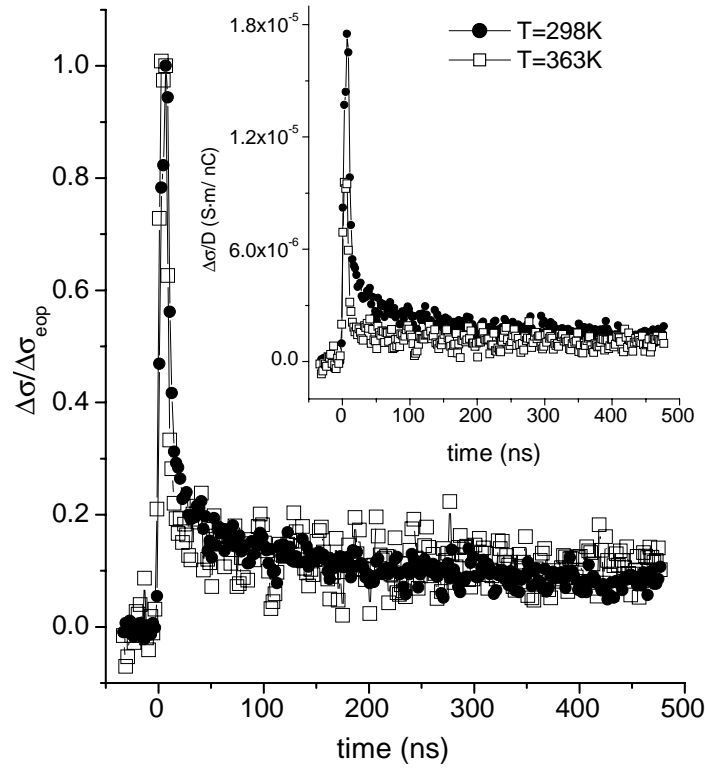


Figure 7.6: Transients for HAT6 (normalized on the end of the pulse conductivity) obtained at 298K (crystalline phase) and 363K (discotic phase). Inset: conductivity transients for HAT6 as obtained from experiment.

conductivity decay curve and relaxation time should remain unaltered. The drop in conductivity points out on change in concentration of charge carriers, which occurs during phase transition. The same intensity discontinuity was observed for HAT6 in fluorescence spectra [19]. The intensity of the line in fluorescence spectroscopy is proportional to the concentration of excited electronic states. HAT6 undergoes first order phase transition during transition from crystalline to liquid crystalline phase [20]. So, the only parameter that has discontinuity for this kind of transition in semiconductors is concentration of charge carriers [21, 22]. The normalized transients have been fitted with equation 1.42, p.12 giving the value of dispersion parameter $\beta=0.62$ and the value of the relaxation time $\tau=15.3$ ns for both curves, fig 7.7. The quality of the fit is good, but there is some deviation at short times that is probably due to recovery from the pulse.

We would anticipate that the changes to the molecular dynamics that were seen on addition of the acceptor, TNF, would also be present in the time-resolved conductivity measurements. A comparison between transients for HAT6 and HAT6-TNF is shown on figure 7.8, where it can be seen that at 298K the complex, HAT6-TNF, decays more slowly than the pure compound, HAT6. This is entirely consistent with the slower molecular dynamics seen with neutron scattering on the shorter timescale. Table 1 shows that as the temperature is increased, the decay of the HAT6-

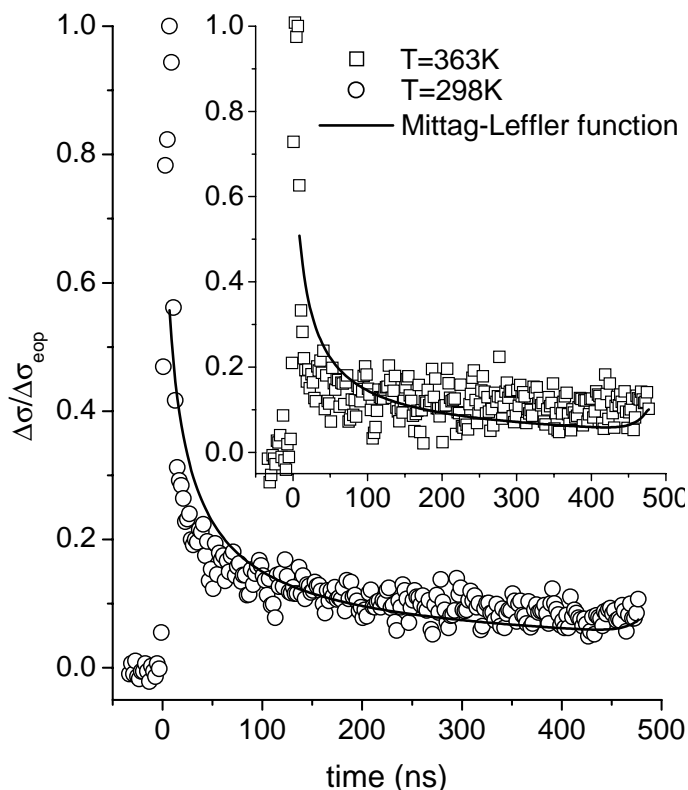


Figure 7.7: Fits of HAT6 normalized transients using the Mittag-Leffler function.

TNF transients generally also increases, this being in agreement with the molecular dynamics. The higher value at 300K for the complex may result from the onset of a dynamical process that couples more efficiently with the charge. By fitting these data with expression 1.42, p. 12 we obtain values for the dispersion parameter $\beta=0.59$, $\tau=35.2$ ns for $T=248$ K and $\beta=0.6$, $\tau=0.19$ μ s for $T=298$ K, fig. 7.9. From the relaxation time, τ , we can calculate charge-carrier mobility from expression 7.1, Table 1.

	Temperature							
	173	223	248	298	323	348	373	393
Relaxation time, ns	22.2	41.5	35.2	186	119	97.2	127	151
Mobility, $\text{cm}^2\text{V}^{-1}\text{s}^{-1}$	0.39	0.73	0.62	3.27	2.09	1.71	2.23	2.65

The maximum in this table, $\mu = 3.27$ $\text{cm}^2\text{V}^{-1}\text{s}^{-1}$, at $T=298$ K, may reflect a dynamical process that is particularly strongly coupled to the charge mobility. Drop in the relaxation time and, therefore, mobility might be caused by the "switching off" of TNF motion. Comparing two conductivity decay curves for HAT6 at $T=298$ K and HAT6-TNF at $T=248$ K, fig. 7.8, one can see their resemblance in shape although relaxation times are slightly different. The dispersion parameter, β , characterizes the delay in relaxation time due to fluctuations of the potential barrier, and it

is connected with the fundamental parameter, η , the entropic index, that defines the kinetics in a particular area. If the neutron scattering and time-resolved conductivity experiments are measuring different parts of the same global relaxation process described by equation 1.42, we would expect some correspondence in the value of β . The momentum transfer, Q , is a measure of the length scale, and in the neutron scattering experiment β clearly depends on Q . For HAT6 $\beta=0.62$ from conductivity measurements, which matches the neutron scattering value at $Q=1.12 \text{ \AA}^{-1}$. Assuming our basic supposition to be correct, this provides a distance of 5.6 \AA for the average distance moved by the charges following the microwave radiation. This value seems entirely reasonable. If both the molecular relaxation and mobility decay are described by the same global kinetic equation, 1.39, p.11, we would also anticipate the same temperature dependence of β (at the appropriate Q). This comparison is made in figure 8, where it is clear that over the temperature-range where data are available from both techniques, there is remarkable consistency in the β -values.

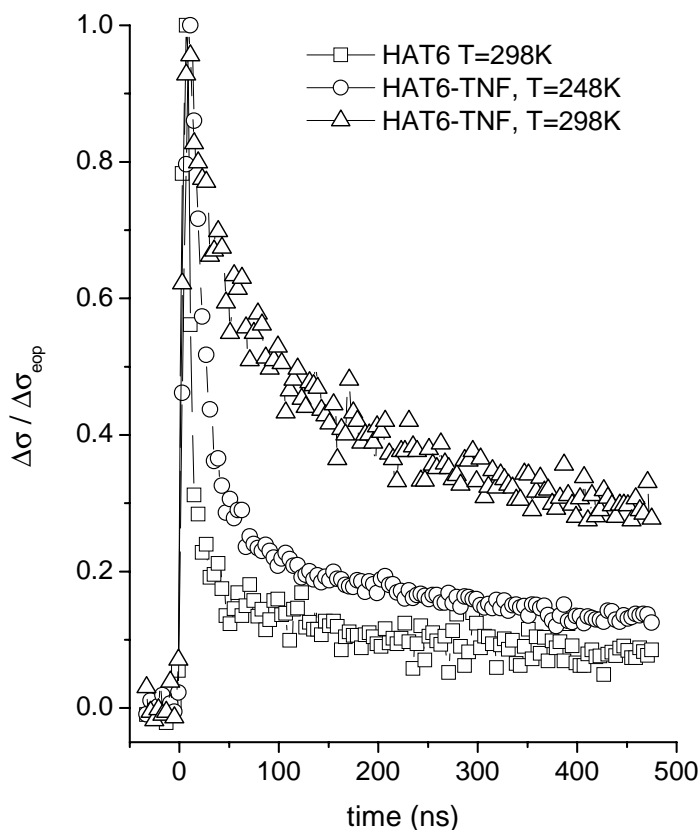


Figure 7.8: A comparison of normalized transients for HAT6 and HAT6-TNF.

7.3.6 Charge-molecule coupling strength

It is interesting to try to quantify the coupling of the charge and molecular dynamics so that the effects of complexation can also be quantified. We will show in a forthcoming publication [23] that the Q-dependence of the relaxation-time obtained from QENS for the HAT6 and HAT6-TNF has Lévy distribution, $\tau_s(Q) = \exp(-a_s Q^\alpha)$, where a_s is an amplitude parameter, and α is the Lévy index. Within the assumption that the relaxation kinetics of charge carriers is described by the same dynamical equation as the molecular relaxation, the Q-dependence of the relaxation time will also have a Lévy distribution, $\tau_{cc}(Q) = \exp(-a_{cc} Q^\alpha)$, with the same Lévy index, α . The only term that differs is the amplitude parameter, a_s and a_{cc} . This amplitude parameter takes into account number of particles that contribute to the relaxation time at particular Q, and their characteristic jump-length. On building a relation for relaxation times in order to obtain information about influence of the molecular motion on the motion of the charge carriers we obtain:

$$\frac{\tau_s}{\tau_{cc}} = \exp(-(a_s - a_{cc}) Q^\alpha).$$

Rearranging this expression we get:

$$\frac{a_{cc}}{a_s} = 1 + \frac{1}{a_s Q^\alpha} \ln \frac{\tau_s}{\tau_{cc}}.$$

Because the values of a_s , α , and τ_s can be obtained from fitting of the QENS data, and the value of τ_{cc} from fitting of the conductivity decay curve, we can obtain the fraction, $\frac{a_{cc}}{a_s}$, that characterizes the coupling between electron motion and molecular motion. Clearly, the greater the coupling parameter, the faster the charges will be carried by the molecular motion leading to more rapid decay [24]. We can evaluate the coupling parameter to 0.71 for HAT6 at T=363K and 0.64 for HAT6-TNF at T=370K. Meaning that in HAT6 there will be 71 charge carrier hops on 100 proton jumping events and 64 charge carrier hops in HAT6-TNF. The decrease of the parameter with addition of TNF is consistent with a weakening of the connection between charge carrier and molecule leading to higher conductivity because the number of charge carrier hoppings which will be coupled with that of protons has decreased.

7.3.7 Determination of conductivity using relaxation time

The general consistency of the kinetics measured by both the conductivity and neutron scattering is rather good, despite the large separation of timescales. This agreement suggests that the relaxation time, τ , measured in the conductivity is the collision or scattering time in equation 7.1. The value that we obtain for HAT6 using $\tau=15.3$ ns is $\mu=0.28$ cm²V⁻¹s⁻¹, which differs significantly from previous value for mobility for HAT6, $\mu_K=0.012$ cm²V⁻¹s⁻¹ and $\mu_{LC}=0.002$ cm²V⁻¹s⁻¹. These lower mobilities were obtained by a different procedure in which the mobility is determined by assuming that the charge-carrier concentration formed at the initial pulse, is similar to that obtained in other hydrocarbons from the same pulse intensity and that charge carriers were produced homogeneously [13-15]. The main difficulty is that this assumes that the pulse creates the maximum possible number of carriers and does not take into account subtle changes occurring during phase transition, and it is easy to understand how this might lead to underestimation of mobility as well as different qualitative temperature dependence. It is interesting to note that our value of $\mu=0.28$ cm²/Vs for HAT6, agrees quite well with that of octaocetylphthalocyanine, $\mu=0.2$ cm²V⁻¹s⁻¹ which was measured with Time Of Flight technique. Obtaining a reliable conductivity is a complex

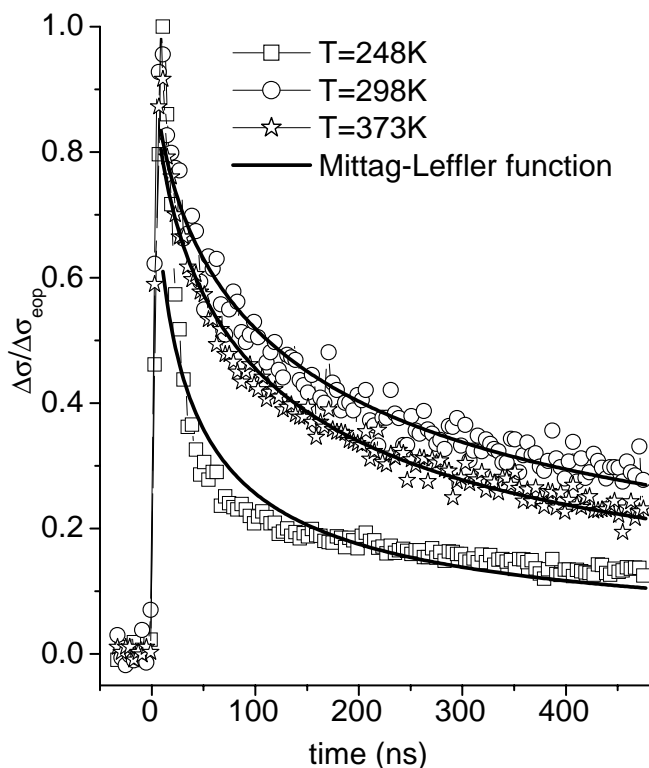


Figure 7.9: Conductivity transients for HAT6-TNF at different temperatures including fits with Mittag-Leffler function.

question that depends strongly on the technique that is used, and a detailed discussion of this goes beyond the scope of the present paper. In this context the precise function used to fit the relaxation data is less crucial since it will have effect on τ which is rather small when compared with the differences obtained by different techniques.

7.4 Conclusion

The central question was: is the coupling between molecular dynamics and charge mobility in discotic systems so strong that they can be described by a single kinetic model from ~ 1 ps to 500 ns? To achieve this we have used a model of entangled dynamics in which an exponential distribution of barriers fluctuates with time maintaining the correct thermal distribution. In principle this relates how even the fast local vibrations affect the trapping and releasing of larger-scale slow molecular reorganizations. This model is particularly well suited to probing the consistency of the dynamics measured by the different methods in this work because it provides physically meaningful parameters and allows evaluating coupling between molecular and charge carrier motions. The relaxation times differ considerably (when comparing the neutron results at $Q=1.12 \text{ \AA}^{-1}$), because

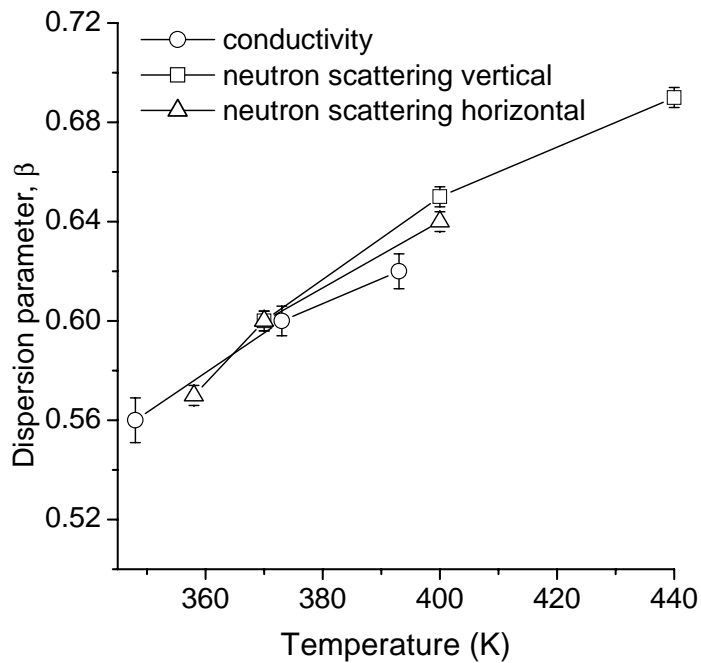


Figure 7.10: Temperature dependence of dispersion parameter β for HAT6-TNF at $Q=1.12 \text{ \AA}^{-1}$ from PR TRMC and neutron scattering in two orientations.

the neutrons measure the response of the H-atoms to the molecular rearrangements, which is much more efficient than the response of the charges. Although there will be different coupling between the various types of molecular motion and charge mobility, we have been able to derive an effect overall coupling parameter. An independent check of our proposals is provided by the distance moved by the charge in the conductivity measurements as derived from the neutron-scattering experiment. This links the two techniques and timescales with a rather reasonable value. Basically, within our model the charge mobility is coupled to the molecular dynamics since they obey the same dynamical equation, the important parameter here being dispersion, β that is directly related to the entropic index.

Bibliography

- [1] L. Schmidt-Mende, A. Fechtenkötter, K. Müllen, E. Moons, R. H. Friend, and J. D. MacKenzie, *Science* 2001 293 1119-1122
- [2] J. Nelson, *Science* 2001 293 1059-1060
- [3] N. Boden, R.J. Bushby, J. Clements, B. Movaghar, K.J. Donovan and T. Kreouzis, *Phys.Rev.B*, 52, 18, 13274, (1995)
- [4] J.M. Warman, A.M. van de Craats, *Molecular Crystals and Liquid Crystals*, 396 (2003) 41-72.
- [5] N. Boden, R.J. Bushby, and J. Clements, *J.Chem.Phys.* 98, 5920 (2003)
- [6] A.M. van de Craats, P.G. Schouten, J.M. Warman, *Journal of the Japanese Liquid Crystal Society*, 2 (1998) 12-27; A.M. van de Craats, L.D.A. Siebbeles, I. Bleyl, D. Haarer, Yu.A. Berlin, A.A. Zharikov, J.M. Warman *Journal of Physical Chemistry B*, 102 (1998) 9625-9634.
- [7] E. Knoesel, M. Bonn, J. Shan, and T. F. Heinz, *Phys.Rev.Lett.*, 86, 340-343 (2001).
- [8] H. Iino, J. Hanna, R. J. Bushby, B. Movaghar, B. J. Whitaker, M. J. Cook, *Appl. Phys. Lett.*, 87, 132102, (2005)
- [9] S.T. Hyde, "Identification of Lyotropic Liquid Crystalline Phase", ch.16. p.307, *Handbook of Applied Surface and Colloid Chemistry* edited by Krister Holmberg, 2001, John Wiley & Sons Ltd
- [10] P. G. Schouten, J. M. Warman, M. P. de Haas, J. F. van der Pol, and J. W. Zwickert, *J. Am. Chem. Soc.*, 114(23), 9028-9034, 1992.
- [11] Yu. A. Berlin, A. L. Burin, and S. F. Fischer, *Chem. Phys.* 220, 25 (1997).
- [12] O. Kruglova, E. Mendes, Z. Yildirim, M. Wbbenhorst, F. M. Mulder, J. Stride, S. J. Picken and G. J. Kearley, submitted to *PhysChemPhys*.
- [13] P. P. Infelta, ; de Haas, M. P.; Warman, J. M. *Rad. Phys. Chem.* 1977, 10, 353.
- [14] Warman, J. M. The microwave absorption technique for studying ion and ionic processes. In *The study of fast processes and transient species by electron pulse radiolysis*; Baxendale, J. H., Busi, F., Eds.; D. Reidel Publishing Company: Dordrecht, 1982; pp 129.
- [15] Warman, J. M.; de Haas, M. P. D., G.; Grozema, F. C.; Piris, J.; Debije, M. G. *Chem. Mater.* 2004, 16, 4600.

- [16] A. Devos, M. Lannoo, Phys. Rev. B, 58, p.8236, 1998
- [17] Yu. A. Berlin et al, J.Chem.Phys., 69, p.2401, 1978
- [18] S. Chandrasekhar and G. S. Ranganath, Rep. Prog. Phys., 53, 57-84, 1990
- [19] D. Markovitsi, F. Rigaut, M. Mouallem and J. Malthête, Chem.Phys.Lett., 135, 236-242, 1987
- [20] Z. Yildirim, M.R. Wübbenhorst, E. Mendes, S.J. Picken, I. Paraschiv, A.T.M. Marcelis, H. Zuilhof and E.J.R. Sudhölter, Journal of Non-Crystalline Solids, 351, 2622 - 2628, 2005
- [21] P. T. Landsberg Eur. J. Phys., 1, 31-38, 1980
- [22] E. A. Katz, D. Faiman, K Iakoubovskii, A. Isakina, K. A. Yagotintsev, M. A. Strzhemechny and I. Balberg, J. Appl. Phys. 93, 3401-3406, 2003
- [23] O. Kruglova, F.M. Mulder, J.A. Stride, I. Paraschiv, H Zuilhof, S.J. Picken and G.J. Kearley (to be published)
- [24] N. Singh and N Kumar, J. Stat. Mech. (2005) L06001.

Chapter 8

General conclusions

The aim of this research was to understand relationship between structure, dynamics and the electronic conduction at the molecular level within columns of triphenylene and its acceptor-donor complexes formed with TNF. The triphenylene system served as a model for more general discotic materials and, possibly, for polymers as well. Its advantage with comparison to other compounds is that it has enough complexity to make it a realistic model compound, yet is not so complex that we are unable to model the details of the dynamics. One would expect motion from the structure of HAT6 molecule that can be represented by two motions: in-plane and out-of-plane assuming that the core remains rigid. Those movements are assumed to interfere with conduction of discotic materials decreasing π orbital overlap, and have been used as the basis in a number of studies.

Our analysis of discotic dynamics has revealed the necessity to treat molecular motion as a whole because the simplified consideration does not take into account the important consequences of complexity in the system. Essentially, the simplified approach will give an incorrect description of the system by omitting the required interdependency of motions. Interpretation of dynamics from the point of view of the model that takes into account disorder and interactions among parts of the system has allowed us to obtain the van Hove correlation function. Knowledge of this function is especially important because it characterizes motion and positions of atoms and molecules in any system in time and space, this being accessible through neutron scattering and simulation. The van Hove correlation function in HAT6 and in HAT6-TNF strongly deviates from a Gaussian function on the timescale and space volumes accessible to QENS. It follows that motions on timescales and space volumes other than that of QENS may also exhibit the same type of behavior. It would be rather interesting to analyze the dynamics on much faster and slower timescales in the future to determine the full range of our model.

In order to understand the influence of molecular vibrations and thermal motion on the electronic structure of HAT6 we have studied it by means of molecular dynamics simulation and subsequent analysis of the electronic structure. Although the model we have used was simple (one column of molecules), the result we have obtained is consistent with that of the dynamics analysis. The distribution of energy fluctuations for total intermolecular interaction and HOMO interaction deviates from conventional Boltzmann distribution, and the degree of fluctuation represents the same order of the magnitude although exact values differ. Nevertheless, this is an important result because calculations made from classical molecular dynamics reproduce the picture of the real system. To get more precise description it would be interesting to repeat such calculations using molecular

dynamics simulation using a better model with periodic boundary conditions, since this would take account of some of long-range correlations, which might be present in HAT6. Therefore, the value of the fluctuation degree obtained from calculations will be in the vicinity of that of obtained from the analysis of dynamics.

The ultimate goal is to find a suitable model which will describe behaviour of the different parts of HAT6 and HAT6-TNF giving the same values for fundamental parameters that characterize those systems, since the molecules and electrons represent the different aspects of a single system. QENS gives information about molecular motion while PR-TRMC provides data that describe motion of charge carriers. Applying the same model for interpretation of the results from two very different experiments one should get the same value that would be characteristic for the system as a whole. In our case it will be the dispersion parameter that reflects delay in relaxation due to potential barrier fluctuation. Indeed, the value of the dispersion parameter is the same for both experiments at the relevant space volume, which indicates the possibility of coupling between molecular and electron (hole) motions in HAT6 and HAT6-TNF. Moreover, this coupling can be quantified in the context of applied model. In such way it is possible to understand the underlying mechanism of conduction in the material. In the future it would be interesting to analyze discotic liquid crystals with different symmetry and tails length from point of view of this model.

Summary

In this dissertation the dependency between structure and dynamics, and its influence on charge transfer properties of self-assembling discotic liquid crystalline materials, are studied in some detail. Dynamics was probed by quasielastic neutron scattering (protons) and PR-TRMC (charge carriers). Both techniques are complimentary since they give information about different parts of a single system and they should give the same qualitative result.

Chapter 1 starts with a brief overview of liquid crystals in general, and discotic liquid crystals in particular. Subsequently, a theory of neutron scattering is discussed in detail followed by description of the continuous time random walk model on which the fractional diffusion equation is built. Solution of that fractional diffusion equation represents van Hove correlation Function that is measured in neutron scattering experiment. The model for relaxation kinetics in a correlating environment parameterizes the van Hove correlation function and gives a more physical insight of the processes occurring in system. After a short description of the conduction process, the possible connection between molecular dynamics and charge carrier motion is examined.

In Chapter 2 a brief description of the techniques that have been used for data analysis is presented. It is divided into two sections, which include appropriate techniques for structure and dynamics interpretation.

In Chapter 3 the QENS data for hexakis(n-hexyloxy)triphenylene is discussed from the point of view of the model for relaxation kinetics in correlating environment. It is demonstrated that the new approach gives information about the discotic energy landscape obtained by analysis of hydrogen motion. The relaxation-time dependence from momentum transfer is analyzed and the deviation from a Gaussian shape is established. That allowed us to build the van Hove correlation function in Laplace-Fourier space for HAT6. A dynamics analysis revealed the presence of long-range correlations and a hierarchical order of relaxation.

In Chapter 4 the vibrational dynamics of the different triphenylene derivatives is considered by means of inelastic neutron scattering. INS data is compared with first-principles calculations. The compact model that reproduces essential features of vibrational dynamics is suggested. It has revealed that vibrational dynamics of the molecular core and tails is decoupled. This conclusion will simplify future calculation for electronically excited states.

In Chapter 5 the influence of molecular thermal motion on electronic structure is considered. Data obtained from molecular dynamics simulation have been used to analyze electronic structure and revealed presence of two separate motions: slow whole body motions of the disks, and internal vibrational modes of the aromatic cores. Some vibrational motions may have a surprisingly strong impact on conductive properties of HAT6.

In Chapter 6 the structure of the charge transfer complex that HAT6 forms with trinitrofluor-

renone is analyzed by means of X-ray diffraction, elastic and quasielastic neutron scattering and dielectric relaxation spectroscopy. It is demonstrated that unlike the previous assumption, the acceptor molecule lies among the tails of HAT6. This has an important outcome for future application of discotic liquid crystals because such a position of TNF will lead to the improvement of charge transfer rate.

In Chapter 7 the dynamics from QENS of HAT6 and HAT6-TNF are compared. The relaxation time and dispersion parameter for both compounds are analyzed. The conductivity for both materials measured using PR-TRMC is interpreted from point of view the same model as dynamics. It revealed that both experiments give the same dispersion parameter that describes the effect of potential barrier fluctuations on the relaxation time. A possible explanation is suggested for electron-phonon coupling in discotic crystalline materials.

In Chapter 8 general conclusions are represented.

Samenvatting

Het onderwerp van deze dissertatie is de studie van de moleculaire structuur en dynamica van zichzelf organiserende discotische vloeibaar kristallijne materialen, en het verband tussen structuur en dynamica en ladingstransport. De moleculaire dynamica is experimenteel bepaald met behulp van quasi elastische neutronen verstrooiing (QENS), waarbij voornamelijk de beweging van protonen wordt waargenomen. De dynamica van ladingsdragers is bepaald met PR-TRMC. Beide experimentele technieken geven complementaire informatie over het systeem.

Hoofdstuk 1 geeft een korte introductie van vloeibaar kristallijne discotische materialen. Theoretische aspecten van neutronen verstrooiing worden gepresenteerd, gevolgd door een beschrijving van het 'continuous time random walk' model waarop de fractionele diffusie vergelijking is gebaseerd. De oplossing van deze fractionele diffusie vergelijking geeft een van Hove correlatie functie zoals experimenteel bepaald in neutronen verstrooiings experimenten. Het model voor de kinetiek van relaxatie van correlaties parametrizeert de van Hove correlatie functie en leidt daarmee tot meer fysisch inzicht in de dynamische processen die optreden in het systeem. Na een korte beschrijving van geleidings processen wordt het mogelijke verband tussen moleculaire dynamica en ladingsdrager mobiliteit aangegeven.

In hoofdstuk 2 worden de technieken die zijn gebruikt voor data analyse geïntroduceerd, verdeeld over twee secties met toepasbare methoden voor de analyse van structuur en dynamica.

In hoofdstuk 3 worden de QENS data voor hexakis(n-hexyloxy)triphenylene (HAT6) bediscussieerd vanuit het model voor de relaxatie van correlaties. Deze nieuwe benadering geeft informatie over het energie-landschap waarin de discotische moleculen zich bewegen door analyse van de gemeten bewegingen van HAT6 waterstof atomen. De afhankelijkheid van de relaxatietijden van impuls overdracht is bestudeerd en een afwijking van Gaussische vorm is aangetoond. Hiermee kan de van Hove correlatie functie in Laplace-Fourier ruimte geconstrueerd worden voor HAT6. Analyse van de dynamica laat de aanwezigheid van lange-dracht correlaties en hierarchische ordening van relaxatie zien.

In hoofdstuk 4 wordt de vibrationele dynamica van verschillende triphenylene afgeleide materialen met behulp van inelastische neutronen verstrooiing (INS) bestudeerd. De INS data worden vergeleken met 'first principles' computer berekeningen. De resultaten geven aan dat de vibrationele dynamica van de alkyl 'staarten' en de aromatische centrale gedeelten ('core') van de discotische moleculen ontkoppeld zijn. Deze conclusie kan toekomstige berekeningen van elektronische excitaties sterk vereenvoudigen.

In hoofdstuk 5 wordt de invloed van de thermische moleculaire beweging op de instantane elektronische structuur beschreven. Data verkregen via moleculaire dynamica simulaties zijn gebruikt waarbij langzame bewegingen van het hele molecuul en snelle interne vibraties van de polyaroma-

tische core naar voren komen. Deze bewegingen kunnen sterke invloed hebben op de geleidende eigenschappen van HAT6.

In hoofdstuk 6 wordt de structuur van het 'charge transfer complex' van HAT6 en trinitrofluorenone (TNF) volgend uit Röntgen diffractie, elastische en inelastische neutronen verstrooiing en dielectrische spectroscopie beschreven. Het wordt aangetoond dat -in tegenstelling tot eerdere aannamen- het acceptor molecuul TNF zich tussen de alkyl staarten bevindt. Er wordt aangenomen dat dit relevant is voor mogelijke toepassingen aangezien de geleiding door deze positie van TNF niet nadelig beïnvloed wordt.

In hoofdstuk 7 wordt de dynamica volgend uit QENS van HAT6 en HAT6-TNF vergeleken. De relaxatie tijden en dispersie parameters voor beide materialen worden geanalyseerd. De geleiding van beide materialen volgend uit PR-TRMC wordt geïnterpreteerd volgens een model gerelateerd aan dat voor de moleculaire dynamica. Beide experimenten geven dezelfde dispersie parameter die het effect van potentiaal barrières aangeeft op de relaxatie tijden. Electron phonon koppeling in deze materialen wordt beschreven.

In hoofdstuk 8 worden enige algemene conclusies van het onderzoek gepresenteerd.

Acknowledgements

It seems just yesterday I have started to work on the project results of which are presented in this thesis. The time, four and half years, I have spent here has passed almost unnoticeable. There were ups and downs along this way but the atmosphere created here was always pleasant and sympathetic.

First of all I would like to express my enormous gratitude to my promoter and daily advisor, professor Don Kearley. Despite his very busy schedule he always found time to hear all my ideas and problems whether it was science or something else. Don gave me the freedom to make research in my own way and was always opened to new approaches. Looking for the answers on questions he has asked me during our discussions helped me to deepen my understanding of the processes in discotics. From him I have learned a lot not just about neutron scattering technique and modeling but also about paper writing and life in The Netherlands from the point of view of foreigner. Dear Don, thank you for giving me an opportunity to work here, in TUDelft and for believing in me. It was such a pleasure to work with you! I hope there will be a chance in life to work together again.

Another words of gratitude I would like to express to Fokko Mulder, who was supposed to be my daily advisor. Unfortunately, his involvement in several different projects has made daily advising somewhat difficult. But Fokko's criticism, always constructive, and the ability to see what is hidden have allowed improving significantly the fundamental understanding of this project. I am absolutely indebted to Fokko for his help in resolving very difficult situations. Dear Fokko, thank you for your critical words, advises when I needed them the most and real help. I am sorry if sometimes I was difficult person to communicate with.

Without vast knowledge of professor Stephan Picken and chemical "aid", as well as nice conversations outside science, of Zeynep Yildirim this work would not be complete leaving a lot of questions unanswered.

I would like to thank my "officemates" Alexander, Lambert and Gijs and other members of the department, Sarita, Naveed, Wicher, with whom I had enjoyable discussions on different subjects. But I am especially grateful to Alexander Schmets who was not only my "officemate" but became real friend who was/is willing to help whether it is translation of propositions in Dutch or bringing pram from Almere.

My dear friends Elena Taracheva, Svetlana Divina, Oksana Anisimova and Dmitry Divine shared with me my joy and tears, frustration and happiness encouraging and helping me in any possible way. I was truly blessed having such reliable friends. Thank you for being there for me whenever I needed it! My brother, Sergey, has given me unconditional love and support, for which I am so thankful. My friend outside work, Peter, I have met whilst writing thesis. His optimism and sense of humor cheered me up helping me through this quite stressful period of my life. I would like to

express my special appreciation to Tina Keogh and Tamar Melzer who helped me before and after the birth of my son.

Last, but not least, I would like to thank my son, Ilusha, who was/is my inspiration, motivation and the reason why this thesis were completed.

Curriculum Vitae

Olga Viktorovna Kruglova was born on the 23^d April 1974 in Nizhnij Tagil, Russia. There she attended the primary and secondary school, which she finished in June 1991. In September 1991 she continued her education in the Faculty of Physics of Saint Petersburg State University. She received her Bachelor of Science with specialization in optics in June 1996. In September 1996 she changed her study from optics to decay kinetics of excited molecules in atmosphere in Atmospheric Physics Department. She received her Master of Science in December 1998. After short period on PhD programme on the Atmospheric Physics Department she started a PhD project in University of Puerto Rico in July 1999. After one and half year she returned back to Russia, where she began to work on the project devoted to photoemission in CO₂ molecules on Solid State Electronics Department in Saint Petersburg State. One and a half year later, in October 2002, she started her PhD project in Interfacultair Reactor Institute, TUDelft, results of which are represented in this thesis.

List of Publications

"Analysis of quasielastic neutron scattering (QENS) data of discotic systems using different molecular dynamics (MD)models", O. Kruglova, F.M. Mulder, S.J. Picken, J.A. Stride, G.J. Kearley, *Physica B* **350**, e1003-e1005 (2004)

"Origin of Heterogeneous Relaxation in a Random Liquid Crystal Thermoset Copolyester", G. J. Kearley, Th. J. Dingemans, O. Kruglova, J.A. Stride, and F. M. Mulder, *Macromolecules* **37**, 9855-9860(2004)

"A Compact Model System For Electron-Phonon Calculations In Discotic Materials", O. Kruglova, F. M. Mulder, A. Kotlewski, S. J. Picken, S. Parker, M. R. Johnson and G. J. Kearley, *Chem. Phys.* **330**, 360 (2006)

"Coupling between local vibrations and charge transport in discotic materials", O.Kruglova, F.M.Mulder, L.D.A. Siebbeles and G.J. Kearley, *Chem. Phys.* **330**, 333 (2006)

"Structure of discotic liquid crystalline charge transfer complex", O. Kruglova, E. Mendes, Z. Yildirim, M. Wübbenhorst F. M. Mulder, J.A. Stride, S. J. Picken and G. J. Kearley, submitted to *ChemPhysChem*

"A New Approach to Dispersive Kinetics: Experiment and Theory", O. Kruglova, F. M. Mulder, S. J. Picken, J. A. Stride, I. Paraschiv, H. Zuilhof and G. J. Kearley, submitted to *J. of Chem. Phys.*

"Conductivity of discotic liquid crystals: from molecular dynamics to charge dynamics", O. Kruglova, F. C. Grozema, R.D. Abellon F.M. Mulder, J.A. Stride, S.J. Picken and G.J. Kearley, in preparation

Acronyms

HAT6: hexakis(n-hexyloxy)triphenylene

TNF: 2,4,7 trinitro-9-fluorenone

LC: liquid crystal

QENS: Quasielastic Neutron Scattering

MD: Molecular Dynamics

DFT: Density Functional Theory

NSE: Neutron Spin-Echo

DRS: Dielectric Relaxation Spectroscopy

PR TRMC: Pulse-Radiolysis Time resolved Conductivity

IFT: Inverse Fourier Transform

HOMO: Highest Occupied Molecular Orbital

LUMO: Lowest Unoccupied Molecular Orbital

INS: Inelastic Neutron Scattering

LDA: Local Density Approximation